FACHBEREICH NATURWISSENSCHAFTEN
BERGISCHE UNIVERSITÄT
WUPPERTAL

Search for Poorly Localized Gamma-Ray Bursts in AMANDA-II Data

Anna Franckowiak

Diplomarbeit

Juni 2007
WU D 07 12


Andy Warhol

Für meinen Vater.

Abstract

The AMANDA detector was built between 1995 and 2000 at the geographic South Pole with its main purpose to detect high-energy neutrinos from astrophysical sources. The detection of neutrinos in temporal and directional coincidence with photons from gamma ray bursts (GRBs) is of special interest for the basic understanding of the physical processes that cause GRBs and in addition would identify GRBs as possible sources of ultra-high-energy cosmic rays.
The first part of this work contains a brief summary of the current observational facts and empirical relations found for the characteristics of GRB, followed by an introduction to the widely accepted theoretical model explaining most of the observations: the relativistic fireball model. Design and principle of operation of gamma-ray detectors mounted on satellites and the AMANDA-II neutrino detector are presented focussing on poorly localized GRBs.
The presented analysis contains improved detector stability tests and cut optimizations to separate signal from background events. Data of 64 poorly localized bursts observed in 2000-2004 has been unblinded and no recorded neutrino event passed the applied selection cuts. The absence of surviving events allows us to set a limit of

$$E^2 \cdot \Phi(E)_{90\%} \leq 4.4 \cdot 10^{-4}\,\mathrm{GeV\,cm^{-2}\,s^{-1}}$$

on the neutrino flux in the energy range of $10^5\,\mathrm{GeV}$ to $10^7\,\mathrm{GeV}$. This limit is 8.8 times above the flux predicted by the Waxman Bahcall model.
Finally a brief comparison with former GRB coincidence analyses and their results is made followed by an outlook to future analyses.

Contents

1 Introduction **1**

2 Gamma-Ray Bursts **5**
2.1 Observational Facts and Empirical Relations 5
2.1.1 Lightcurve and Duration 5
2.1.2 General Characteristics 6
2.1.3 Redshift and Redshift Estimates 8
2.1.4 Photon Spectrum 9
2.1.5 Afterglow Emission 10
2.2 The Relativistic Fireball Shock Model 11
2.2.1 Fermi Acceleration 11
2.2.2 Internal-External Shocks Model 15
2.2.3 Collimation of Emission 15
2.2.4 Inner Engine of GRBs 16
2.2.5 Neutrino Spectrum 17
2.2.6 Neutrino Oscillation 21
2.3 The Cannonball Model 22

3 Satellites **25**
3.1 The Third Interplanetary Network 25
3.1.1 Ulysses 27
3.1.2 KONUS-Wind 29
3.1.3 HETE-II 30
3.2 Coordinate Systems 32
3.2.1 The Equatorial Coordinate System 32
3.2.2 The Ecliptical Coordinate System 33

4 Neutrino Detection **35**
4.1 The AMANDA Detector 35
4.1.1 Design 35
4.1.2 Principle of Operation 36
4.1.3 The AMANDA Coordinate System 39
4.2 Background 39

4.3 Simulation of Neutrino Signal Events . . . 41
4.3.1 Simulation of Neutrino Interactions . . . 41
4.3.2 Muon Propagation . . . 41
4.3.3 Photon Propagation . . . 42
4.3.4 AMANDA-II Detector Simulation . . . 43
4.4 AMANDA Data - Reconstruction and Filtering . . . 43
4.4.1 Trigger and Hit Cleaning . . . 43
4.4.2 Track Reconstruction . . . 44
4.4.3 Upgoing Muon Filtering . . . 46
4.4.4 Track Quality Parameters . . . 46

5 Analysis of Poorly Localized GRBs in 2000-2004 **51**
5.1 Selection of Poorly Localized Bursts . . . 51
5.2 Detector Stability . . . 53
5.2.1 The Cumulative Test . . . 55
5.2.2 The Likelihood Test . . . 57
5.2.3 ΔT-Distribution . . . 61
5.3 Reweighting of Simulated Events . . . 62
5.3.1 Energy Reweighting . . . 62
5.3.2 Directional Reweighting . . . 63
5.4 Cut Variable Selection . . . 66
5.4.1 Temporal Cut / Definition of the Search Window . . . 67
5.4.2 Directional Cut . . . 67
5.4.3 Reconstruction Quality Cuts . . . 69
5.5 Cut Optimization . . . 72
5.5.1 Confidence Belt and Upper Limit . . . 72
5.5.2 Average Flux Upper Limit . . . 73
5.5.3 Optimization Technique . . . 73
5.5.4 Systematic Uncertainties . . . 80

6 Unblinding and Results **87**

7 Summary and Outlook **89**

Appendices

A Detailed Burst Information **91**

Bibliography **97**

List of Figures

1.1 Number of GRB Publications per Year. 2

2.1 Duration Distribution of BATSE Bursts 6
2.2 Different Shaped Light Curves Recorded by BATSE 7
2.3 Spatial Distribution of BATSE GRBs. 8
2.4 Average Photon Energy Spectrum. 10
2.5 Second Order Fermi Acceleration 12
2.6 First Order Fermi Acceleration 14
2.7 The Internal-External Shock Scenario 16
2.8 Average Neutrino Energy Spectrum. 21
2.9 The Cannonball Model 23

3.1 The Triangulation Method 26
3.2 The Trajectory of the Ulysses Spacecraft 28
3.3 The Hard X-ray Detector Aboard the Ulysses Spacecraft 28
3.4 The Soft X-ray Detector Aboard the Ulysses Spacecraft 29
3.5 The KONUS Gamma-Ray Sensor 30
3.6 The Wind Spacecraft 31
3.7 Schematic Drawing of the HETE-II Spacecraft 32
3.8 The FREGATE Detector 33
3.9 Rotation, Precession and Nutation 34
3.10 The Equatorial and Ecliptical Coordinate Systems 34

4.1 The AMANDA Detector. 37
4.2 Detection Mechanisms in AMANDA 38
4.3 The AMANDA Coordinate System 40
4.4 Smoothness Illustration. 49

5.1 Probability Distribution within a Triangulation Annulus 52
5.2 The Two Classes of Poor Localization Used in This Analysis 53
5.3 Blind Interval 54
5.4 Cumulative Event Number Distribution 55
5.5 χ^2 of Cumulative Event Number Distribution for Different Start Bin Positions 56
5.6 Distribution of $\chi^2_{\max}$ 56

5.7 Simulated $\chi^2_{\max}$ Distribution and its Cumulative. 57
5.8 GRBs with Missing Data in the Off-time Window 58
5.9 Poisson Fit to the Data Contained in the Off-time Window 58
5.10 Variation of Level 3 Event Rates in 2001 59
5.11 Simulated minimal -ln($\mathcal{L}$) Distribution 60
5.12 Simulated Cumulative minimal -ln($\mathcal{L}$) Distribution 60
5.13 Burst Rate Affected by the VLF Veto 61
5.14 ΔT-Distribution 62
5.15 Energy Reweighting 63
5.16 Distribution of Energy Weights 64
5.17 Distribution of Directional Weights 65
5.18 Directional Reweighting 65
5.19 Neutrino Search Window 68
5.20 MC True Direction Compared to Reconstructed Direction 69
5.21 Declination Distribution 70
5.22 Distribution of the Angular Resolution for Background and Signal 71
5.23 Distribution of Smoothness for Background and Signal 71
5.24 Likelihood Distribution for Background and Signal 72
5.25 Scheme of the Iterative Optimization Process 76
5.26 MRF vs. Cut Values 78
5.27 Distribution of Selected Cut Values for All Bursts 79
5.28 Number of Signal and Background Events Passing the Selected Cuts 80
5.29 Combined MRF Dependent on Number of Bursts Included 81

List of Tables

2.1 Average Neutrino Spectrum Parameter 20

4.1 Simplified Model of Propagation Material 42
4.2 Number of Bad OMs per Year 44
4.3 Reconstructions and Quality Cut Levels in AMANDA Data Processing . . 47
4.4 Number of Events in AMANDA Data at Different Cleaning Levels 47
4.5 Signal Passing Rates at Different Cleaning Levels 47

5.1 Yearly Event Rates at Level 3 59
5.2 Start Values and Step Size Used in Cut Optimization 77
5.3 Summary of Systematic Uncertainties 84

A.1 List of Initially Selected GRBs in 2000 from the IPN catalog 92
A.2 List of Initially Selected GRBs in 2001 from the IPN catalog 93
A.3 List of Initially Selected GRBs in 2002 from the IPN catalog 94
A.4 List of Initially Selected GRBs in 2003 from the IPN catalog 95
A.5 List of Initially Selected GRBs in 2004 from the IPN catalog 95

Chapter 1

Introduction

On 10th of October 1963 the "Treaty Banning Nuclear Weapon Tests in the Atmosphere, Outer Space and Under Water" came into force. The governments of the United States of America, the United Kingdom of Great Britain and Northern Ireland, and the Union of Soviet Socialist Republics were the first parties to sign the contract.
To verify compliance with the treaty, the US Air Force designed and built a series of satellites at the Los Alamos Scientific Laboratory and Sandia Laboratories of Albuquerque New Mexico, which were launched in October 1963. These "Vela" satellites[1] were part of a research program with the goal of developing a technology to monitor nuclear weapon tests on Earth, in space and even on the dark side of the moon by detecting the emitted gamma and X-ray radiation. The satellites were launched and operated in pairs of two identical satellites on opposite sides of a geocentric circular orbit with a radius of 120,000 km, so no part of the Earth was shielded from direct observation. Six pairs of Vela spacecrafts were successfully launched. Each satellite carried an X-ray, gamma-ray and neutron detector. On each spacecraft six cesium-iodide scintillation counters provided a nearly uniform omnidirectional response. Their energy response was defined by two level discriminators in the interval 0.15 to 0.75 MeV for Vela 5 and 0.3 to 1.5 MeV for Vela 6. A logics and data storage system enabled nearly continuous coverage in time with a time resolution of 16 ms.
Occasional occurrence of brief but intense bursts of cosmic gamma-rays was detected by the Vela satellites. The measured flashes of radiation did not have the signature of nuclear weapons. The large diameter of the Vela orbit and their accurate time measurement enabled the determination of directional information of gamma sources, if several satellites responded to the same event (more details of these triangulation method can be found in section 3). The derived spatial distribution of 39 events detected by the Vela satellites appeared consistent with isotropy. The first observation of Gamma Ray Bursts (GRBs) had taken place and first results were published in 1973 [1], starting the modern scientific study of GRBs. The interest in GRBs has increased since their first discovery, which is reflected in the number of publications per year shown in Figure 1.1 adapted from [2]. Today scientists believe to have a basic understanding of the GRB phenomenon, but

[1] Vela means "watch" in Spanish

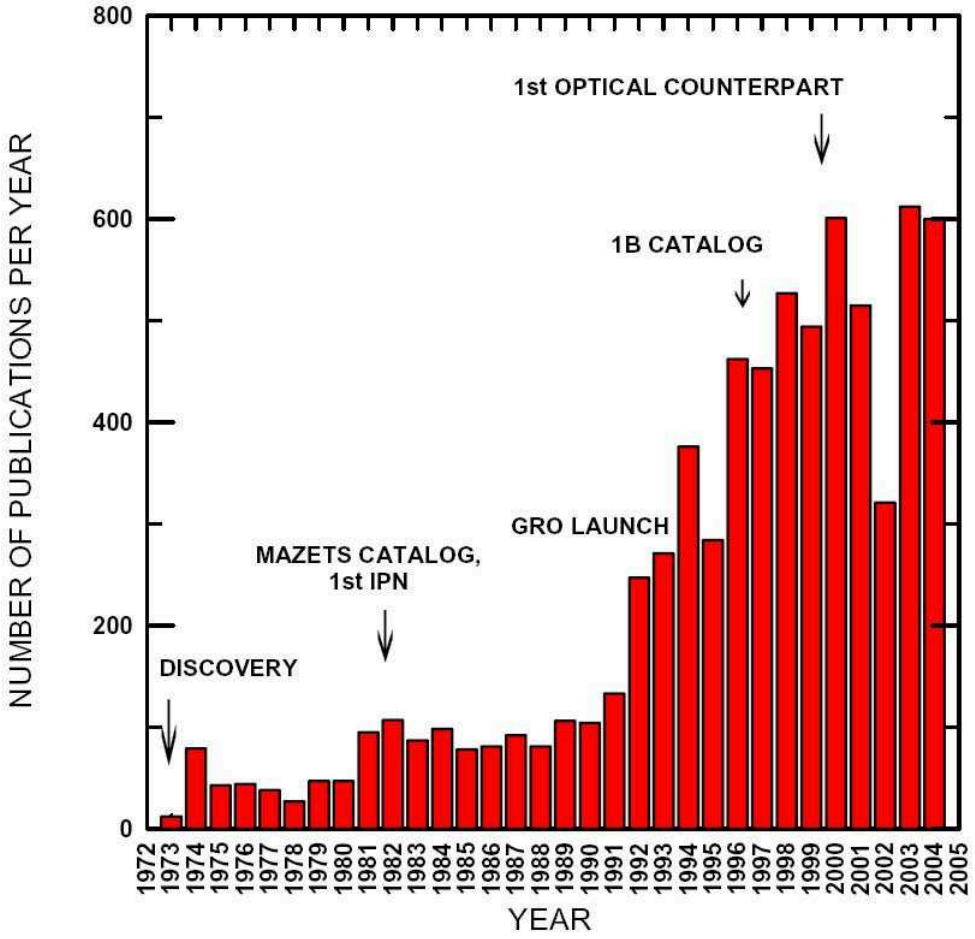

Figure 1.1: Increasing number of GRB-related publications with time from discovery year 1972 to 2004. Important incidence are marked (from [2]).

there are still several open questions. A brief summary of the important observational facts and empirical relations known about GRBs will be presented in section 2.1 followed by an introduction to the "Relativistic Fireball Shock Model" in section 2.2. It will be shown that most of the present observations are well described by the theoretical model. The fundamental question of the physical conditions in GRBs addressed in the model might be answered by the detection of correlations of high energy neutrinos with cosmic gamma-rays. This might also help to prove present theories on acceleration mechanisms of ultra-high-energy cosmic rays (UHECR) and to confirm the acceleration of protons to ultra-high energies within GRB sources. This in turn would prove the possible role of GRB sources as origin of UHECRs.
To prove the coincidence two types of detectors are required. First of all gamma-rays with cosmological origin are observed by gamma-ray detectors mounted on satellites (see chapter 3). High-energy neutrinos, however, can be measured in large neutrino telescopes

like Baikal [3], AMANDA[2], ANTARES[3] or IceCube[4]. A brief description of neutrino detectors with a focus on the AMANDA detector, which was used in the presented GRB analysis, can be found in chapter 4. Previous GRB analyses neglected the class of not well localized GRBs, which represents an important subsample of the detected GRBs, especially after the switch-off of the BATSE satellite [4] in May 2000 before the launch of Swift [5] in November 2004. BATSE and Swift are direction sensitive, while most other satellites are not. A burst has to be triggered by at least three of those non direction sensitive satellites to obtain a good localization whereas two are required for poor localization. This gave motivation to an analysis of 64 bursts from 2000-2004, which were localized within a narrow annulus or a banana shaped segment in the sky. This analysis is presented in chapter 5, it assumes the contemporaneity for neutrino and gamma-ray arrivals.
The analysis can be divided in three steps. First the detector stability is tested for the temporal neighborhood of each burst. In a second step variables are selected to provide a separation of background and signal data. Cuts on these variables are optimized in order to set the most stringent limit on the theoretical flux model. Both steps are executed "blindly", i.e. the recorded data that is believed to contain the expected GRB neutrino signal is excluded from investigations to avoid the introduction of a bias to the cut selection. Finally, in the last step, the developed cuts are applied to these data as well. The outcome allows to set an upper limit on the predicted flux. The results are summarized in chapter 6 and an outlook to future analyses is given.

[2]Antarctic Muon and Neutrino Detector Array
[3]http://antares.in2p3.fr/
[4]http://icecube.wisc.edu/

Chapter 2

Gamma-Ray Bursts

Gamma-Ray bursts are electromagnetic signals of short durations in the gamma-ray band (typical energy $0.1 - 1\,\mathrm{MeV}$). They are detected roughly once per day from random directions. During their short duration they are in fact the most concentrated and brightest electromagnetic events in the Universe outshining every other source of gamma-rays in the sky. They are a hundred times brighter than a typical supernova. Follow-up X-ray and radio observations by space or ground based telescopes allow an accurate determination of their position, which proves their cosmological distance (up to Gigaparsecs or redshifts of ~ 4.5). Despite of their extreme distance, GRBs still outshine galaxies and quasars by a very large factor, therefore their luminosity is believed to be much greater. Their electromagnetic energy output in tens of seconds is comparable to that of the Sun in 10^{10} years or the entire Milky Way over a few years. A cataclysmic stellar event like the collapse of a massive star or the merger of two remnant compact cores (neutron stars or black holes) might be responsible for this enormous energy release. Such events are possibly accompanied by non-electromagnetic signals like cosmic rays, neutrinos and gravitational waves. *The Relativistic Fireball Shock Model* (section 2.2) describes the theoretical scenario of a GRB and successfully predicts many of the observed properties (section 2.1).

2.1 Observational Facts and Empirical Relations

2.1.1 Lightcurve and Duration

The duration of gamma-ray burst varies over 5 orders of magnitude in the range of $10^{-2} - 10^{3}\,\mathrm{s}$. BATSE observations discovered a bimodal distribution of the duration, which is displayed in Figure 2.1. This distribution implies a classification of GRBs by their duration: *Short bursts* have a typical duration of 0.2 s and do not last longer than 2 s whereas *long burst* last at least 2 s and have a typical duration of 50 s. Typically short bursts have a harder spectrum and a higher peak energy than long bursts, which confirms the above classification. Roughly one quarter of the total burst population consists of short bursts while the other three quarters are of long durations. The two classes of GRBs might have different origins. Most of our current knowledge is based on observations of

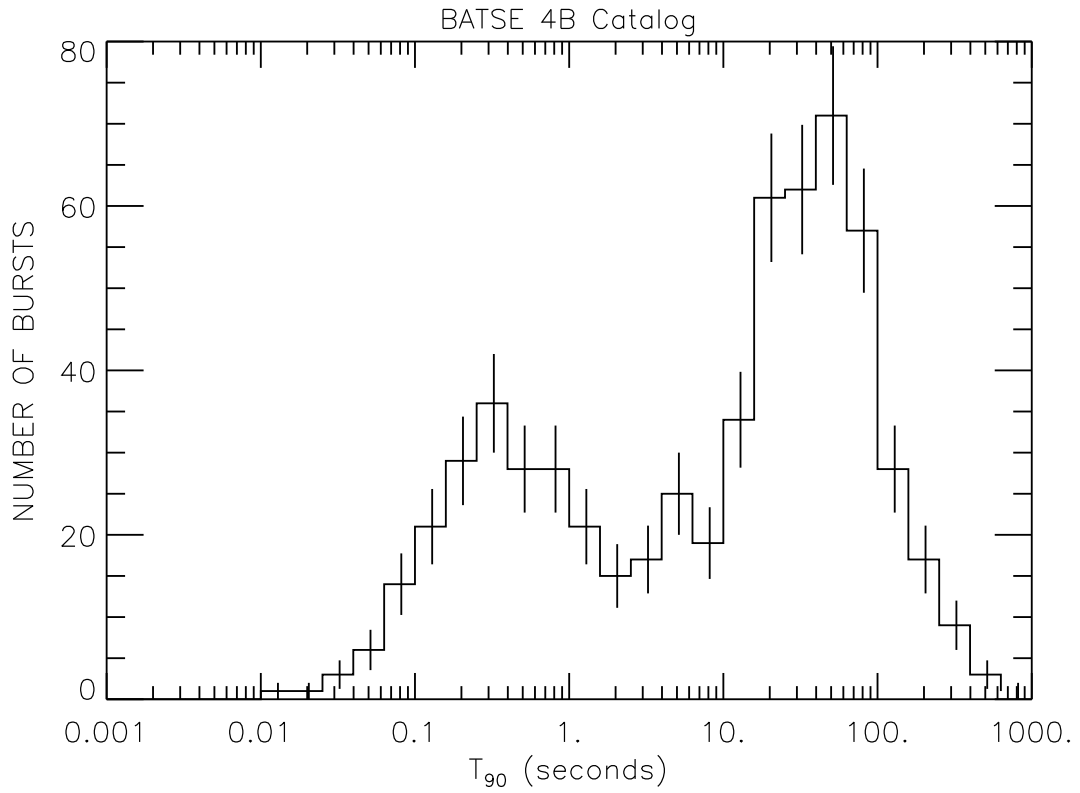

Figure 2.1: The time distribution of BATSE bursts show a bimodal behavior (from [6])

long bursts while the nature of short bursts to a large extent is still a mystery.
The measured light curves are very irregular and individual pulses vary in a wide range. Figure 2.2 gives an overview of different shaped light curves observed by BATSE [4]. The strong variation among different bursts is obvious. They range from smooth to highly variable curves with many peaks. Some are fast rising with quasi-exponential decay. The curves vary rapidly on scales less than $\Delta T \sim 10\,\mathrm{msec}$, which implies a compact object producing the gamma-rays ($R \leq c\Delta T \sim 3000\,\mathrm{km}$). The burst duration is usually quantified by T_{90}, the time interval over which a burst emits from 5% to 95% of its total number of measured photons. T_{90} depends on the characteristics of the detector (see section 3.1).

2.1.2 General Characteristics

The angular distribution of GRBs is isotropic as illustrated in Figure 2.3. The angular distribution provides two dimensions of the spatial distribution, while the intensity distribution is a convolution of the radial distribution and the luminosity distribution. Even though the latter one is unknown, the integral intensity distribution provides constraints on the compatibility of the spatial distributions of the GRB sources with homogeneity of the universe [8]. The observed intensity distribution of GRBs is consistent with homo-

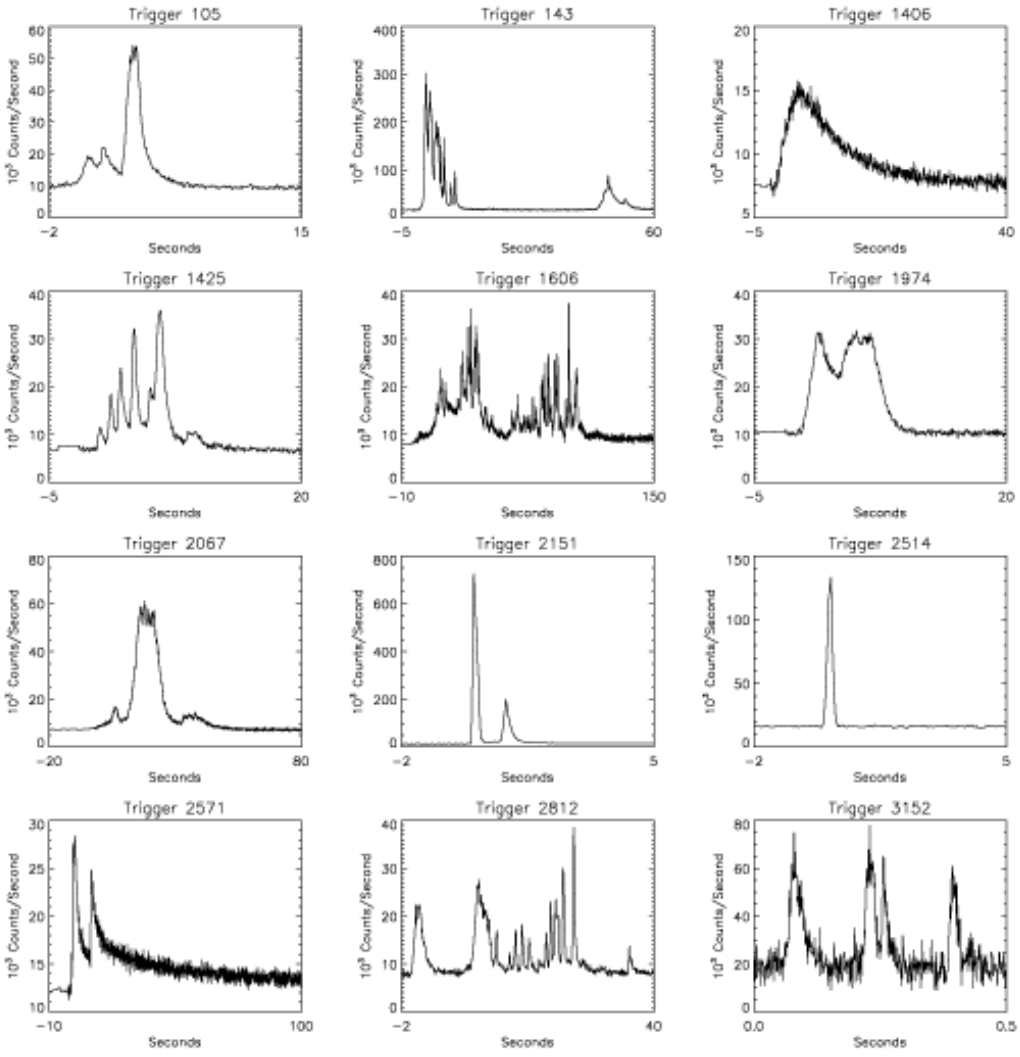

Figure 2.2: The shape of the light curve, here observed by BATSE, varies strongly for different GRBs (from [7])

geneity of the universe, which is, according to the standard model of cosmology, on large scales[1] ($> 100\,\mathrm{Mpc}$ or $z > 0.023$), isotropic and homogeneous. There are no preferred directions and no preferred locations in the universe on large scales. According to their homogeneous and isotropic distribution, GRB are considered cosmological events.
The average GRB birthrate integrated over the observable universe[2] is $\sim 7.5\,\mathrm{Gpc}^{-3}\,\mathrm{yr}^{-1}$ (for $H_0 \sim 70\,\mathrm{km\,s}^{-1}\,\mathrm{Mpc}^{-1}$ and an average galaxy number density of $n_g \sim 0.02\,\mathrm{Mpc}^{-3}$). GRBs are very likely collimated and observed light curve steepenings may be due to a collimated emission with jet opening angles from 5° to 20° (see section 2.2.3). Assuming

[1] comparable to the length scale of the local supercluster with a dimension of $\sim$ 200 million lightyears or $\sim 60\,\mathrm{Mpc}$

[2] also referred to as Hubble volume

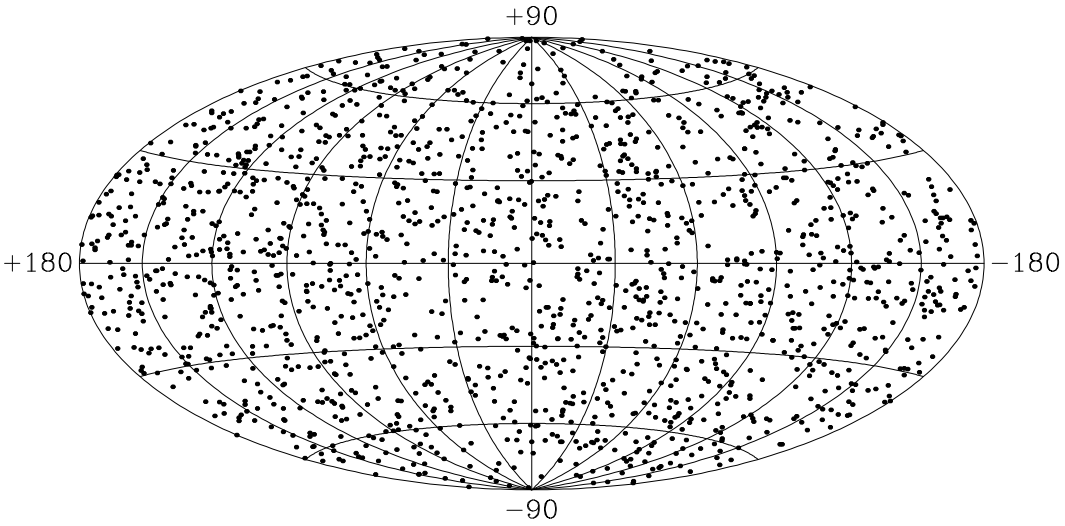

Figure 2.3: The spatial distribution of all 1637 GRBs from the BATSE 4Br catalog shows an isotropic sky coverage. [6]

isotropic energy emission leads to a total isotropic energy emission varying up to three orders of magnitude ($10^{51} - 10^{54}$ ergs), but corrections, accounting for collimation of the emission, yield a constant total energy emission of 10^{51} ergs. Long collimated GRBs seem to have a standard energy reservoir and eventually might be used as standard candles. [9] Although polarization of radiation, especially in the gamma-ray band, is difficult to measure, strong polarization of the prompt emission was discovered in single cases (see [10], [11] or [12] for example).

2.1.3 Redshift and Redshift Estimates

Spectroscopic observation of absorption lines in the spectra of afterglows (see section 2.1.5) and emission lines in the spectra of the host galaxy allow the determination of GRB redshifts. Absorption lines in distant galaxies are shifted to longer wavelength (redshifted) compared to the wavelength of the same absorption line measured in a laboratory on Earth due to the expansion of the Universe. The galaxy's redshift z is given by

$$z = \frac{\lambda_{obs} - \lambda_{em}}{\lambda_{em}}. \tag{2.1}$$

λ_{em} is the absorption wavelength measured in the rest frame while λ_{obs} stands for the measured wavelength of an absorption line in a distant galaxy. The Hubble law allows to estimate the distance of a galaxy from its measured redshift. According to the Hubble law redshift and distance r are related linearly:

$$z = \frac{H_0}{c} r, \tag{2.2}$$

where $H_0 = 70 \pm 7\,\mathrm{km\,s^{-1}\,Mpc^{-1}}$ is the Hubble constant [13].
Based on a few GRBs with observed redshift, temporal and spectral parameters have been

investigated, in order to find correlations between the luminosity and the redshift of the burst. For known luminosity L and measured flux f the *luminosity distance* is defined as:

$$d_L = \sqrt{\frac{L}{4\pi f}}. \tag{2.3}$$

Assuming that space is flat, which is consistent with present observations, the relation between luminosity distance and current proper distance $d_p(t_0)$ is given by (from [13]):

$$d_L = d_p(t_0)(1+z). \tag{2.4}$$

Several correlations between burst luminosity and quantities that can be measured directly from the light curve of long bursts have been proposed. Stern et al. suggested that *simple* bursts, those with light curves dominated by a single, smooth peak, are less luminous than *complex* bursts with light curves consisting of overlapping pulses [14]. Norris et al. investigated the time interval between the peak of the light curve in different energy bands, referred to as *spectral lag*. They found that more luminous bursts have shorter spectral lags [15]. Fenimore and Ramirez-Ruiz studied the *variability* of the light curve and suggested that more luminous bursts have more variable light curves. Variability is a measure of the deviation of the light curve from a smoothed version of the light curve [16].

2.1.4 Photon Spectrum

Observations show a non-thermal photon spectrum of GRBs. The energy flux peaks at few hundred keV and has a long high energy tail, which in some cases extends up to GeV. The prompt spectrum is usually well described by a smoothly joining broken power law, the *Band-function* [17]:

$$\epsilon_\gamma^2 \frac{\mathrm{dN}_{\epsilon_\gamma}}{\mathrm{d}\epsilon_\gamma} \propto \begin{cases} \epsilon_\gamma^{-\alpha} & \epsilon_\gamma \leq \epsilon_\gamma^b \\ \epsilon_\gamma^{-\beta} & \epsilon_\gamma \geq \epsilon_\gamma^b \end{cases} \tag{2.5}$$

We quote the photon spectrum weighted with E^2 to make it comparable to the neutrino energy spectrum, which will be introduced in section 2.2.5 and is usually weighted in this way.
Three independent spectral parameters are involved describing the photon spectrum: the low-energy photon spectral index α, the high-energy photon spectral index β and the break energy ϵ_γ^b. The spectral indices of different bursts are usually scattered around average values $\alpha \sim -1$ and $\beta \sim 0$. The shape of the spectrum can be explained by synchrotron radiation of electrons in internal shock fronts within the jets. It is illustrated for the average spectral parameters in figure 2.4. The break at an energy of typically $\epsilon_\gamma^b \sim 250\,\mathrm{keV}$ is due to Inverse Compton Scattering or to cooling of electrons at high energies [18]. Theoretical estimations allow the calculation of the neutrino energy spectrum from the observed photon energy spectrum (see section 2.2.5).

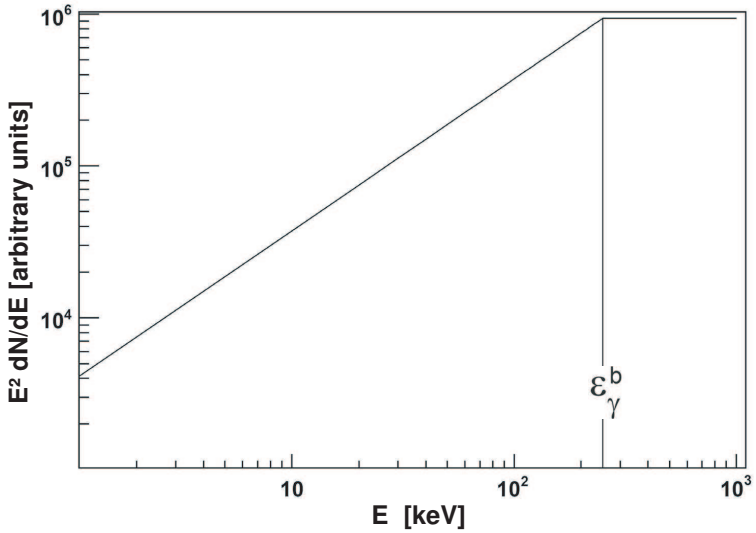

Figure 2.4: The prompt photon energy spectrum is usually well described by a broken power law. The displayed average spectrum breaks at $\epsilon_\gamma^b \sim 250\,\mathrm{keV}$ with a low-energy spectral index $\alpha \sim -1$ and a high-energy spectral index $\beta \sim 0$ (see equation 2.5).

2.1.5 Afterglow Emission

GRBs are followed by lower energetic, long-lasting emission in the X-ray, optical, infrared and radio wavelength: the afterglow. In some cases the afterglow has been observed several years after the burst. Afterglows are broad band and in each band the light curve generally decays following a powerlaw. Not all bursts have afterglows detected in all bands. X-ray afterglows are most commonly detected while radio afterglows are detected in roughly 50% of all GRB afterglow detections. Optical observations of detected X-ray afterglows exist for 60% of bursts detected by BeppoSAX[3] and 90% of bursts detected by HETE[4]. Bursts without observed optical afterglow are referred to as *dark bursts*. The lack of an optical afterglow might occur due to dust extinction, high redshift or the intrinsically faint nature of the burst.
Afterglow localization measurements enabled the identification of host galaxies. These are consistent with the association of GRBs with star-forming regions, which gives evidence of GRBs following the star forming rate and indicates that their progenitors might be massive stars, because these have the shortest lifetime. Knowing the host galaxy enables the determination of the corresponding redshift in most cases. The observed redshifts range from 0.16 to 4.5. Some GRBs can be associated with supernovae and stellar collapses, because their afterglow light curve shows a supernova signature [19].
Breaks in the afterglow light curve indicate that the emission is beamed with beam opening angles of a few degrees (see section 2.2.3). [9] [20]

[3]http://www.asdc.asi.it/bepposax/
[4]http://space.mit.edu/HETE/

2.2 The Relativistic Fireball Shock Model

According to the *Relativistic Fireball Shock Model* GRB photons are produced by dissipation of kinetic energy of an ultrarelativistic flow. First proposed by Paczyński [21] and further enhanced by Rees and Mészáros [21] [22] the model explains the production process of GRBs, but it leaves open, what kind of inner engine accelerates the relativistic ejecta. The prediction of relativistic movement is necessary to solve the *Compactness Problem*, which is the combination of the fact that GRBs are cosmological events emitting an enormous amount of energy in a short time period, with the observed non-thermal photon spectrum.
A non-thermal spectrum requires an optically thin medium where only a few interactions take place. Non-relativistic calculations for the photon density and the pair production cross section (involving the variability and the distance) result in impossible conditions for an optically thin medium. However, introducing relativistic movement of the source changes the relation between variability and distance by a factor of Γ, the Lorentz factor of the ejecta, and could therefore solve the compactness problem.
The Fireball shock model predicts an inner engine producing a relativistic flow. Its kinetic energy is dissipated by internal and external shocks, described in more detail in sections 2.2.2 and 2.2.2. Internal shocks happen within irregular flows between faster and slower shells while external shocks take place between the flow and the circumburst medium. The *Internal-External shocks model* assumes that internal as well as external shocks take place. It is illustrated in Figure 2.7. The shocks generate strong magnetic fields and accelerate electrons and protons. A brief introduction to the acceleration process is given in section 2.2.1. The observed gamma-rays are emitted by relativistic electrons via synchrotron radiation and inverse Compton scattering. The emission is assumed not isotropic but beamed (see section 2.2.3).

2.2.1 Fermi Acceleration

Fermi acceleration at a strong shock is usually considered to produce the observed cosmic ray spectrum [23]. Individual charged particles can gain many times of their initial energy in the transfer of macroscopic energy contained in a moving magnetized plasma. This results in a characteristic non-thermal energy distribution. One has to distinguish first and second order Fermi acceleration. Acceleration at a shock front is referred to as first order Fermi acceleration, whereas second order Fermi acceleration describes the acceleration by randomly moving, partially ionized gas clouds. Second order Fermi acceleration was suggested first by Fermi in 1949 [24] while first order Fermi acceleration was proposed in 1978 (see e.g. [23]). The following descriptions are based on [25].

Second Order Fermi Acceleration

A magnetized cloud of plasma moves with velocity $\vec{V}$ and a relativistic charged particle encounters the cloud with an energy E_{in} and an angle θ_{in} relative to the velocity of the

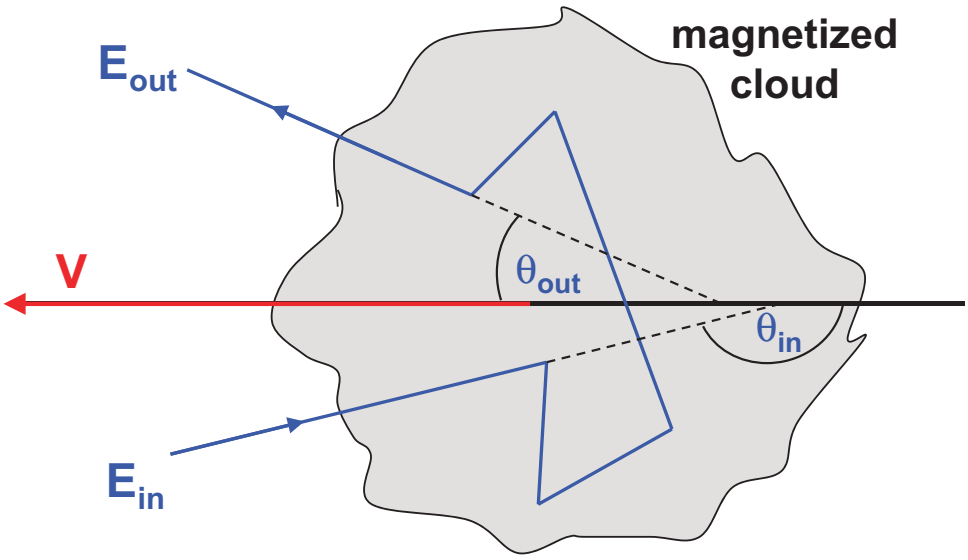

Figure 2.5: Second order Fermi acceleration: A relativistic particle encounters a moving magnetized cloud. The particle enters the cloud with an energy E_{in} and an angle θ_{in} relative to the velocity of the cloud, is deflected within the cloud and leaves it with an angle θ'_{out} relative to the velocity of the cloud and an energy E'_{out} in the cloud's rest frame

cloud (illustrated in figure 2.5). In the rest frame of the moving cloud the particle has a total energy

$$E'_{\mathrm{in}} = \gamma E_{\mathrm{in}}(1 - \beta\cos(\theta_{\mathrm{in}})), \tag{2.6}$$

with $\beta = V/c$, where c is the speed of light, and $\gamma = (1-\beta^2)^{-1/2}$. Within the cloud the particle scatters elastically deflected by the magnetic fields, without collisional energy loss. The particle escapes from the cloud with an angle θ'_{out} and an energy $E'_{\mathrm{out}} = E'_{\mathrm{in}}$ in the cloud's rest frame. Transformation to the laboratory frame yields

$$E_{\mathrm{out}} = \gamma E'_{\mathrm{out}}(1 + \beta\cos(\theta'_{\mathrm{out}})). \tag{2.7}$$

The relative change in energy is given by

$$\epsilon = \frac{E_{\mathrm{out}} - E_{\mathrm{in}}}{E_{\mathrm{in}}} = \frac{1 - \beta\cos(\theta_{\mathrm{in}}) + \beta\cos(\theta'_{\mathrm{out}}) - \beta^2\cos(\theta_{\mathrm{in}})\cos(\theta'_{\mathrm{out}})}{1-\beta^2} - 1. \tag{2.8}$$

To obtain an average change in energy, the average over all angles θ_{in} and θ'_{out} is calculated. Both angles range from 0° to 180°. The average is given by

$$\langle \cos(\theta) \rangle = \frac{\int_{-1}^{1} \mathrm{d}\cos(\theta) \cos(\theta) \frac{\mathrm{dn}}{\mathrm{d}\cos(\theta)}}{\int_{-1}^{1} \mathrm{d}\cos(\theta) \frac{\mathrm{dn}}{\mathrm{d}\cos(\theta)}}. \tag{2.9}$$

Directions inside the cloud are isotropic ($\frac{\mathrm{dn}}{\mathrm{d}\cos(\theta'_{\text{out}})} = \text{const.}$) and therefore

$$\langle \cos(\theta'_{\text{out}}) \rangle = 0. \tag{2.10}$$

The probability of a collision is proportional to the relative velocity between the cloud and the particle. Since the cloud is moving, the number of particles entering from the moving direction is expected to be larger than the number of particles from the opposite moving direction. The distribution depends on the velocity of the cloud:

$$\frac{\mathrm{dn}}{\mathrm{d}\cos(\theta_{\text{in}})} = \frac{c - V\cos(\theta_{\text{in}})}{2c} \ . \tag{2.11}$$

In this case the average becomes $\langle \cos(\theta_{\text{in}}) \rangle = -\frac{V}{3c}$. This results in an average change in energy of

$$\langle \epsilon \rangle = \frac{\langle E_{\text{out}} - E_{\text{in}} \rangle}{E_{\text{in}}} = \frac{\frac{4}{3}\beta^2}{1 - \beta^2} \ . \tag{2.12}$$

The particle can encounter several clouds until it escapes from the acceleration region. The energy change is $\Delta E = \langle \epsilon \rangle E$ per encounter. For an injection energy of E_0 the energy after n encounters is given by

$$E_n = E_0(1 + \langle \epsilon \rangle)^n. \tag{2.13}$$

For each encounter the particle escapes with a probability P_{esc}, after n encounters the escape probability is given by $(1 - P_{\text{esc}})^n$. In each encounter the particle enters and leaves the cloud. Depending on the angle the particle loses or gains energy, but after many encounters the particle will receive a net energy gain.

First Order Fermi Acceleration

A plane shock front moves with the velocity $-\vec{V}_{\text{shock}}$. Shocked gas flows away from the shock with the velocity $\vec{V}_{\text{rel}}$ relative to the shock front and $|\vec{V}_{\text{rel}}| < |\vec{V}_{\text{shock}}|$. Gas behind the shock moves with $\vec{V}_{\text{down}} = -\vec{V}_{\text{shock}} + \vec{V}_{\text{rel}}$. A sketch can be found in figure 2.6. Interpreting the shocked gas velocity, also referred to as "downstream", relative to the unshocked gas ("upstream") from the interstellar medium (ISM) allows application of equation 2.8 to this situation as well. In both, the upstream and downstream gas the particle directions are isotropic. Therefore, averaging over all angles yields

$$\langle \cos(\theta'_{\text{out}}) \rangle = -\langle \cos(\theta_{\text{in}}) \rangle = \frac{2}{3} \ , \tag{2.14}$$

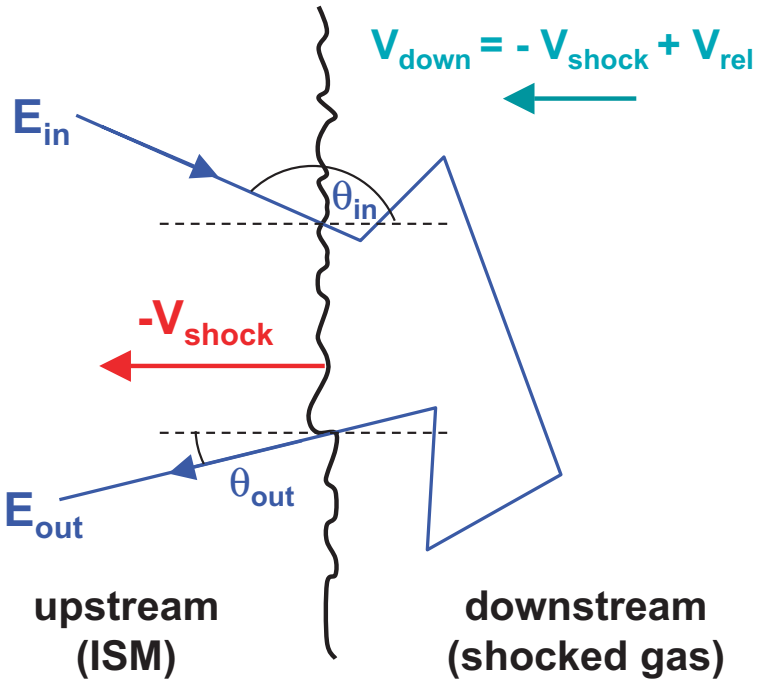

Figure 2.6: First order Fermi acceleration: A relativistic particle from the interstellar medium (ISM) encounters a shock front that moves with velocity $-V_{\text{shock}}$. Shocked gas flows away from the shock with the velocity $\vec{V}_{\text{rel}}$ relative to the shock front and $|\vec{V}_{\text{rel}}| < |\vec{V}_{\text{shock}}|$. Gas behind the shock moves with $\vec{V}_{\text{down}} = -\vec{V}_{\text{shock}} + \vec{V}_{\text{rel}}$. The particle enters the cloud with an energy E_{in} and an angle θ_{in} relative to the shock front and leaves it with an energy E_{out} in the cloud's rest frame and an angle θ_{out} relative to the velocity of the cloud.

where θ'_{out} ranges from -90° to 90° and θ_{in} takes values between 90° and 270°.
Inserting this in equation 2.8 gives an average energy change of

$$\langle \epsilon \rangle = \frac{1 + \frac{4}{3}\beta + \frac{4}{9}\beta^2}{1 - \beta^2}. \tag{2.15}$$

A particle can move several times back and forth across the shock. Assuming an infinite plane shock results in an energy gain for each encounter[5]. Therefore, the first order Fermi acceleration is more effective compared to the second order and in fact, the second order Fermi acceleration is irrelevant for acceleration.
According to the fireball model particles, accelerated in shocks, produce the GRB. Thus, the acceleration process can be described by first order Fermi acceleration.

[5]This is because $\cos(\theta'_{\text{out}})$ is always positive, while $\cos(\theta_{\text{in}})$ is always negative.

2.2.2 Internal-External Shocks Model

The Internal-External Shocks model predicts that both, internal and external shocks, take place in the relativistic flow (see figure 2.7).

Internal Shocks

The inner engine produces an irregular flow of short duration T ($\sim 50\,\mathrm{s}$). The flow varies on a small time scale δt, which corresponds to the variability of the observed GRB light curve with $\delta t \sim 1\,\mathrm{s}$. The internal shocks take place at a radius $R \sim 10^{13} - 10^{14}\,\mathrm{cm}$ (comparable to the distance between Sun and Earth of $1\,\mathrm{AU} = 1.5 \cdot 10^{13}\,\mathrm{cm}$) and are responsible for the prompt gamma emission. The forward inner shocks last as long as the inner engine is active. Only a fraction of the initial kinetic energy is dissipated during the internal shocks. The remaining fraction will be dissipated later by external shocks caused by collisions with the surrounding matter. [26]

External Shocks

The external shocks with the circumburst matter of the ISM take place at a radius $R \sim (10^{14} - 10^{16})\,\mathrm{cm}$. They slow down the ejected particles and are responsible for the long lasting afterglow. At the initial stage of the external shock a short lived reverse shock propagates into the ejecta and produces optical and UV emission. It stops when it runs out of matter as it reaches the inner edge of the flow. [26]

2.2.3 Collimation of Emission

According to the fireball model, the GRB emission is not isotropic but beamed. Calculation of the total energy, assuming an isotropic emission, leads to values up to $10^{54}\,\mathrm{ergs}$, which are unreasonable for any compact source [6]. Significant beaming would reduce the calculated total amount of emitted energy. Due to relativistic effects it is not possible to distinguish a jet from a spherical expanding shell if $\theta > \Gamma^{-1}$, where θ is the jet opening angle. An observer on the beam only receives information from within the relativistic light cone and does not know if, outside the cone, the emitter is radiating or not. This is because the angular distribution of the radiation intensity of an accelerated particle peaks at $\theta \sim \Gamma^{-1}$ for $\beta \to 1$.
As the jet slows down by going through the interstellar medium and Γ decreases, eventually the relativistic beam becomes wider. Radiation and material start to expand sideways when $\theta \sim \Gamma^{-1}$. This effect results in a break in the light curve. Beaming corrections of the observed energy suggest that all bursts have a comparable corrected energy of $\sim 10^{51}\,\mathrm{ergs}$. The observed energy, if assumed isotropic, varies due to variations in the jet opening angle. [27]

[6] For typical burst durations this results in a luminosity of 10^{53}-$10^{54}\,\mathrm{ergs/s}$. The brightest observed sources besides GRBs are quasars with a luminosity of 10^{45}-$10^{48}\,\mathrm{ergs/s}$.

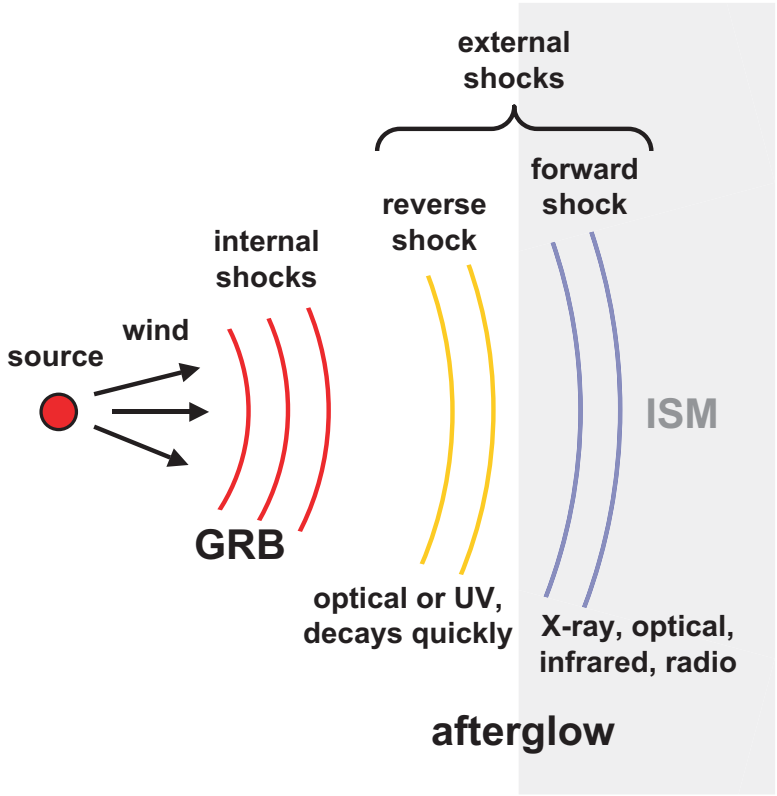

Figure 2.7: The Internal-External Shock Scenario: Internal shocks between faster and slower shells are responsible for the GRB itself, the external shock produces the long duration afterglow emission and a short lived reverse shock creates optical and UV emission (from [26]).

2.2.4 Inner Engine of GRBs

The fireball model requires several conditions for the inner engine:

- It must be able to generate large energies of $\sim 10^{51}$ ergs and to accelerate $10^{-5} M_{\odot}$ to relativistic velocities.
- It must be able to collimate the emission.
- Fast variations in the light curve (~ 10 ms) indicate that the inner engine must be a compact object. Average durations of ~ 50 s exclude an energy release in one single explosion.

Present observations like the following ones might give a clue about the inner engine:

- Two classes of bursts might indicate the existence of two different progenitors.
- GRBs are rare.
- There might be an association with supernovae.

- GRBs are distributed isotropically and seem to follow the star formation rate.

Many models are ruled out by these requirements. Candidates for the inner engine are "Collapsars" for long bursts and neutron-star neutron-star mergers or neutron-star black-hole mergers for short bursts. Beaming arises naturally in binary merger models, because flow is emitted preferably along the rotation axis. However, it can also be explained for collapsars, which are massive rotating stars ($M > 25 \cdot M_{\odot}$) forming a black hole after a core collapse. The rest of the star forms a massive accretion disk while falling into the black hole. Rapid accretion of stellar matter into the black hole results in large energy releases and heated gas at the pole expands in a jet-like fireball, which penetrates the shell of the stellar surface [26] [9].

2.2.5 Neutrino Spectrum

According to the fireball model electrons are shock accelerated. It is expected that protons are accelerated in the same process. Photons are produced by synchrotron radiation of accelerated electrons. In photoproduction mechanisms pions are created with a very large cross-section of $\sigma_{\Delta} \sim 5 \cdot 10^{-28}\,\mathrm{cm}^2$ in the following Δ-resonance processes

$$p\gamma \rightarrow \Delta^{+} \rightarrow n\pi^{+} \tag{2.16}$$

and

$$p\gamma \rightarrow \Delta^{+} \rightarrow p\pi^{0}. \tag{2.17}$$

The pions decay subsequently. Charged pions produce neutrinos in the decay:

$$\pi^{+} \rightarrow \nu_{\mu}\mu^{+} \rightarrow \nu_{\mu}e^{+}\nu_{e}\bar{\nu}_{\mu}\ . \tag{2.18}$$

Neutrinos can also be produced in *pp* collisions, but the proton density in the relativistic flow is too low to allow significant conversion of energy to neutrinos in this process.
Since the synchrotron photons are believed to induce the pion creation, which results in a neutrino creation in the pion decay, the GRB is expected to take place in coincidence with the neutrino emission. The time delay for neutrinos with a typical expected energy of $10^{14}\,\mathrm{eV}$ and mass m_{ν} travelling 100 Mpc is only $\sim 10^{-11}(m_{\nu}/10\,\mathrm{eV})^2\,\mathrm{s}$ [28]. Therefore, this coincidence is conserved on the way from the source to the observer.
The following results are derived assuming that photo-meson productions are dominated by the contribution of the Δ-resonance. To produce the Δ-resonance in a photon-proton-interaction, the proton needs to exceed a certain center of mass energy threshold. Momentum and energy conservation lead to the following equation in the co-moving system which is fixed to the progenitor's rest frame. Quantities in the co-moving frame are marked with a prime while the quantities in the observer's frame are unprimed.

$$2\epsilon'_p\epsilon'_\gamma = (m_{\Delta}^2 - m_p^2)c^4 + 2\cos(\theta')\epsilon'_\gamma\sqrt{\epsilon'^2_p - m_p^2c^4} \tag{2.19}$$

where θ' describes the angle between photon and proton momentum in the co-moving frame. Inserting the relation $\cos(\theta') \leq 1$ yields

$$\epsilon'_p \geq \frac{(m_\Delta^2 - m_p^2)c^4}{4\epsilon'_\gamma} + \frac{m_p^2 \epsilon'_\gamma}{(m_\Delta^2 - m_p^2)}. \tag{2.20}$$

For typical $\epsilon'_\gamma \sim 1$ MeV the second summand is negligibly small (1.4 MeV) compared to the first summand (159495 MeV). Thus we can neglect the second summand:

$$\epsilon'_p \geq \frac{(m_\Delta^2 - m_p^2)c^4}{4\epsilon'_\gamma}. \tag{2.21}$$

The charged pion decay creates four leptons. Assuming equipartition of the initial energy among the decay products, each lepton has $\frac{1}{4}$ of the initial pion energy. The pion produced in the Δ-resonance process receives a fraction $\langle x_{p\to\pi} \rangle \simeq 0.2$ (see equation 2.28 for a more detailed calculation) of the energy of the initial proton. Inserting $m_\Delta = 1232\,\mathrm{MeV}$ and $m_p = 938\,\mathrm{MeV}$ [29] and changing from the co-moving frame to the observer's frame yield the resulting neutrino energy

$$\epsilon_\nu = \frac{1}{4}\langle x_{p\to\pi} \rangle \epsilon_p \geq 7 \times 10^3 \Gamma^2 \frac{\mathrm{MeV}^2}{(1+z)^2 \epsilon_\gamma}, \tag{2.22}$$

where Γ is the plasma expansion (bulk) Lorentz factor and z the burst's redshift. For $\Gamma < 100$ the medium is optically thick to photons and for $\Gamma > 1000$ protons lose most of their energy by synchrotron radiation. Therefore, the boost factor is constrained to $100 < \Gamma < 1000$ [18]. Because the co-moving frame is fixed to the progenitor's rest frame one has to correct for the ejection of the plasma (with the boost factor Γ) and for the expansion of the universe according to the Hubble law. Additionally, the energy transformation is dependent on Γ and z via $E' = E(1+z)/\Gamma$. Equation 2.22 is valid for any ϵ_γ and ϵ_p, so we find the following relation between photon and neutrino break energy:

$$\epsilon_\nu^b \simeq 7 \times 10^3 \Gamma^2 \frac{\mathrm{MeV}^2}{(1+z)^2 \epsilon_\gamma^b}. \tag{2.23}$$

High energy pions may lose some energy by synchrotron radiation before they decay. The neutrinos produced in the pion decay therefore have reduced energy, which results in a second break of the neutrino spectrum at $\epsilon_\nu = \epsilon_\nu^s$. At neutrino energies $\epsilon_\nu \gg \epsilon_\nu^s$ the probability that a pion would decay, before losing energy via synchrotron radiation, can be estimated by

$$\frac{\tau_\pi^s}{\tau_\pi} = \left(\frac{\epsilon_\nu}{\epsilon_\nu^s}\right)^{-2}, \tag{2.24}$$

where τ_π is the decay time of the pion and τ_π^s its synchrotron loss time. The decay time in the observer's frame is proportional to the energy, while the synchrotron loss time is inverserely proportional to the energy [30]. The intensity is suppressed by the

same factor. The second break in the neutrino spectrum depends on the neutrino flavor[7]. The following calculations will be valid for muon neutrinos. The synchrotron loss effect becomes important when the pion lifetime becomes comparable to the synchrotron loss time. Estimation of the synchrotron lifetime allows the estimation of a second break energy in the neutrino spectrum at higher energy than the first break energy ϵ_ν^b. Above this second break energy (according to [18])

$$\epsilon_\nu^s = \frac{10^{28}}{1+z}\sqrt{\frac{\varepsilon_e}{\varepsilon_B L_\gamma/\mathrm{ergs}}}\Gamma^4 t_v/\mathrm{s\ MeV}, \tag{2.25}$$

the neutrino spectrum falls off faster with spectral index $(\alpha - 2)$ according to the factor given in equation 2.24. ε_e and ε_B are the fractions of the burst's internal energy converted to kinetic energy of electrons and to the magnetic field respectively. There is no good way of determining these equipartition functions theoretically yet. L_γ is the observed gamma-ray luminosity and t_v the time difference between the emission of different shells [31]. Finally, the relation between photon and neutrino energy $\epsilon_\nu \propto \epsilon_\gamma^{-1}$ (see equation 2.22) and the correction for the synchrotron energy loss of the pions yield the neutrino energy spectrum [31]:

$$\epsilon_\nu^2 \frac{\mathrm{dN}_{\epsilon_\nu}}{\mathrm{d}\epsilon_\nu} \approx A_\nu \times \begin{cases} \left(\frac{\epsilon_\nu}{\epsilon_\nu^b}\right)^{\beta+1} & \epsilon_\nu < \epsilon_\nu^b \\ \left(\frac{\epsilon_\nu}{\epsilon_\nu^b}\right)^{\alpha+1} & \epsilon_\nu^b < \epsilon_\nu < \epsilon_\nu^s \\ \left(\frac{\epsilon_\nu}{\epsilon_\nu^b}\right)^{\alpha+1}\left(\frac{\epsilon_\nu}{\epsilon_\nu^s}\right)^{-2} & \epsilon_\nu > \epsilon_\nu^s \end{cases}, \tag{2.26}$$

where the spectral indices α and β are the parameters used to describe the photon energy spectrum (see equation 2.5).
The AMANDA detector is mainly sensitive to neutrino energies in the region around the typical first break. The spectrum is normalized to the photon fluence F_γ, which is assumed to be proportional to the neutrino luminosity [18]:

$$A_\nu = \frac{1}{8}\frac{1}{f_e}\frac{F_\gamma}{\ln(10)} f_\pi. \tag{2.27}$$

The factor 1/8 is due to the fact that half of the photo-hadronic interactions result in four leptons. f_e is the fraction of total energy in electrons compared to protons in the jet, f_π the fraction of proton energy transferred to the pions. The latter is given by [18]:

$$f_\pi \sim 0.2 \cdot 10^{-44} \cdot \frac{L_\gamma/\mathrm{erg}}{\Gamma^4\,(t_v/\mathrm{s})\,(\epsilon_\gamma^b/\mathrm{MeV})}. \tag{2.28}$$

This normalization is valid for the ν_μ-flux at the source. The ν_e- and $\bar{\nu}_\mu$-flux is approximately the same. The flavor ratio at the source (ν_e:ν_μ:ν_τ)=(1:2:0) changes due to oscillations[8] (see also section 2.2.6) to (1:1:1) on Earth. The total all flavor neutrino flux

[7] At high energies the muon will lose energy due to synchrotron radiation before its decay. Therefore, the ν_e and the $\bar{\nu}_\mu$ will receive less energy than the ν_μ created in the pion decay.
[8] assuming distance to Earth $\gg$ oscillation length

Table 2.1: Average parameters determining the neutrino spectrum. Since all of the parameters fluctuate strongly, these values can only be taken as rough benchmarks.

Parameter	Symbol	Average Value
Photon flux	F_γ	$(10^{-4}$ - $10^{-6})$ erg/cm^2
Electron-proton total energy ration	f_e	~ 0.1
Energy fraction transfered form p to π	f_π	~ 0.2
First neutrino break energy	ϵ_ν^b	$\sim 10^5$
Second neutrino break energy	ϵ_ν^s	$\sim 10^7$
First photon spectral index	α	$\sim$ -1
Second photon spectral index	β	~ 0

at the source is assumed to be ~ 3 times the ν_μ-flux at the source. Only $\frac{1}{3}$ of this flux will reach the Earth in form of ν_μ- or $\bar{\nu}_\mu$-flux. Therefore, the expected ν_μ- or $\bar{\nu}_\mu$-flux on Earth is equal to the produced ν_μ-flux at the source.
The spectral indices of the neutrino spectrum can be obtained directly by the Band fit of the photon spectrum. The fit parameters are not universal. The parameters, and therefore the neutrino spectra, can differ significantly for individual bursts. Another essential parameter in the neutrino flux calculation is the redshift, since strong redshift evolution is expected due to the connection of GRBs to the star formation rate [18].

Average Neutrino Spectrum

Typical values for the parameters determining the neutrino spectrum are given by Becker et al. [18], some are summarized in Table 2.1. Since all of the parameters fluctuate strongly, these values can only be taken as rough benchmarks. In cases of lacking photon spectrum measurements, there is no other way of obtaining the neutrino spectrum. The shape of this average neutrino spectrum is displayed in figure 2.8. Inserting these values in Equation 2.27 yields:

$$A_\nu = (6.77 \cdot 10^{-3} - 6.77 \cdot 10^{-5})\,\mathrm{GeV\,cm^{-2}}. \tag{2.29}$$

Assuming a typical burst duration of $T = 50\,\mathrm{s}$ yields to the following per burst flux per second.

$$\frac{A_\nu}{T} = (1.35 \cdot 10^{-4} - 1.35 \cdot 10^{-6})\,\mathrm{GeV\,cm^{-2}\,s^{-1}}. \tag{2.30}$$

This normalization for a single burst can be modified to a diffuse normalization by the multiplication with the number of bursts per year (666 long bursts per year) and dividing by $4\pi\,\mathrm{sr}$:

$$A_\nu^{diff} = (1.14 \cdot 10^{-8} - 1.14 \cdot 10^{-10})\,\mathrm{GeV\,cm^{-2}\,s^{-1}\,sr^{-1}}. \tag{2.31}$$

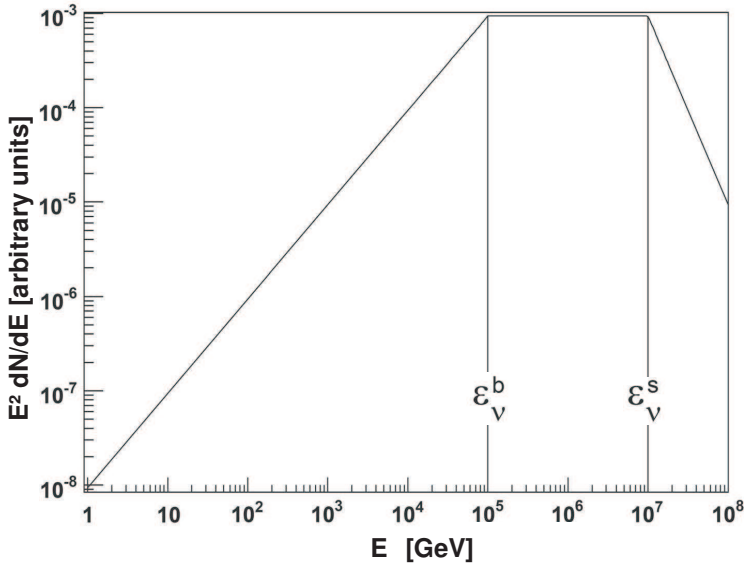

Figure 2.8: The neutrino energy spectrum can be derived from the photon energy spectrum. The displayed average spectrum breaks at $\epsilon_\nu^b \sim 10^5\,\mathrm{GeV}$ with a low energy spectral index $\alpha \sim -1$ and a high energy spectral index $\beta \sim 0$. A second break due to synchrotron energy loss appears at $\epsilon_\nu^s \sim 10^7\,\mathrm{GeV}$ above which the spectrum decays faster.

Previous analyses used the normalization of the diffuse flux calculated by E. Waxman (for more details see [32]) as a benchmark.

$$A_\nu^{diff,WB} = 4.5 \cdot 10^{-9}\,\mathrm{GeV\,cm^{-2}\,s^{-1}\,sr^{-1}} \tag{2.32}$$

The resulting per burst flux normalization is

$$A_\nu^{WB} = 5 \cdot 10^{-5}\,\mathrm{GeV\,cm^{-2}\,s^{-1}}. \tag{2.33}$$

2.2.6 Neutrino Oscillation

Due to oscillations, neutrinos produced at the source change their flavor on their way to the Earth. The weak eigenstates ν_α ($\alpha = (e, \mu, \tau)$) are not identical to the mass eigenstates ν_i ($i = (1, 2, 3)$). They are connected by the unitary Maki-Nakagava-Sakata-matrix (MNS-matrix) U:

$$|\nu_\alpha\rangle = \sum_{i=1}^{3} U_{\alpha i}^* |\nu_i\rangle \ . \tag{2.34}$$

Assuming three neutrinos, U is given by

$$U = \begin{pmatrix} c_{12}c_{13} & s_{12}c_{13} & e^{-i\delta} \\ -s_{12}c_{23} - c_{12}s_{23}s_{13}e^{i\delta} & c_{12}c_{23} - s_{12}s_{23}s_{13}e^{i\delta} & s_{23}c_{13} \\ s_{12}s_{23} - c_{12}s_{23}s_{13}e^{i\delta} & -c_{12}s_{23} - s_{12}c_{23}s_{13}e^{i\delta} & c_{23}c_{13} \end{pmatrix} \times \mathrm{diag}(\mathrm{e}^{\mathrm{i}\alpha_1/2}, \mathrm{e}^{\mathrm{i}\alpha_2/2}, 1), \tag{2.35}$$

with $s_{ij} = \sin(\theta_{ij})$ and $c_{ij} = \cos(\theta_{ij})$ $(i, j = 1, 2, 3)$. θ_{ij} are the mixing angles and δ, α_1 and α_2 are CP-violating phases. The Majorana phases, α_1 and α_2, only have physical influences if neutrinos are identical to their antiparticles (Majorana particles), they do not affect neutrino oscillation. [33] [34]
Assuming that the oscillation length is very small compared to the distance between source and detector the probability of an oscillation from flavor α to flavor β after a distance L for a neutrino with energy E is:

$$P(\nu_\alpha \to \nu_\beta; L) = |\langle \nu_\beta | \nu_\alpha(x) \rangle|^2 = \delta_{\alpha\beta} - \sum_{i \neq j} U^*_{\alpha i} U_{i\beta} U^*_{\beta j} U_{j\alpha} \left(1 - \exp\left(\frac{-i\Delta m^2_{ij} L}{2E}\right)\right), \tag{2.36}$$

dependent on the neutrino mass difference Δm^2_{ij} between two mass eigenstates. Averaging over rapid oscillations yields in the limit $L \to \infty$

$$\langle P_{\alpha,\beta} \rangle = \langle P(\nu_\alpha \to \nu_\beta; L = \infty) \rangle = \delta_{\alpha\beta} - \sum_{i \neq j} U^*_{\alpha i} U_{i\beta} U^*_{\beta j} U_{j\alpha} = \sum_j |U_{\alpha j}|^2 |U_{\beta j}|^2. \tag{2.37}$$

A cosmic mixed flavor neutrino flux on Earth $(\Phi_{Earth}(\nu_e), \Phi_{Earth}(\nu_\mu), \Phi_{Earth}(\nu_\tau))$ can be calculated from the expected neutrino flux at the source $(\Phi_{source}(\nu_e), \Phi_{source}(\nu_\mu), \Phi_{source}(\nu_\tau))$ [35]:

$$\begin{pmatrix} \Phi_{Earth}(\nu_e) \\ \Phi_{Earth}(\nu_\mu) \\ \Phi_{Earth}(\nu_\tau) \end{pmatrix} = \begin{pmatrix} \langle P_{ee} \rangle & \langle P_{\mu e} \rangle & \langle P_{\tau e} \rangle \\ \langle P_{e\mu} \rangle & \langle P_{\mu\mu} \rangle & \langle P_{\tau\mu} \rangle \\ \langle P_{e\tau} \rangle & \langle P_{\mu\tau} \rangle & \langle P_{\tau\tau} \rangle \end{pmatrix} \begin{pmatrix} \Phi_{source}(\nu_e) \\ \Phi_{source}(\nu_\mu) \\ \Phi_{source}(\nu_\tau) \end{pmatrix} \tag{2.38}$$

The flavor ratio at the GRB source $(\nu_e{:}\nu_\mu{:}\nu_\tau)$=(1:2:0) changes due to neutrino oscillations[9](see also section 2.2.6) to (1:1:1) at Earth.

2.3 The Cannonball Model

Besides the Fireball Model, the Cannonball Model provides a different theory to describe the experimental observations. The inner engine of a long duration GRB and its afterglow is believed to be an ordinary corecollapse supernova (SN) explosion. The SN forms a compact object surrounded by an accretion disk or torus made of stellar material. When parts of the accretion disk fall abruptly onto the compact object, a pair of cannonballs is emitted in opposite directions along the rotation axis. The cannonballs consist of atomic matter with very high bulk motion Lorentz factor $\Gamma \sim 1000$. Each time a part of the accretion disks falls onto the core, another pair of cannonballs is emitted and a collimated beam of cannonballs leaves the central object. Cannonballs, crossing the ambient light left by the SN surrounding the core, produce single pulses of the GRB. The electrons enclosed in the cannonball accelerate the photons up to GRB energies ($\sim$ 1 MeV) by inverse Compton scattering. Figure 2.9 sketches the scenario of the Cannonball Model. [36]
Pions are produced when the baryons contained in the cannonballs collide with the nuclei

[9]assuming distance to Earth $\gg$ oscillation length and maximal mixing angle

from the shell. Neutrinos with an energy of a few-hundred GeV are produced in the decay of charged pions [37].

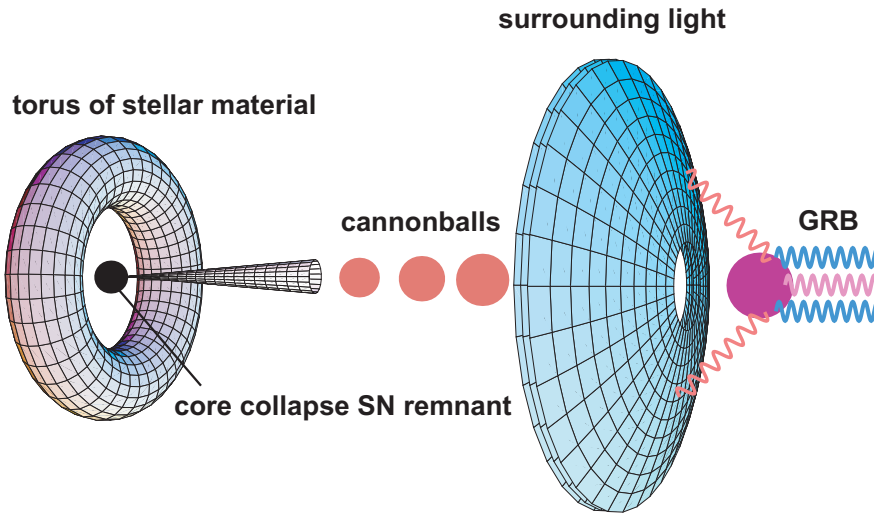

Figure 2.9: The Cannonball Model: A corecollapse SN forms a compact object surrounded by a torus of stellar material. Matter abruptly falling onto the core produces a collimated beam of cannonballs in opposite directions along the rotational axis. The cannonballs cross the surrounding light and accelerate the photons by inverse Compton scattering with enclosed electrons up to GRB energies (from [36]).

Chapter 3

Satellites

Earth orbiting satellites and space probes located in the solar system observe GRBs and provide astronomical locations of these short bursts. Some instruments are able to determine the direction of the incoming gamma-rays others can only trigger the event. The latter need the response of several satellites to provide directional information via the *triangulation method*. By timing the arrival of a GRB at several spacecrafts, its possible locations are restricted. Each pair of satellites provides an annulus of possible arrival directions. The center of the annulus is defined by the vector joining the two satellites. Its radius θ (in radian) is given by:

$$\cos(\theta) = \frac{c \cdot \Delta T}{D_{12}}, \tag{3.1}$$

where c is the speed of light, ΔT the difference in the two arrival times and D_{12} the distance between the two satellites. This triangulation method is illustrated in Figure 3.1.

3.1 The Third Interplanetary Network

The third interplanetary network (IPN[1]) consists of several spacecrafts equipped with GRB detectors. It began operations in 1990. First member of the network was the Ulysses spacecraft[2] launched by a NASA/ESA mission in 1990, followed by the Compton Gamma Ray Observatory equipped with the GRB detector BATSE. While they were operating, the Pioneer Venus Orbiter, the Mars Observer and the Near Earth Asteroid Rendezvous (NEAR) were included in the network. Today, main contributions come from Ulysses, WIND[3], the high energy transient explorer 2 (HETE-II)[4], 2001 Mars Odyssey[5],

[1] http://www.ssl.berkeley.edu/ipn3/
[2] http://helio.estec.esa.nl/ulysses/
[3] http://www-spof.gsfc.nasa.gov/istp/wind/
[4] http://space.mit.edu/HETE/
[5] http://mars.jpl.nasa.gov/odyssey/

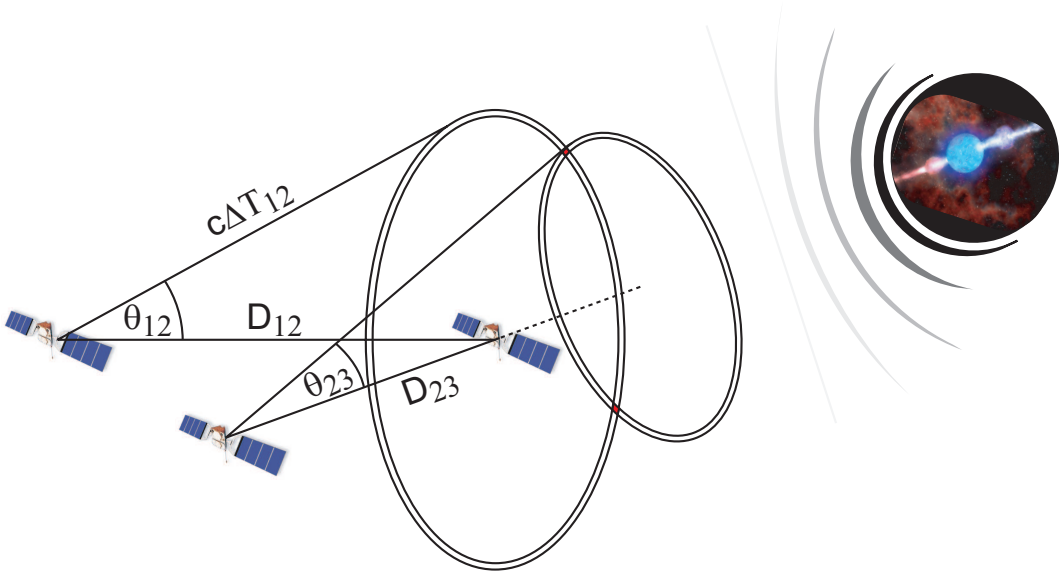

Figure 3.1: Each pair of satellites gives an annulus of possible arrival direction. Three satellites give two annuli, which intersect in two points. The source position is restricted to these two points.

INTEGRAL[6], RHESSI[7], Swift[8] and the Italian X-ray astronomy satellite BeppoSAX[9]. Most burst information used in this analysis is provided by the KONUS detector on the WIND spacecraft and Ulysses. Thus, these detectors are described in more detail in the following sections. Additionally, HETE-II is depicted as an example of direction sensitive detectors.
Start times and localization information of the IPN are summarized in the IPN catalog[10]. There, the bursts are characterized by their start time. Usually the burst trigger time is used to indicate the start time of a burst. This is reasonable if the sample of bursts is detected by only one satellite (e.g. BATSE). However, the IPN bursts are detected by several instruments at the same time and the triggered satellites might differ from burst to burst. Therefore, the IPN catalog quotes the time, when the detected emission at at least one detector rises significantly above the background. For satellites that are not on low Earth orbits, this start time is not identical with the Earth crossing time. KONUS-

[6]http://www.rssd.esa.int/index.php?project=INTEGRAL&page=index
[7]http://hessi.ssl.berkeley.edu/
[8]http://swift.gsfc.nasa.gov/docs/swift/swiftsc.html
[9]http://www.asdc.asi.it/bepposax/
[10]http://www.ssl.berkeley.edu/ipn3/interpla.html

Wind for example orbits up to 5 light seconds away from Earth. Regarding well localized GRBs, it is possible to correct for the delay caused by the distance between Earth and satellite with respect to the direction of the burst. In case of poor localizations, the Earth crossing time can only be constrained to a few seconds.
For the same reason it is not reasonable to use the T_{90} variable to quote the duration of the burst. T_{90}, which is the time interval over which a burst emits from 5% to 95% of its total number of measured photons, is not meaningful when different detectors observe the same event. The IPN detectors are different in many aspects: The detection medium differs. Some consist of CsI crystals, others of BGO or Ge crystals. The size of the effective area varies from detector to detector, it ranges from 20 cm^2 to thousands of cm^2. Some satellites operate outside the magnetosphere in very steady background conditions, others inside the magnetosphere in variable backgrounds. Their energy range can range from 25 to 150 keV for some detectors, while others have an energy range between 100 keV and several MeV. Some detectors have actual triggers, while others have no triggers at all, and simply stream all the data to Earth. Some instruments are collimated, so that they are restricted to a certain field of view, while others are isotropic, and still others are in low Earth orbit or low Mars orbit, so a part of the sky is blocked, while others are far from any planet. But even the collimated detectors generally can respond to GRBs outside their field of view, because the gamma-rays can penetrate the spacecraft and the shielding, so it is entirely possible for a detector to trigger on a burst outside its field of view. Further complications occur because the detectors, which comprise the IPN, are always changing as some missions end and others begin.
Instead of T_{90} a duration is used that represents the time during which the burst emits clearly detectable gamma-ray emission. This time window is larger than the T_{90} window and contains the T_{90} window for each triggered instrument.

3.1.1 Ulysses

The Ulysses spacecraft was launched in October 1990 and orbits on an elliptical, high-inclination heliocentric orbit. Its trajectory is illustrated in Figure 3.2. Ulysses' primary mission is to characterize the heliosphere as a function of solar latitude. In addition it carries the solar X-ray/cosmic gamma-ray burst experiment, which consists of two detector systems, the *hard* and the *soft X-ray detectors*. A burst detection issues a trigger signal and the instrument switches into a burst mode to record data with high time resolution. Comparisons with instruments on other spacecrafts allow an estimation of the trigger sensitivity of $10^{-7}\,\mathrm{ergs\,cm^{-2}\,s^{-1}}$. The power supply is provided by a radioisotope thermoelectric generator (RTG) containing 10 kg of ^{238}Pu.

The Hard X-ray Detector

The hard X-ray detector operates in the energy range of $15 - 150$ keV. It consists of two 3 mm thick CsI crystals with a diameter of 51 mm. The crystals are connected to

[11] http://ulysses.jpl.nasa.gov/mission/images/2ndorbitlg.jpg

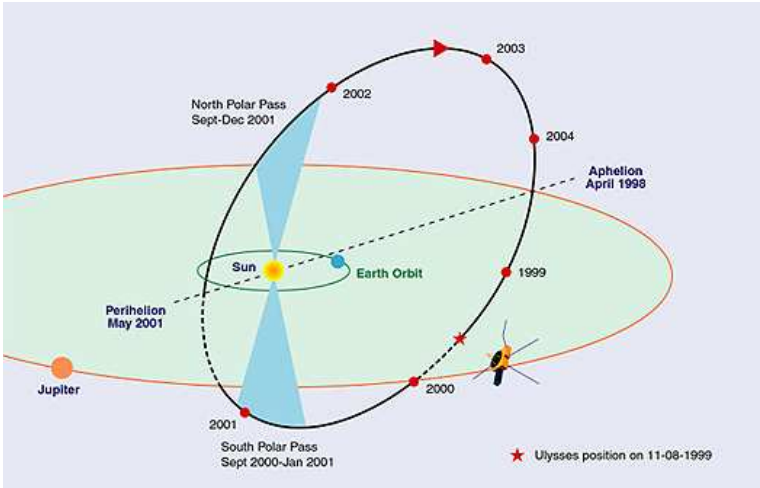

Figure 3.2: The Ulysses spacecraft is on an elliptical, high-inclination heliocentric orbit[11].

two photomultiplier tubes via plastic light guides. They are mounted on a boom far away from the RTG to reduce the background of high-energy gamma-rays produced in the RTG. The mounting provides an almost all-sky field of view and nearly isotropic response. The structure of the hard X-ray detector is displayed in Figure 3.3.

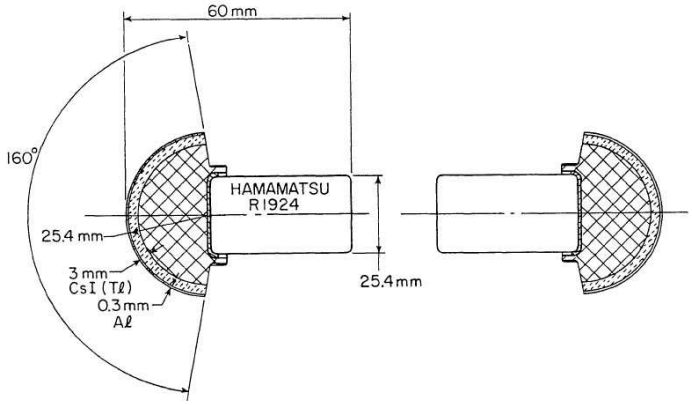

Figure 3.3: The hard X-ray detectors consist of two 3 mm thick CsI crystals with a diameter of 51 mm. They are mounted on a boom and thus have an omnidirectional response (from [38]).

The Soft X-ray Detector

The soft X-ray detector operates in the energy range of $5 - 20\,\mathrm{keV}$. It consists of two $500\,\mu\mathrm{m}$ Si surface barrier detectors with an area of $0.5\,\mathrm{cm}^2$. To shield the detector from low energy X-rays a thin beryllium foil is mounted in front of the detector and defines a

conical field of view of 150°. The detected pulses are amplified and analyzed by six-level discriminators, which define four differential energy channels and two integral channels. Figure 3.4 shows the schematic structure of the soft X-ray detector. [38]

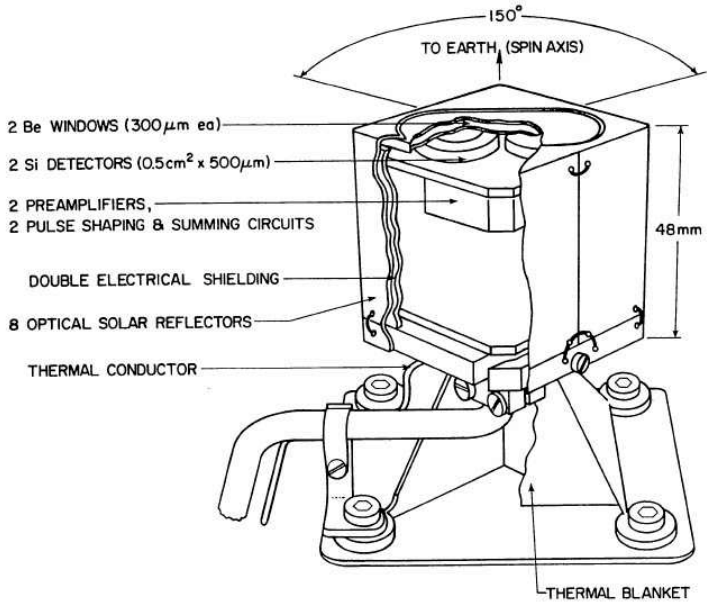

Figure 3.4: The soft X-ray detectors consist of two 500 μm Si surface barrier detectors with an area of 0.5 cm^2. A thin beryllium window rejects low energy X-rays (from [38]).

3.1.2 KONUS-Wind

The Wind spacecraft was launched in November 1994 and is orbiting the Earth, after a double lunar swing-by orbit it follows a halo orbit around the first Sun-Earth Lagrangian Point. The gamma-ray burst experiment KONUS, mounted on the Wind satellite, consists of two identical gamma-ray detectors S1 and S2, which observe the Southern and Northern ecliptic hemisphere. The detectors are large scintillators consisting of NaI(Tl) crystals 12.7 cm in diameter and 7.6 cm in hight, placed into an aluminum container covered with a beryllium entrance window. Each scintillator is read-out by a photomultiplier tube through a 20 mm thick lead glass. An illustration of one gamma-ray detector is shown in figure 3.5. The detectors operate in the energy range 5 keV - 10 MeV. Emission lines (0.511 MeV and 1.46 MeV) present in the naturally occurring background are used for in-flight calibrations to avoid carrying radioactive sources aboard. The instrument has two modes of operation: the background mode and the burst mode. The burst mode is activated when the signal exceeds the 6σ trigger threshold, which corresponds to a sensitivity of $(1-5)\cdot 10^{-7}\,\mathrm{erg\,cm^{-2}\,s^{-1}}$. An energy spectrum is recorded with a time resolution ranging between 2 ms and 256 ms.
The two identical detectors are mounted on long arms on each face of the spacecraft pointing parallel to its spin-axis. The ratio of the S1 and S2 count rates allow an estimation

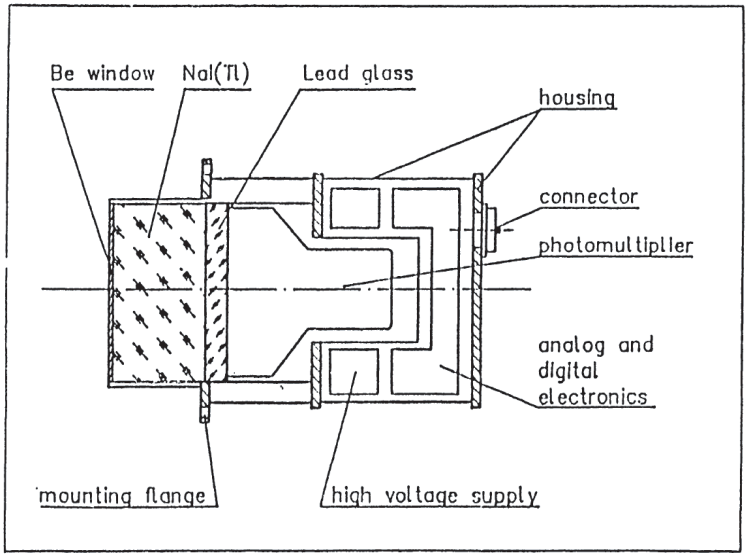

Figure 3.5: The KONUS gamma-ray sensor consists of a NaI(Tl) scintillator shielded with beryllium and is read-out by a photomultiplier tube.

of the burst localization (via the triangulation method) with an accuracy of $5° - 10°$. A illustration of the Wind spacecraft can be seen in figure 3.6.

3.1.3 HETE-II

The HETE-II satellite was launched in October 2000. Its primary goal is the determination of the origin and nature of cosmic GRBs. Broad-band observations and accurate localizations of GRBs are provided within several seconds of the burst duration. The spacecraft is on an equatorial orbit with an inclination of 2° and 600 km altitude. It carries three instruments: the *FREnch GAmma TElescope* (FREGATE), the *Wide-field X-ray Monitor* (WXM) and the *Soft X-ray Camera* (SXC), which are usually pointed towards the anti-sun direction. The duration of one orbit is 90 minutes. During the daytime period of 45 minutes the Earth blocks the field of view, therefore the high voltage is switched off and no data is recorded. During nighttime continuous lightcurves and energy spectra are recorded. Figure 3.7 shows a schematic drawing of the HETE-II spacecraft with the positions of the three instruments. [39]

FREGATE

FREGATE is a set of wide-field gamma-ray spectrometers. It consists of four identical NaI scintillation detectors operating in an energy range of $6 - 400$ keV and providing a time resolution of $6.4\,\mu$s. The NaI crystals have a cylindrical shape, 10 mm thick with 71 mm diameter, which are read out by a photomultiplier. They have a deadtime of $10\,\mu$s.

[12] http://heasarc.nasa.gov/docs/heasarc/missions/wind.html

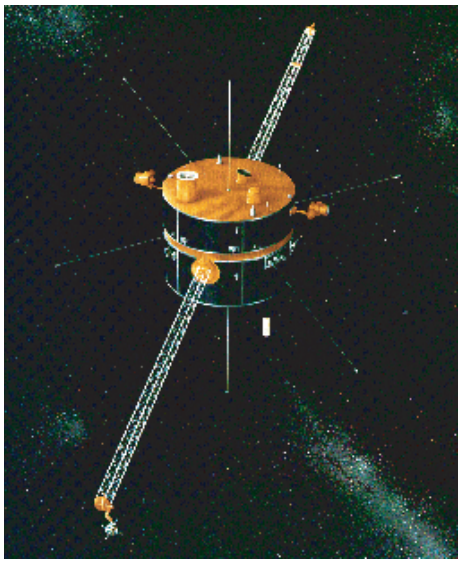

Figure 3.6: Illustration of the Wind spacecraft carrying the KONUS instrument consisting of two sensors mounted on long arms at each face of the spacecraft.[12]

Two radioactive ^{133}Ba sources aboard allow to monitor the gain of the detectors. A shield made of lead, tantalum, tin, copper and aluminum prevents photons from outside the field of view from reaching the NaI crystal. Its sensitivity in the range of 50 keV to 300 keV is $3 \cdot 10^{-7}\,\mathrm{erg\,cm^{-2}\,s^{-1}}$. FREGATE's field of view encloses 140°. It is built for triggering and spectroscopy in the hard X-ray and gamma-ray energy ranges and it alerts HETE-II's other instruments of the occurrence of a GRB. FREGATE has no localization capability. A schematic drawing of the FREGATE detector is shown in Figure 3.8.

WXM

WXM is a wide-field X-ray monitor consisting of two units, the X- and the Y-camera. Each consists of two identical position sensitive proportional counters (PSPC). The two detectors are oriented orthogonally to each other to measure X and Y direction independently. The X detector measures the projection angle of the burst direction in the XZ plane and the Y detector the projection angle in the YZ plane. The counter is divided in two layers. The upper layer consists of three anode cells equipped with 50 μm tungsten cathode wires placed at intervals of 3 mm. The gas filled counters (97% xenon and 3% carbon dioxide) are shielded by a 100 μm thick beryllium entrance window. The counters are covered with a coded mask made of 0.5 mm thick aluminum plates and 50.8 μm thick gold plates. The plates are interspersed with slits of randomly varying width of integer multiples of 2 mm. Measuring a set of two shift distances of the mask pattern in X and Y direction, allows the determination of the GRB location. The WXM is sensitive to X-rays in an energy range of 2 keV to 25 keV within a field of view of 85°. It reaches a localization accuracy of ~ 30 arcmin with a limiting sensitivity of $10^{-7}\,\mathrm{erg\,cm^{-2}\,s^{-1}}$. [39]

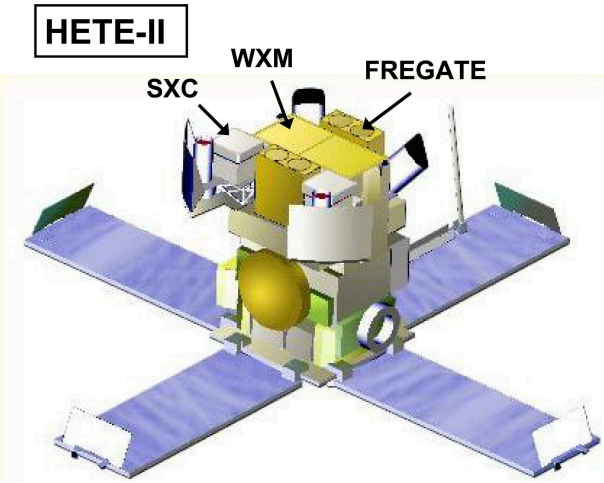

Figure 3.7: Schematic drawing of the HETE-II spacecraft. HETE-II carries three instruments: FREGATE, WXM and SXC.

SXC

A fraction of GRBs has a soft X-ray flux, which can be measured by the SXC, a set of soft X-ray cameras built to detect and localize GRBs. The detectors consist of $15 \times 15\,\mu\text{m}^2$ silicon pixels sensitive to photons within an energy range of $1 - 14\,\text{keV}$ and provide a position resolution of 30 arcsec for bright bursts. SXC's field of view encloses 65° half angle. The SXC is covered with a coded mask consisting of gold stretched over a stainless steel frame. The coding pattern of the mask was chosen to minimize noise for a given signal to noise ratio. To shield the detector from non X-ray photons, it is covered with an optical blocking filter made of $0.05\,\mu\text{m}$ thin aluminized plastic films and $25\,\mu\text{m}$ thin beryllium foil. SXC yields an excellent spectral resolution (full width at half maximum at 5.9 keV is $\sim 400\,\text{eV}$) and extends the spectral coverage of WXM down to 1 keV. [41]

3.2 Coordinate Systems

The GRB localization provided by satellites is usually given in equatorial coordinates except for localizations provided by KONUS, which is given in ecliptical coordinates.

3.2.1 The Equatorial Coordinate System

The position of each celestial object in the sky can be described by two parameters: the *right ascension* (RA or α) and the *declination* (DEC or δ). The declination is the polar angle measured in degrees from the equator ($\delta = 0°$) to the North Celestial Pole ($\delta = 90°$). The North Celestial Pole is defined by the direction of the Earth rotational axis. The right ascension is usually measured in hours ($24h = 360°$) from the vernal equinox, which is

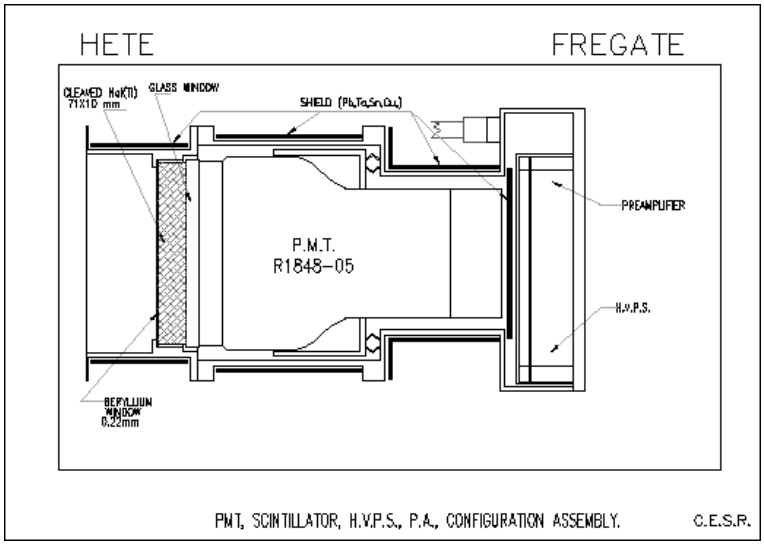

Figure 3.8: Schematic drawing of one of four FREGATE detectors: The NaI crystal has a cylindrical shape, 10 mm thick with 71 mm diameter (from [40]).

the intersection point of the ecliptical plane[13] with the celestial equator reached in spring. Due to precession and nutation of the Earth the position of the vernal equinox changes slowly but constantly and therefore the whole coordinate system varies slowly over time. Precession is a motion of the Earth rotation axis along a cone centered on the ecliptic pole. It is caused by a torque exerted on the spinning and distorted Earth by Sun and Moon. Nutation is caused by the same physical effect and overlays the precession with a higher frequency. The three effects taken account for in the coordinate transformation are displayed in figure 3.9. The varation of the coordinate system requires the specification of with reference to a particular epoch (e.g. J2000, the beginning of the year 2000 AD). [42]

3.2.2 The Ecliptical Coordinate System

The physical basis of the ecliptical coordinate system is the ecliptical plane, which is inclined 23.5° compared to the equatorial plane of the equatorial coordinate system. The ecliptic North Pole is located in the constellation of Draco and the ecliptic South Pole in the constellation of Dorado. The location of each object in the sky can be described by its ecliptical longitude and ecliptical latitude. The ecliptical longitude is measured eastwards from the vernal equinox and ranges from 0° to 360°. The ecliptical latitude ranges from −90° (South Pole) to 90° (North Pole). [43] Both, the ecliptical and equatorial coordinate system are sketched in Figure 3.10.

[13] plane of the Earth's orbit around the sun

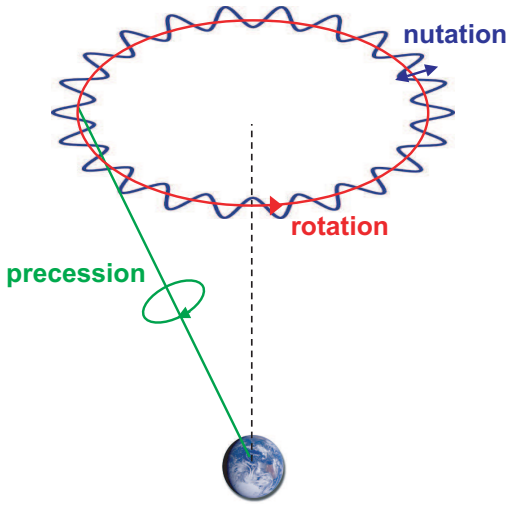

Figure 3.9: Rotation, precession and nutation have to be taken into account when transforming the coordinates from detector to equatorial coordinates.

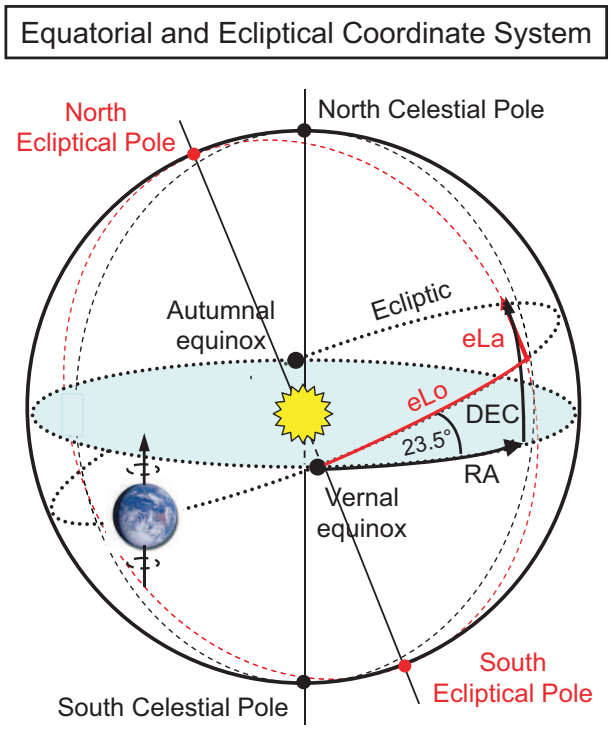

Figure 3.10: The equatorial and ecliptical coordinate systems: The equatorial coordinate system uses the right ascension RA and the declination DEC to describe an object in the sky. The right ascension is measured from the vernal equinox. The physical basis of the ecliptical coordinate system is the ecliptic plane, which is inclined 23.5° to the equatorial plane. An object is described by its ecliptical latitude eLa and ecliptical longitude eLo. The longitude is measured from the vernal equinox as well.

Chapter 4

Neutrino Detection

Neutrino detectors are classified into underground neutrino detectors and high-energy neutrino telescopes in transparent media like water or ice of oceans or lakes. The former achieve a low energy threshold whereas the latter have large detection volumes, which allow the detection of the low flux of high-energy neutrinos.
High energy neutrinos are used as a probe for the highest energy phenomena observed in the Universe. They yield information complementary to that obtained from observations of high energy photons and charged particles. Since protons and ions do not carry directional information because of their deflection by magnetic fields, neutrons decay before they reach the Earth and photons are absorbed by the interstellar medium and interact with radiation. Neutrinos interact only weakly and can reach the observer unobscured by intervening matter and undeflected by magnetic fields. The main purpose of high energy neutrino telescopes like AMANDA[1] is the search for the sources of highest energy phenomena. Possible candidates are, for instance, Active Galactic Nuclei (AGN), supernovae, super massive black holes and Gamma Ray Bursts (GRB). Apart from that, neutrino telescopes search for neutrinos produced in annihilation of Weakly Interacting Massive Particles (WIMPs). Their detection would be extremely important for cosmology since they would contribute to the cold dark matter content of the Universe. Furthermore, neutrino telescopes are used to monitor the sky for supernova explosions and to search for exotic particles like magnetic monopoles.
This analysis is based on data taken by the neutrino telescope AMANDA. The principle of operation and the design of AMANDA are described in this chapter.

4.1 The AMANDA Detector

4.1.1 Design

The AMANDA detector was designed, built, installed and is used for research by an international collaboration. The detector is located in the deep, optically transparent ice

[1] Antarctic Muon and Neutrino Detector Array

under the geographic South Pole. AMANDA was built from 1995-2000 and is operating since 1997. The AMANDA-B10 subdetector was running from 1997 to 1999 with 302 optical modules (OMs) on the now inner 10 AMANDA strings. Its extension AMANDA-II consists of 677 OMs containing photomultiplier tubes (PMTs) deployed on 19 strings arranged in a cylindrical shape with a diameter of 200 m embedded 1.5 to 2.0 km under the surface of the ice. The strings are not homogeneous because different techniques are tested. 4 strings supply high voltage and transmit the PMT pulses via coaxial electrical cables, while 6 strings use twisted pair electrical cables and 7 strings convert the electrical PMT pulse with a LED and transmit the optical pulse via an optical fiber. Two strings are IceCube prototypes with high voltage power supply inside the OMs themself and analog optical signal transmission used in the AMANDA DAQ.
The holes containing the strings were drilled with pressurized hot water, which refreezed in 35-40 hours fixing the strings in the ice. The components under the ice are kept as simple as possible to make the detector highly reliable. Each OM is connected with a cable to supply the high voltage and to transmit the anode signal whereas the data acquisition electronics are stored in a building at the surface. Advantage of the South Pole conditions is a low radiation noise rate. Since ice is a sterile medium the only noise is given by ^{40}K decays in the PMT glass housings and the PMT dark noise.
Air shower arrays at the surface were used to calibrate AMANDA by measurements of muons penetrating to AMANDA depth. [44]
Figure 4.1 illustrates the scales of AMANDA-II and the subdetector AMANDA-B10 and shows the design of one optical module. AMANDA will be part of the first 1 km^3 neutrino detector *IceCube*. The IceCube neutrino observatory at the South Pole is still under construction at the same site and will, once it is completed in 2010/11, consist of 4800 optical modules installed on 80 strings between the depth of 1450 and 2450 m in the antarctic ice. In addition 320 OMs will be deployed in 160 ice Čerenkov tanks referred to as *IceTop* on the ice surface directly above the strings to measure air showers for cosmic ray physics as a veto for IceCube.

4.1.2 Principle of Operation

AMANDA's main purpose is the detection of high-energy neutrinos from extrasolar sources and the determination of their arrival time, direction and energy. A high energy neutrino can interact in the polar ice in a charged current reaction ($W^{\pm}$ exchange) with a nucleon N:

$$\nu_l(\bar{\nu}_l) + N \rightarrow l^{\mp} + X, \tag{4.1}$$

where it creates a hadronic cascade X and a charged lepton l. According to the flavor of the incoming neutrino the lepton is an electron (e), a muon (μ) or a tau (τ). Each flavor has a different signature in the detector.
A high-energy ν_μ creates a muon, which is nearly collinear with the neutrino direction with an energy dependent mean deviation angle of

$$\psi = 0.7^\circ \cdot (E_\nu/\mathrm{TeV})^{-0.7}. \tag{4.2}$$

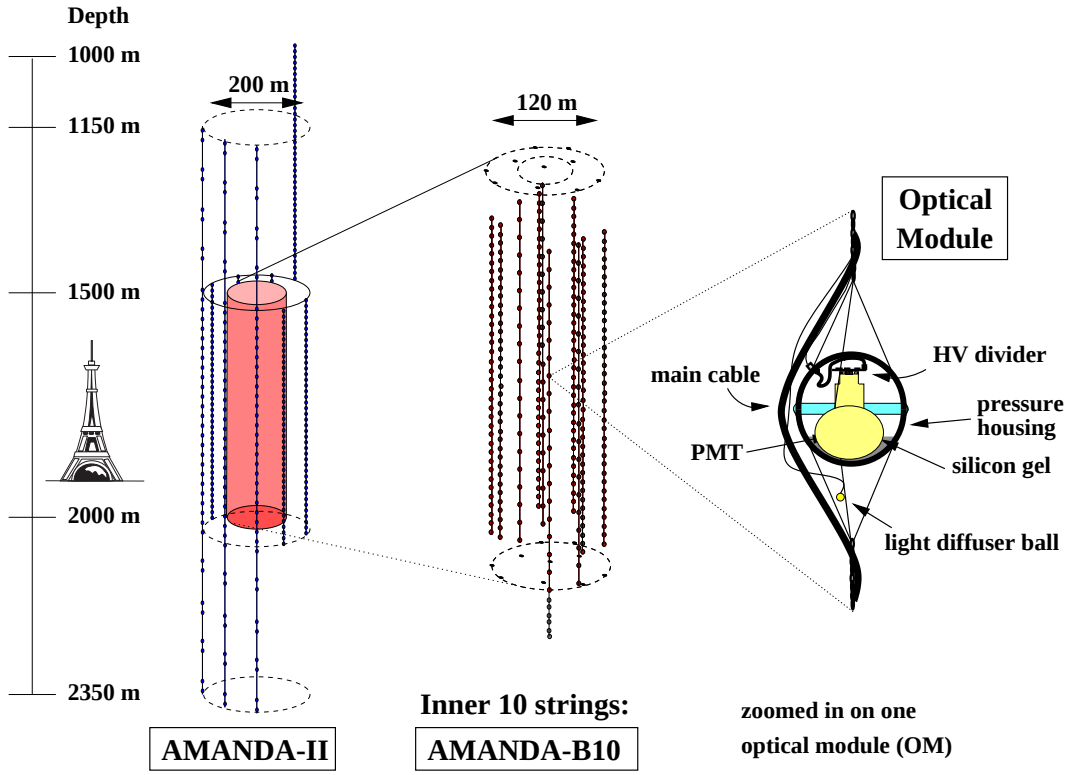

Figure 4.1: The scales of the subdetector AMANDA-B10 and its extension AMANDA-II are compared to the Eiffel tower. A schematic picture displays the design of one optical module. [45]

It carries a significant fraction $(60-80\%)$ of the neutrino energy. If the high-energy muon passes through the ice at a speed faster than the speed of light in this medium, it emits a cone of Čerenkov light. The refraction index in the ice $n = 1.32$ determines the cone opening angle θ_c by

$$\cos(\theta_c) = (n \cdot \beta)^{-1}. \tag{4.3}$$

For relativistic particles ($\beta \simeq 1$) this results in $\theta_c \approx 41°$. The direction of the muon and respectively the ν_μ direction is reconstructed from the time and amplitude information of the PMTs illuminated by the Čerenkov light. Depending on its energy the muon can travel tens of kilometers through the ice. For typical neutrino energies of $\sim 10^5$ GeV the muon path length is around $10-15$ km. Secondary charged particles are generated along the muon track in radiative energy loss processes. These particles produce Čerenkov light as well. The light intensity allows an estimation of the muon energy, which is a lower bound for the neutrino energy.

A high-energy ν_e creates an electron in a charged current interaction. The electron initiates an electromagnetic cascade in a small volume compared to the distance between neighboring OMs. The optical signature is an expanding spherical shell of Čerenkov light with a higher intensity in the forward direction. [45]

A tau produced in a ν_τ interaction generates a hadronic shower and flies several tens of

meters on a muon like tau track before decaying. The decay creates a second cascade. The signature of two extremely bright cascades is unique for high-energy ν_τ interactions and is called a *double bang event*. [46]
Neutral current interactions (Z^0 exchange) of high energy neutrinos with a nucleon N

$$\nu_l + N \rightarrow \nu_l + X \tag{4.4}$$

generate a hadronic cascade X. The neutral current interaction does not produce a detectable charged lepton. Figure 4.2 presents the different signatures in the detector. On the left a muon track creating a Čerenkov cone is shown. The cone angle θ_c is marked. The right hand side illustrates a cascade event with its characteristic nearly spherical Čerenkov front. Little circles mark the PMTs of the detector. Cascade-like events can

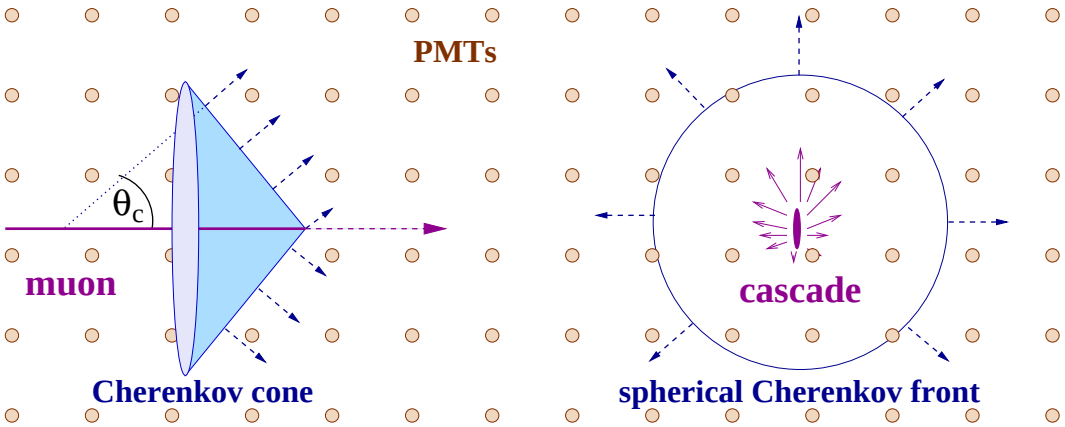

Figure 4.2: Left: Čerenkov Cone created by a neutrino induced muon. Right: Čerenkov Sphere produced by a cascade induced by a ν_e- or ν_τ-event or a neutral current event. [45]

only be measured within the detector volume whereas a muon track can be detected even if the ν_μ interaction vertex is far outside the detector. The long muon tracks allow an accurate direction measurement while the cascades give only poor directional information. But cascades also have clear advantages over muons. Since cascades are topologically distinct from AMANDA's primary background of down-going atmospheric muons (see section 4.2), it is not necessary to use the Earth as a filter, so cascade analyses have full sky coverage as opposed to the restriction to the Northern hemisphere for muon analyses. Furthermore, cascades have a significantly better energy resolution since the full energy is deposited in the detector. The cascade channel is sensitive to all neutrino flavors.
This analysis focusses on muon neutrinos since directional information is required. ν_e, ν_τ and neutral current interactions are of minor interest for this analysis.
The cross section for muon neutrino charged current interactions with a nucleon is calculated by Gandhi et al. (for a detailed calculation see [47]).

$$\frac{d^2\sigma}{dxdy} = \frac{2G_F^2 M E_\nu}{\pi}\left(\frac{M_W^2}{Q^2+M_W^2}\right)^2 [xq(x,Q^2) + x\bar{q}(x,Q^2)(1-y^2)^2], \tag{4.5}$$

where $x = Q^2/2M\nu$ and $y = \nu/E_\nu$ are the Bjorken scaling variables and $-Q^2$ the invariant momentum transfer between incoming neutrino and outgoing muon, $\nu = E_\nu - E_\mu$ is the energy loss in the laboratory frame, M is the nucleon mass and M_W the W-boson mass. G_F is the Fermi constant. The quark distribution functions are given by

$$q(x,Q^2) = \frac{u_v(x,Q^2)+d_v(x,Q^2)}{2} + \frac{u_s(x,Q^2)+d_s(x,Q^2)}{2} + s_s(x,Q^2) + b_s(x,Q^2) \tag{4.6}$$

$$\bar{q}(x,Q^2) = \frac{u_s(x,Q^2)+d_s(x,Q^2)}{2} + c_s(x,Q^2) + t_s(x,Q^2)\ , \tag{4.7}$$

where subscripts v and s stand for valence and sea contributions and u, d, c, s, t, b label the distributions for different quark flavors in a proton.

4.1.3 The AMANDA Coordinate System

AMANDA is located at the geographic South Pole. Muon directions are described in spherical coordinates, e.g. the two angles θ and ϕ. The azimuth angle ϕ ranges from 0° to 360° and corresponds to degree of longitude + 180°. The zenith angle θ is measured with respect to the rotation axis of the Earth. It ranges from 0° to 180°. The South Pole location is defined as $\theta = 0°$ and the North Pole as $\theta = 180°$. θ corresponds to degree of latitude - 90°. Incoming particles from North to South are referred to as up-going particles. Down-going particles move from South to North. Figure 4.3 illustrates the AMANDA coordinate system.

4.2 Background

The presented analysis focusses on muon neutrinos. Most events triggered by AMANDA are atmospheric muons reaching the detector from above. At the depth of AMANDA the down-going cosmic ray muon flux is about 5 orders of magnitude larger than the expected neutrino flux. [48]
Muons produced in charged current interactions of ν_μ (see section 4.1.2) can be separated from atmospheric ones by taking into account directional and energy information. The Earth serves as a shield against particles, such that up-going muons must be ν_μ induced. At the energy range of interest for this analysis, $10^4 - 10^8$ GeV, downgoing muons can be rejected by a zenith angle selection and up-going muons can be used as reliable neutrino messengers. Directional information is obtained by reconstruction and therefore accompanied by an uncertainty. Possible scenarios causing a misreconstruction are classified below. [45]

- **Nearly horizontal muons**: Due to the finite angular resolution even a small error in the reconstruction can cause a down-going event with a true incident angle close to the horizon to appear as an up-going event.

- **Muon bundles**: If multiple muons originating in a single air shower have a small spatial separation they are reconstructed as a single bright muon track.

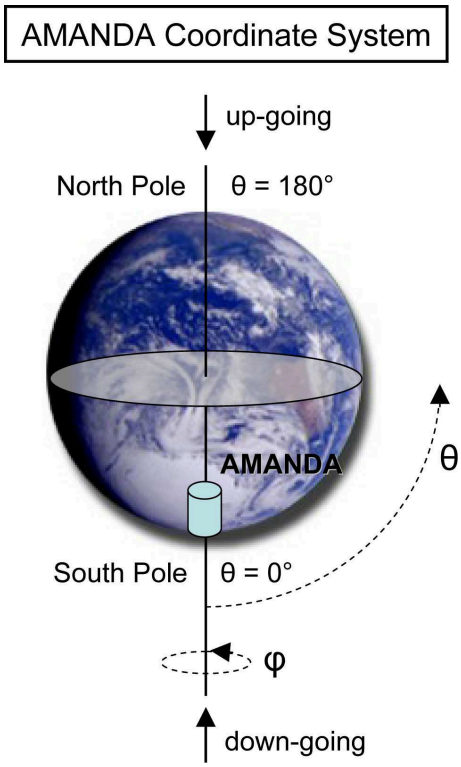

Figure 4.3: The AMANDA coordinate system. AMANDA is located at the South Pole. The zenith angle θ is measured with respect to the rotation axis of the Earth. The South Pole location is defined as $\theta = 0°$ and the North Pole as $\theta = 180°$. Incoming particles from North to South are referred to as up-going particles. Down-going particles move from South to North.

- **Cascades**: Additional light produced in bright stochastic energy loss distorts the Čerenkov cone emitted by the muon.
- **Stopping muons**: Muons lose their energy and stop eventually within or close to the detector. Especially muons which stop just before entering the detector from the side can mimic an up-going hit pattern.
- **Scattering layers**: Light from bright events scattered at dust layers from bright events can mimic an up-going hit pattern.
- **Corner clippers**: Čerenkov light emitted by muons passing diagonally below the detector traverses the detector in upwards direction and mimics an up-going muon.
- **Uncorrelated coincident muons**: The combination of two coincident muons, one traversing the bottom of the detector and a later one traversing the top, can be reconstructed as one up-going muon.
- **Electronic artifacts**: Noise and cross-talk can occasionally produce hits, which distort the time pattern and lead to a misreconstruction.

4.3 Simulation of Neutrino Signal Events

The simulation is divided into several steps:

- Simulation of neutrino interactions
- Muon propagation
- Čerenkov photon propagation
- AMANDA-II detector simulation

A brief summary of these four steps is given in the following sections. For a more detailed description see [49].

4.3.1 Simulation of Neutrino Interactions

The program NUSIM [50] simulates charged current interactions of muon neutrinos in an interaction region, which is two times the range R of a muon with given energy E_ν from the detector center. The range depends on the energy loss, which is well approximated by a linear function of the energy:

$$\frac{1}{\rho} \cdot \frac{dE}{dx} = -a - b \cdot E, \tag{4.8}$$

where the constant $a = 2.68\,\mathrm{MeV\,g^{-1}\,cm^2}$ takes into account energy loss by ionization and the linear term ($b = 4.7 \cdot 10^{-6}\,\mathrm{g^{-1}\,cm^2}$) includes fractional energy loss from other contributions as bremsstrahlung, photo-nuclear interactions and pair-production. ρ is the density of the medium. Integration yields the range R after which the muon has lost all of its energy:

$$R = \frac{1}{\rho} \cdot \frac{1}{b} \cdot \ln(1 + \frac{b}{a} \cdot E)\ . \tag{4.9}$$

Actual interaction probabilities for the simulated events are given by the cross section (see equation 4.5) and are assigned as weights. The scattering angle between neutrino and muon is neglected. According to equation 4.2 the scattering angle becomes very small for the energies of interest: for $E_\nu = 10^5\,\mathrm{GeV}$ it yields $\psi = 0.03°$. The input energy spectrum is chosen to follow $\frac{d\Phi}{dE} \propto E^{-1}$ in order to obtain equal statistics in each logarithmic energy bin.

4.3.2 Muon Propagation

A muon generated in charged current neutrino interactions by NUSIM needs to be propagated from the interaction region through rock, ice and the detector volume. On its way it loses energy in discrete events of stochastic nature. The probability that those events take place increases with a decreasing energy lost per event. Below an energy loss

Table 4.1: The simplified propagation material model used in MMC consists of four layers with constant density.

Material	Horizontal Depth [m]	Density [$\mathrm{g\,cm^{-3}}$]
Air	< 0	$0.81 \cdot 10^{-3}$
Snow	$0 - 200$	0.76
Ice	$200 - 2810$	0.92
Rock	> 2810	2.65

threshold ($\Delta E < 0.5\,\mathrm{GeV}$) an energy loss event is treated as a continuous process by the propagation program MMC [51], only secondaries with $E > 0.5\,\mathrm{GeV}$ are propagated as individual particles. The propagation material is described in a simplified model of four horizontal layers of constant density. The layers and their density is summarized in table 4.1.

4.3.3 Photon Propagation

The Čerenkov photons emitted by neutrino induced muons and their secondaries are propagated through the ice with the PTD software package [52]. Direction and arrival time of Čerenkov photons are influenced by scattering and absorption in the medium. Scattering is mainly caused by dust, organic matter, air bubbles and clathrate. At 400 nm the effective scattering length is on average 20 m, while the absorption length is typically 110 m with a strong wavelength dependence. [45] The Muon Absorption Model (MAM) describes the ice properties in a strongly simplified way. The ice properties at each OM are different, but instead of treating each OM separately they are divided into four classes according to their horizontal depth for reasons of simplification. The scattering and absorption coefficients of each class are fitted and the resulting effective ice properties are used for each class. This effective optical properties are considered constant for each class and the OMs are assumed to be surrounded by an infinite layer of ice with these properties.
Photon simulations[2] are used to determine the expected number of photo electrons dN in the time interval $[t, t + dt]$ at any space point (x, y, z) detected with an optical module pointing to a direction (θ, ϕ) relative to the track direction. The expected number of photo electrons is calculated on a grid of values in the parameter space and stored in tables. For a generated position of a muon track the number of photo electrons detected in an OM and their arrival time can be directly called from the data archive. Integrating the number of photo electrons over time yields the mean amplitude expected in an OM.

[2]For reasons of simplification only photons with an average wavelength of 420 nm were simulated instead of generating a full Čerenkov spectrum.

4.3.4 AMANDA-II Detector Simulation

The program AMASIM [53] simulates the response of the AMANDA detector to Čerenkov photons produced by muons or cascades. Input parameters of the existing hardware are used. Simulations of several parts of the AMANDA DAQ are included in AMASIM. These are the optical modules, the cables, the SWAMP[3], the discriminators, the TDCs[4], the ADCs[5] and the trigger logic. [53]

4.4 AMANDA Data - Reconstruction and Filtering

Simulated neutrino signals as well as experimental data are processed at DESY-Zeuthen. They are processed in several steps, so called processing levels (see table 4.3), and multiple reconstructions are applied. Different levels differ in the applied reconstructions and cleaning cuts. The cuts reduce the number of events and thus allow more time consuming reconstructions at higher cut levels in reasonable computing time. The cleaning cuts reject down-going muons which are considered as background in muon neutrino analyses. The data sample is processed to be of common use for many muon neutrino analyses. Different analyses have different requirements to their data and therefore data at different processing steps are kept. For the presented analysis data processed to Level 3 is used. All processing steps and fits are done with *Sieglinde*[6] except the *paraboloid fit* and the final *munt*[7] step.

4.4.1 Trigger and Hit Cleaning

The main trigger (Multiplicity Trigger) is activated whenever pulses from 24 OMs are recorded within a 2500 ns time window. A hit and OM cleaning is performed to remove "fake" hits from the record to avoid a bias in the reconstruction. Each year a different set of bad OMs was established. Bad OMs are characterized by a too low recorded hit rate or the production of a high level of noise or jumping between both states. A trustworthy OM shows reasonably dark noise rates, ADC and TDC rates. Additional OMs have been considered bad because they lie outside of the detector bulk and either no reliable calibration exists or they are located in ice layers full of bubbles. The number of bad OMs changed from year to year. Table 4.2 specifies the numbers of bad OMs during the years 2000 - 2004. The decrease in the number of bad OMs over the years 2000 - 2003 is due to identification and elimination of detector problems during the austral summers. 2000 is divided in three periods and therefore three different numbers are quoted for this year. The time over threshold (ToT) cleaning removes electronic noise induced by other

[3] SWedish AMPlifier
[4] time to digital converter
[5] analog to digital converter
[6] http://www-zeuthen.desy.de/nuastro/sieglinde/sieglinde.html
[7] *munt* converts f2k files to hbook files and is part of the *Siegmund* software package available at http://www-zeuthen.desy.de/nuastro/software/siegmund/siegmund_old/pro/siegmund.html

Table 4.2: Number of bad OMs per year. These OMs are not used for reconstruction.

Year	number of bad OMs
2000	186 / 196 / 209
2001	165
2002	144
2003	138
2004	143

pulses in neighboring cable pairs (referred to as cross-talk) or generated in the amplifiers. The ToT is the time difference between recorded leading and trailing edge of the PMT pulses. Noise peaks at small ToT while real pulses peak at 200 ns. To remove this noise a selection cut is applied individually for each year and each OM with electrical read-out. Only hits with ToTs above the cut value are kept. ToTs from those OMs with an optical readout are required to be larger than 5 ns.
An additional cross talk cleaning using the non-linear correlation between amplitude (ADC) and threshold (ToT) is applied to remove these hits that have not been excluded by the ToT cleaning.
Dark noise is caused in the PMTs by thermal emission of photoelectrons or radioactive decay in the OM. These are stochastic signals that can only be separated by temporal properties and spatial isolation. Parts of the dark noise can be removed by time window cleaning, that excludes hits with pulses outside the time interval [-22 μs, 10 μs] around the trigger time. The time window is determined by the time that a particle needs to traverse the detector. Isolated hits are excluded when there is no other hit within 500 ns of time or in any channel closer than 100 m to the module.

4.4.2 Track Reconstruction

The hits remaining after the hit cleaning are used to reconstruct muon tracks. A first guess is generated by a simple and fast pattern recognition algorithm. Seeded on this first estimate a maximum likelihood reconstruction is applied. First guess algorithms are fast and coarse reconstructions that provide the identification of a large part of the muon background. To save CPU time first guess reconstructions are applied first to reduce the number of events running through the full reconstruction. The reconstructions used in this analysis are briefly described here.

First Guess Methods

The **Direct Walk First Guess** is a pattern recognition based algorithm that first selects track elements given by straight lines between any two hit OMs. These track elements have to pass quality criteria (for more details see [45]). A cluster search is applied to the remaining track elements and the cluster containing the largest number of track elements is selected. The average direction of all tracks contained in the selected cluster defines the first guess hypothesis for the reconstructed muon track.
JAMS (Just Another Muon Search) is a pattern recognition based on first guess algorithm as well. It searches hit clusters along a regular grid of input directions, reconstructs the track parameters for the found clusters, assesses the quality of the fit and sorts the reconstructed tracks according to their quality[8].

Likelihood Methods

The track reconstruction gives an estimate of a set of track parameters $\{\mathbf{a}\}$ given a set of experimentally measured values $\{\mathbf{x}\}$. Assuming that the single components x_i of $\{\mathbf{x}\}$ are independent the corresponding likelihood reduces to

$$\mathcal{L}(\mathbf{x}|\mathbf{a}) = \prod_i p(x_i|\mathbf{a}). \tag{4.10}$$

$p(x_i|\mathbf{a})$ is the probability density function of observing the measured value x_i for a given set of track parameters $\{\mathbf{a}\}$. The x_i measured by AMANDA are the hit times t_i, the time over threshold ToT_i for each PMT and the peak amplitude A_i. The hit times are considered most relevant.
For simplification the muon track is assumed infinitely long and ultrarelativistic with $\beta = 1$. In this case the generated Čerenkov cone has a fixed angle of $\theta_c \approx 41^\circ$ (see equation 4.3) and the track can be described by the following parameters:

$$\{\mathbf{a}\} = (\mathbf{r}_0, t_0, \hat{\mathbf{p}}, E_0). \tag{4.11}$$

$\mathbf{r}_0$ is an arbitrary point on the track, which the muon passes at time t_0 with an energy E_0 along the direction $\hat{\mathbf{p}}$. The reconstruction is performed by minimizing $(-\ln(\mathcal{L}))$ with respect to $\{\mathbf{a}\}$. The minimization is repeated n times in an *n-fold iterative likelihood* fit in order to avoid wrong results from local minima. The algorithm is restarted with random track hypotheses to cover larger regions of the parameter space.
This leads to an improvement in the angular resolution. For example the first guess JAMS reconstruction yields an angular resolution of 4.4° compared to $1.5^\circ - 2.5^\circ$ for the 32-fold iterative time likelihood fit seeded on the JAMS first guess.
The **Pandel Reconstruction** is based the *Pandel function* [54]

$$P(r, t_{\mathrm{res}}) = \frac{1}{\Gamma\left(\frac{r}{\lambda}\right)} \cdot \frac{1}{t_{\mathrm{res}}} \cdot \left(\frac{t_{\mathrm{res}}}{\tau}\right)^{\frac{r}{\lambda}} \cdot \exp\left(-\frac{t_{\mathrm{res}}}{\tau} - \frac{r + c_{\mathrm{ice}} t_{\mathrm{res}}}{\lambda_a}\right) \tag{4.12}$$

[8] http://icecube.wisc.edu/internal/amanda-archive/software/sieglinde/usermanual/mod_ref_JAMS.html

to describe the arrival time residual distribution $p(t_{\text{res}})$, with $t_{\text{res}} = t_{\text{hit}} - t_{\text{exp}}$. t_{exp} is the predicted hit time by the track geometry and t_{hit} the measured hit time. r gives the distance from the track, $\lambda_a = 98\,\text{m}$ the absorption length and c_{ice} the speed of light in ice. λ and τ are free parameter fixed by a fit to simulated photon arrival times. The fit obtained $\lambda = 33\,\text{m}$ and $\tau = 557\,\text{ns}$. The Pandel function describes the delay in the photon arrival due to scattering and absorption. Assuming homogeneous ice with constant absorption and scattering length individual hit probabilities can be calculated analytically and allow the calculation of the time likelihood.[45]
In the **paraboloid fit** -ln($\mathcal{L}$) is minimized by fitting a paraboloid to it. $\mathcal{L}_i(\theta_i, \phi_i)$, with muon track directions (θ_i,ϕ_i), is a scalar field around the maximum likelihood value evaluated in a Pandel likelihood reconstruction. A least square fit is performed for $(a_0, b_0, b_1, c_{11}, c_{12}, c_{21}, c_{22})$ to determine the shape of a paraboloid:

$$f(\theta, \phi) = a_0 + (b_0, b_1)^T(\theta, \phi) + (\theta, \phi)^T \begin{pmatrix} c_{11} & c_{12} \\ c_{21} & c_{22} \end{pmatrix} (\theta, \phi) \ , \tag{4.13}$$

which minimizes $\sum_i (f(\theta_i, \phi_i) \ln(\mathcal{L}_i(\theta_i, \phi_i)))^2$.
In this analysis the Pandel first guess reconstruction, the 32-fold Pandel Likelihood fit seeded on JAMS and the Paraboloid fit have been used.

4.4.3 Upgoing Muon Filtering

Table 4.3 gives an overview of the processing steps and the applied quality cuts. The cuts clean the data from down-going muons, which have mainly atmospheric origin. Each quality cut reduces the number of events. The number of events left in the AMANDA data at different cleaning levels for the years 2000 - 2004 are presented in table 4.4. The simulated signal has to pass the same quality cuts. The signal passing rates for energy spectra following E^{-1} and E^{-2} respectively are summarized in table 4.5 adopted from [49]. Harder spectra have lower passing rates. High energy events produce more light and are therefore able to trigger the detector even if they pass outside the detector. All photons experience multiple scattering and thus a reliable direction reconstruction is not possible any more. Comparing table 4.4 and table 4.5 shows that the quality cuts reject a large fraction of the background events while they keep most of the signal events.

4.4.4 Track Quality Parameters

Parameters that characterize the track quality enable a separation between background and signal events. Misreconstructed downgoing events that appear up-going are expected to show worse track quality. In this analysis three parameters (smoothness, angular resolution and the maximum likelihood) are used to investigate the track quality.

[9] http://www-zeuthen.desy.de/nuastro/protected/point/combined00-03/combined00-03.html

Table 4.3: Reconstructions and Quality Cut Levels in AMANDA Data Processing done at DESY-Zeuthen [9]

Reconstruction	**Applied Cut**
Level 1	Zenith (direct walk) > 70
Direct Walk Reconstruction (first guess)	
Pandel Likelihood Reconstruction (4-fold)	
JAMS Reconstruction (first guess)	
Level 2	Zenith (JAMS) > 80
OM and Crosstalk cleaning	
Pandel Likelihood Fit (32-fold, JAMS seed)	
Smoothness calculation	
Level 3	Zenith (Pandel) > 80
Paraboloid Fit (Siegmund) on Pandel track	

Table 4.4: Number of events in AMANDA data, processed at DESY in Zeuthen, at different cleaning levels

Processing Level	**2000**	**2001**	**2002**	**2003**	**2004**
Raw	$1.37 \cdot 10^9$	$2.00 \cdot 10^9$	$1.91 \cdot 10^9$	$1.86 \cdot 10^9$	$1.72 \cdot 10^9$
L1	$45.4 \cdot 10^6$	$81.8 \cdot 10^6$	$68.3 \cdot 10^6$	$65.3 \cdot 10^6$	$60.8 \cdot 10^6$
L2	$5.50 \cdot 10^6$	$6.87 \cdot 10^6$	$7.59 \cdot 10^6$	$8.02 \cdot 10^6$	$7.47 \cdot 10^6$
L3	$1.63 \cdot 10^6$	$1.90 \cdot 10^6$	$2.10 \cdot 10^6$	$2.22 \cdot 10^6$	$2.09 \cdot 10^6$

Table 4.5: Signal passing rates at different cleaning levels for an E^{-1}, an E^{-2} and an E^{-3} spectrum

Processing Level	E^{-1}	E^{-2}	E^{-3}
L1	0.78	0.91	0.95
L2	0.59	0.82	0.90
L3	0.57	0.80	0.88

Smoothness

Different definitions of the smoothness variable exist [55]. The P_{hit} smoothness used in this analysis takes into account the granularity and actual geometry of the detector. This smoothness S describes the cumulative distribution of the hits along the muon track. $N(l)$ is the number of direct hits[10] within a radius of 50 m from the reconstructed track:

$$N(l) = \sum_{i}^{\text{direct hits}} \Theta(l - l_i) \ , \tag{4.14}$$

where l is the projection of the hit position onto the track. The Heaviside function $\Theta(x)$ makes sure that only hits with $l_i < l$ are considered in the calculation. The projection is illustrated in figure 5.23. The number of expected hits at the position l from the origin can be calculated by taking into account the probability $P(\rho_j)$ that the OM j with distance ρ from the track records a direct hit within the 50 m radius:

$$N_{\text{exp}}(l) = \sum_{j}^{\text{OMs}} P(\rho_j)\Theta(l - l_j) \ . \tag{4.15}$$

For an infinitely long track the number of expected hits becomes $N(\infty)$.
The smoothness is defined as the normalized maximum deviation of the number of hits $N(l)$ recorded from the origin of the track to a position l from the number of expected hits $N_{\text{exp}}(l)$:

$$S = \frac{\text{sgn}(N(l_{\text{max}}) - N_{\text{exp}}(l_{\text{max}}))}{N(\infty)} \max_{l} |N(l) - N_{\text{exp}}(l)| \ . \tag{4.16}$$

Here l_{max} is the projection length l that maximizes $|N(l) - N_{\text{exp}}(l)|$.
A smoothness close to 1 indicates that hits are found in OMs where none would be expected while a smoothness close to -1 states that hits are missing in OMs where hits are expected. Both cases indicate a possible misreconstruction.

Angular Resolution

The angular resolution describes the error in the reconstructed direction. The uncertainty in the reconstructed direction can be estimated from the shape and size of the negative likelihood valley. The paraboloid fit minimizes -ln($\mathcal{L}$) by fitting a paraboloid $f(\theta, \phi)$ to it. The paraboloid is given by equation 4.13. Equipotential lines for a paraboloid are ellipses. The region where the logarithm of the likelihood is larger than half of its maximum value is approximated by the ellipse

$$f(\theta, \phi) = \frac{1}{2} f_{max}(\theta, \phi) \ . \tag{4.17}$$

[10] hits in an interval [-25 ns, 75 ns] relative to the expected arrival time at the OM

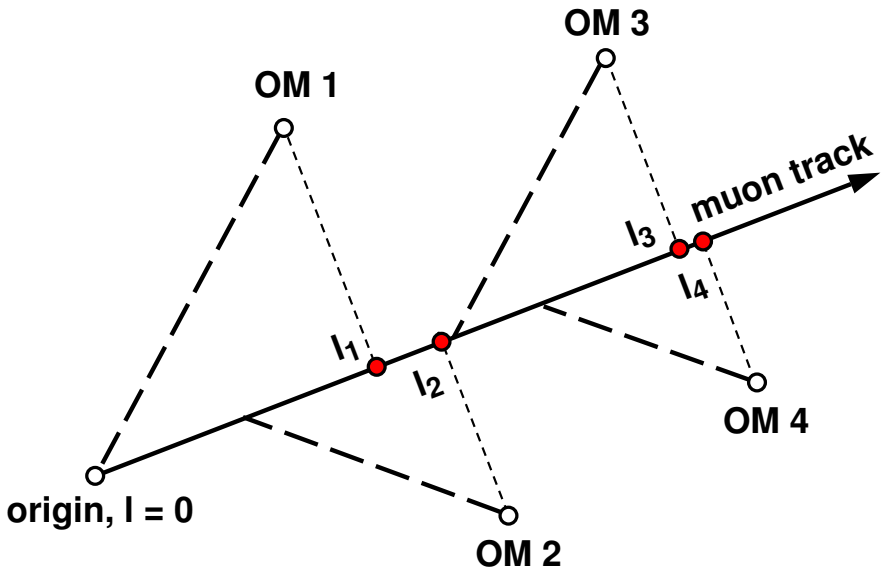

Figure 4.4: Illustration of the projection of the OM hits onto the reconstructed muon track.

This region is considered as the event specific uncertainty in the direction reconstruction. The angular resolution R is defined as the square root of the error ellipse area described by the two axes σ_1 and σ_2:

$$R = \sqrt{\sigma_1 \sigma_2} \; . \tag{4.18}$$

Misreconstructed events are expected to have a large angular resolution.

Maximum Likelihood

The maximum likelihood evaluated in a likelihood reconstruction naturally indicates the quality of the reconstruction. The negative logarithm of the likelihood given by equation 4.10 is expected to be large for misreconstruced events.

Chapter 5

Analysis of Poorly Localized GRBs in 2000-2004

Former analyses focussed on well localized GRBs. These bursts are detected by a direction sensitive satellite or by at least three non-direction sensitive instruments, which allows the determination of the burst direction within a small error circle. Swift and BATSE are the main providers of well GRB localizations since their detectors are direction sensitive. In contrast poor localization information, e.g. restriction to a narrow annulus or a banana shaped segment in the sky, can be obtained if a GRB triggered two non-direction sensitive satellites or one non-direction sensitive satellite and the KONUS instrument. Former analyses neglected this group of poorly localized GRBs, which presents an important subsample of all detected GRBs, especially after the switch-off of BATSE in May 2000 before the launch of Swift in November 2004.

5.1 Selection of Poorly Localized Bursts

The poorly localized bursts analyzed here are a subsample of the IPN bursts. Well localized BATSE and IPN bursts have been analyzed by K. Kuehn and R. Hardtke [56] and therefore are **not** included in this analysis. Bursts which are detected by two non-direction sensitive IPN satellites are localized via the triangulation method (see chapter 3) to a narrow annulus with typical widths $< 1°$. Detection by the KONUS instrument allows the localization within a typically $20°$ wide annulus. The probability of finding the GRB within the annulus is described by a Gaussian with mean at the annulus center line r_{center}. The half width of the annulus corresponds to 3σ of the Gaussian[1]. The coordinates defining the annulus are summarized in the IPN catalog, these are the right ascension α_a and declination δ_a of the center point, its central radius r_{center} and its half width. The probability distribution within the annulus is illustrated in Figure 5.1.

[1] private communication with Kevin Hurley, physics coordinator of the IPN

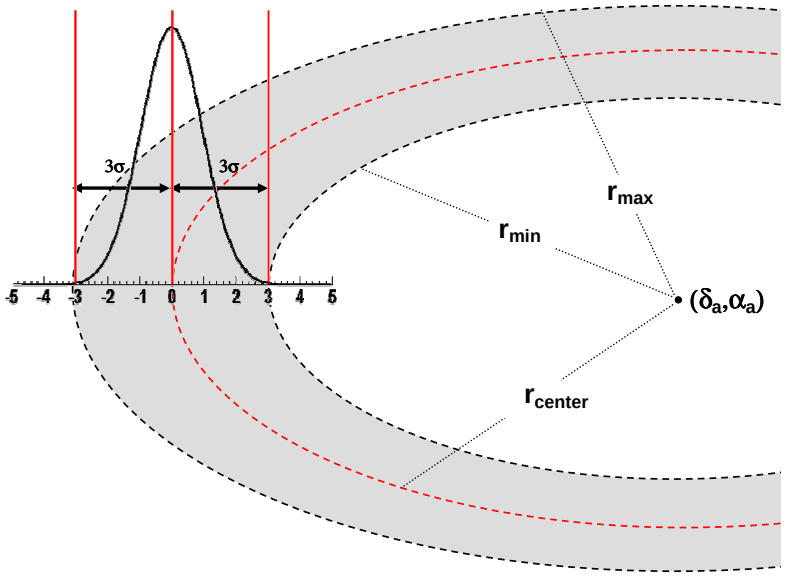

Figure 5.1: Bursts are localized within an annulus by the triangulation method. The probability of finding the GRB within the annulus is described by a Gaussian with mean at the burst center line r_{center}. The half width of the annulus corresponds to 3σ of the Gaussian. The inner and outer radius are called r_{min} and r_{max}. The center of the annulus is denoted with two coordinates: right ascension α_a and declination δ_a.

Two classes of poorly localized bursts are analyzed:

- Bursts that are detected by two non-direction sensitive IPN satellites and therefore are localized to a narrow annulus with a typical width of 1°.
- Bursts that trigger one non-direction sensitive IPN satellite and in addition the KONUS instrument located on the WIND spacecraft. Two identical gamma detectors are mounted on the WIND spacecraft separated from each other as far as possible. The triangulation method can be applied treating the two detectors like two satellites. In this case the method yields a localization within a 20° wide annulus. The narrow IPN annulus intersects with this wider KONUS annulus.

Both cases are illustrated in figure 5.2. The first case is rare compared to the latter one. GRBs which are only localized to a narrow IPN annulus are often not suitable for a muon neutrino analysis with AMANDA since the annuli usually lie in both, the southern and northern hemisphere. The 3σ wide localization band or the intersection region of the two bands, if KONUS was involved in the detection, is inspected for each burst. Localization bands or intersection regions which extend to the southern hemisphere cause the exclusion of the burst from the analysis. 80 bursts from the IPN catalog fulfill the described selection criteria. These bursts are summarized in appendix A in tables A.1 - A.5. There, the bursts are characterized by their start time and duration. For satellites that are not on low Earth orbits like KONUS this start time is not identical with the Earth crossing time. In case of poor localizations, the Earth crossing time can only be

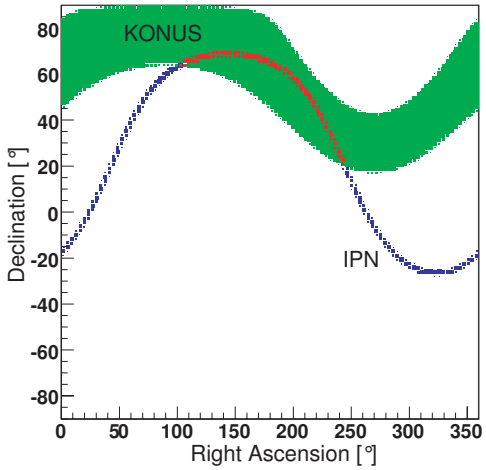

(a) A burst detected by one non-direction sensitive IPN satellite and in addition by the KONUS instrument: The narrow IPN annulus intersects with the wider KONUS annulus. The intersection region (marked red) has a banana shape.

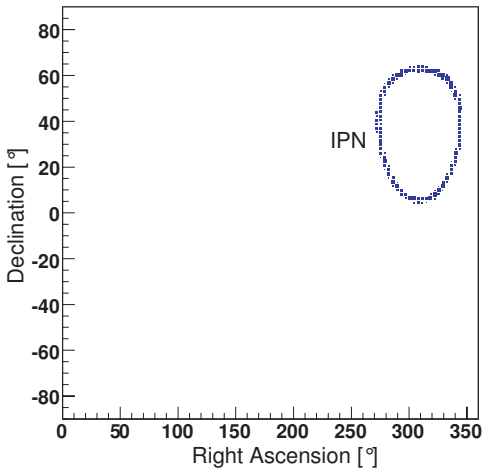

(b) A burst detected by two non-direction sensitive IPN satellites: It is localized to a narrow annulus with a typical width (6σ) of 1°.

Figure 5.2: The two classes of poorly localized bursts used in this analysis.

constrained to a few seconds. The definition of the search time window (see section 5.4.1) accounts for this uncertainty in the Earth crossing time correction. The duration[2] quoted in the appendix A represents the time during which the burst emits clearly detectable gamma-ray emission. This duration is used instead of the T_{90} variable, which is not meaningful when different detectors observe the same event (see section 3.1).

5.2 Detector Stability

Before the GRB neutrino search is performed on the experimental AMANDA data, the stability of the detector has to be tested. In a stable detector the background events are expected to be temporally uncorrelated and to not show any non statistical fluctuations. An instability in the detector could create a fake neutrino signal and might lead to a wrong discovery, which is clearly undesirable. Therefore, GRBs observed during unstable periods of AMANDA are rejected.
To keep the analysis blind, the data in a time window of 10 minutes surrounding the burst start time T_0 is excluded from the stability tests. Blindness is necessary to ensure that the process of selecting and optimizing cuts is not biased. The stability of the experimental data is tested within a two hour background window, one hour immediately before the

[2]Provided by Kevin Hurley in private communication.

blind window and one hour immediately after the blind window. All tests are performed on Level 3 data, because this cut level is used for the actual analysis. Only this off-time window is looked at during the stability tests while the 10 minute on-time window stays blind. Figure 5.3 displays the choice of the on- and off-time window. Two problems can

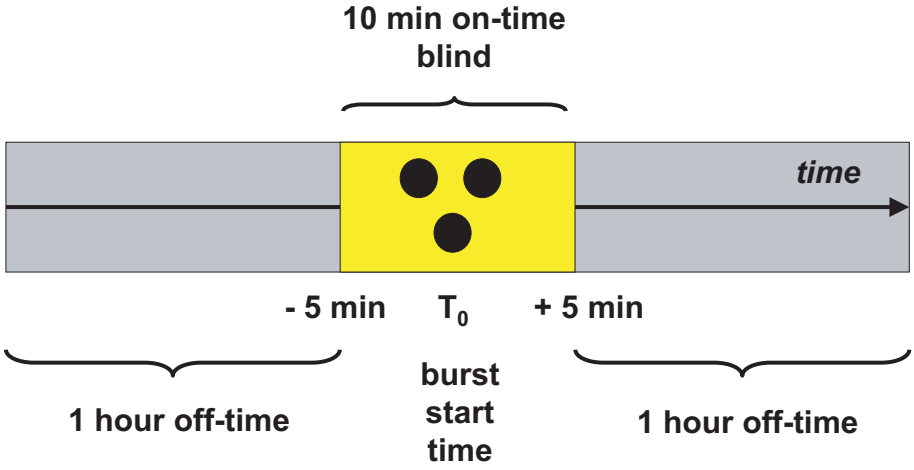

Figure 5.3: On- and Off-time window: A 10 minute interval centered on the GRB start time T_0 is kept blind during stability tests on the experimental data. The test is performed on a two hour background window, one hour before and one hour after the blind window.

occur and are discussed here:

- Instabilities in the off-time window do not necessarily imply an instability in the on-time window, where finally the neutrino signal search will be performed. However, to fulfill the blindness criteria we are not allowed to investigate the on-time window. Therefore, we are forced to conclude the characteristics of the on-time window from the behavior of the off-time window. We believe that requiring the stability of the off-time window yields a reliable criterion to ensure that our measurement is trustworthy.

- Instabilities could occur only in the on-time window without affecting the off-time data. Such an scenario is very unlikely and instabilities most probably occur over a longer period of time.

The data contained in the off-time window of some bursts was taken in runs that appear on the *lists of bad files*. These lists are compiled during data processing for each year separately. Dead OMs defined by a low noise rate and noisy OMs defined by a high noise rate during most of the year appear on a common list of bad OMs and are removed. This OM cleaning does not account for noisy behavior of neighboring OMs induced by the bad OM and lasting for a limited time period. An additional condition was introduced to exclude such time periods: If the time dependent number N_{crit} of OMs with bad status (additional to the OMs from the bad file list) exceeds 50, the file is rejected (for more details see [57]). The rejection of unstable periods is important to enable the comparability

of simulated and experimental data, since it is not possible to simulate such instabilities. Bad runs are excluded in further processing steps. 8 bursts were rejected for this reason:

- GRB010212
- GRB010213
- GRB020529
- GRB020715
- GRB020725
- GRB030629
- GRB040404
- GRB040615

Two different tests are applied to the remaining bursts to identify both, instabilities on short time scales randomly distributed in time, and instabilities over an expanded time interval. We define a burst as stable if the data contained in its off-time window passes the defined stability tests. An unstable burst fails to pass at least one of the tests.

5.2.1 The Cumulative Test

Assuming a stable detector the recorded background event rate is expected to be constant except for statistical fluctuations. Within the off-time window the number of events in short time intervals with a duration of 100 s is observed. 100 s intervals are a reasonable choice because they provide sufficient statistics ($\sim (8-10)$ events/100 s at Level 3). Too small intervals result in insufficient statistics while too large intervals make it impossible to find instabilities on small time scales. Since the off-time window lasts two hours it contains 72 intervals with 100 s duration. In the cumulative test we inspect the cumulative distribution of the number of events in these 100 s intervals. If the detector is stable we expect this distribution to rise linearly. We number the bins consecutively starting from 1 to 72. Figure 5.4 shows the cumulative distribution of the data contained in one off-time window compared to the expected straight line. The deviation of the data from the

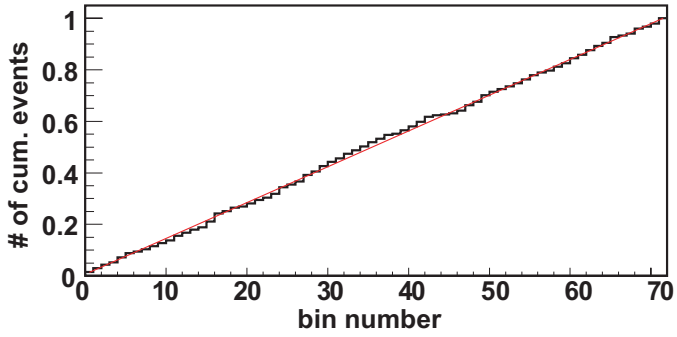

Figure 5.4: The cumulative event number distribution of the data contained in one off-time window is expected to follow a straight line. The bins are numbered consecutively and each bin corresponds to a 100 s interval.

straight line can be expressed by χ^2, which is defined as:

$$\chi^2 = \sum_{\text{bin}=1}^{72} (\text{content}(\text{bin}) - \text{bin}/72)^2 \ . \tag{5.1}$$

If the event rate is increased or decreased due to an instability over an expanded time period the calculated χ^2 would increase as well. The advantage of this method is that possible time correlations of the instability between the individual bins are taken into account. Obviously the method depends on the position of the instability among the 72 bins. To avoid this effect we shift the start bin position and calculate χ^2 for each possible start bin position. Figure 5.5 indicates the dependency of the χ^2 calculation from the start bin position. We find the maximal chi-square, χ^2_{max}, among the 72 calculated values

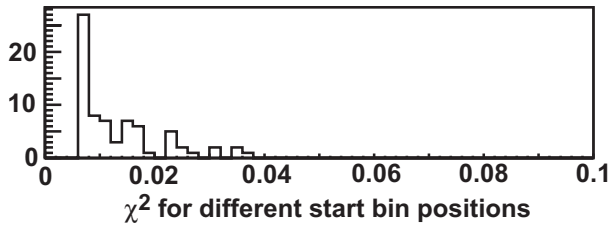

Figure 5.5: χ^2 of the cumulative event number distribution varies for different start bin positions.

for each burst. χ^2_{max} for each burst is plotted in figure 5.6. Large χ^2_{max} values indicate an

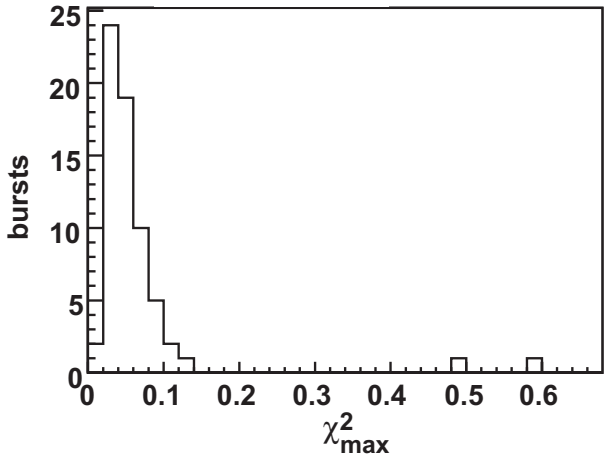

Figure 5.6: Distribution of χ^2_{max}.

instability in the off-time window. Thus a cut on χ^2_{max} is a separation criterion between stable and unstable bursts. A reasonable cut is suitable to exclude bad bursts but will not exclude a large amount of stable bursts. To select such a cut we generate 1000 Poisson

distributions with mean value[3] of 9, each containing 72 random values. The generated random values correspond to the measured event numbers. The cumulative distribution of the event number is investigated for each generated Poisson distribution and $\chi^2_{\max}$ of all possible bin positions is calculated. The cumulative distribution of the $\chi^2_{\max}$ distribution indicates, which cut value would keep 97.5 % of all stable bursts. Both, the distribution of $\chi^2_{\max}$ obtained by the MC simulation of 1000 Poisson distributions and its cumulative distribution are displayed in figure 5.7. A green line marks the 97.5 % level. A horizontal line from the intersection point of the green line with the cumulative curve yields the cut value that keeps 97.5 % of all stable bursts. The determined cut is $\chi^2_{\max} < 0.15$. Two

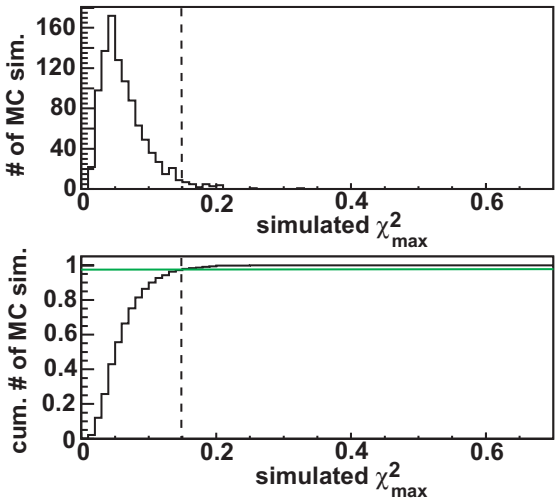

Figure 5.7: The distribution of $\chi^2_{\max}$ values obtained in the MC simulation of 1000 Poisson distributions (top) and its cumulative (bottom), a green line marks 97.5 % level. Bursts with a $\chi^2_{\max}$ larger than the intersection point of the green line and the generated distribution would be considered unstable. The chosen cut $\chi^2_{\max} < 0.15$ (dashed line) keeps 97.5 % of all stable bursts.

bursts (GRB010826 and GRB030304) do not pass this cut. The $\chi^2_{\max}$ of these bursts strikes out dramatically in the $\chi^2_{\max}$ distribution of all bursts. Closer investigations show (see figure 5.8) that obviously parts of the off-time data are missing. The missing data can be explained for by short runs that are excluded from the data sample due to instabilities that were found during the data processing. According to the defined stability criteria both burst are excluded from the analysis.

5.2.2 The Likelihood Test

In a stable detector the distribution of the number of events in short time intervals is expected to follow a Poissonian. The histogram of event numbers is filled with 72 entries

[3]The mean over the years 2000 - 2004 is 9.5, tests showed no significant dependence on the mean of the simulated distributions.

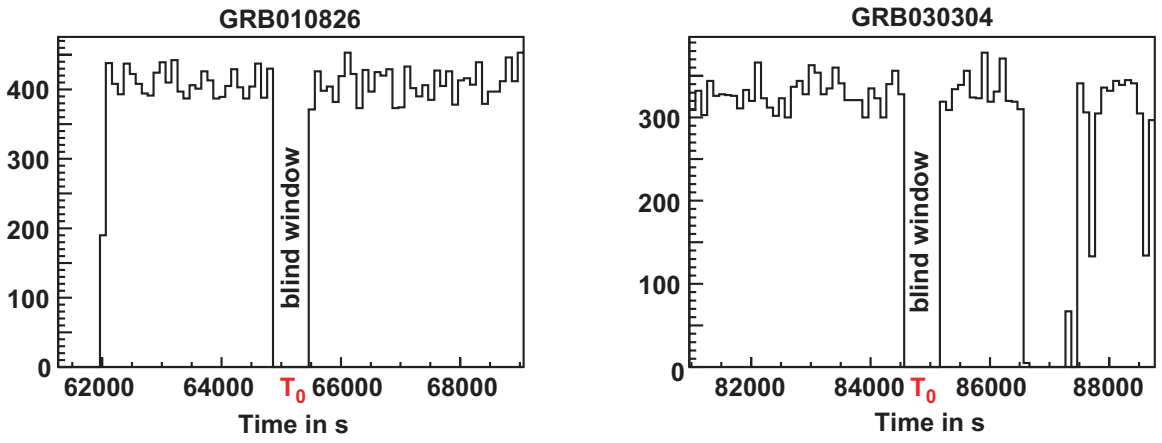

Figure 5.8: GRB010826 (left) and GRB030304 (right) show missing data in their off-time window. In order to receive better visability of the effect, Level 1 data with higher statistics is used for these plots to have better statistics.

when choosing 100 s intervals. The distribution is fitted with a discrete Poisson function with one degree of freedom (the mean λ) and a fixed norm of 72. Since the data is discrete, a discrete Poisson function matches the data better than a smooth one. The mean λ of the Poisson function is estimated in a maximum likelihood fit. The fit is performed using the ROOT[4] class TMinuit[5] to minimize -ln($\mathcal{L}$), which leads the same result as maximizing the likelihood $\mathcal{L}$ itself. Figure 5.9 gives an example of a Poisson fit to the two hour off-time window. Comparisons between the mean λ, resulting from the fit, and the yearly mean

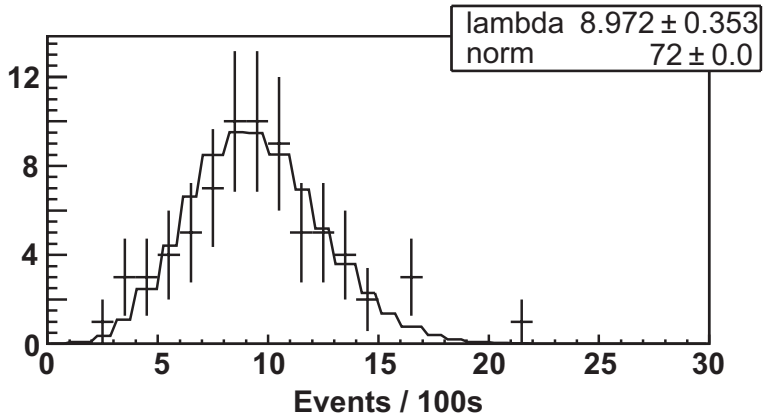

Figure 5.9: The histogram of event numbers in 100 s intervals in the off-time window is fitted with a discrete Poisson function with the fixed norm of 72 (according to 72 100 s bins in the two hour time window) and one degree of freedom by minimizing -ln($\mathcal{L}$).

event rate failed to provide a good criterion to find instabilities, since the events rate varies

[4]http://root.cern.ch/
[5]http://root.cern.ch/root/html/TMinuit.html

Table 5.1: Yearly events rates at Level 3 corrected for the dead time of the detector

Year	**2000**	**2001**	**2002**	**2003**	**2004**
Live Time (days)	197	193	204	213	194
Dead Time (%)	17.24	21.56	14.94	15.30	15.52
Average Event Rate (10^{-2} s^{-1})	7.93	8.93	10.13	10.21	10.54

over the year due to seasonal variations and also on a daily scale. Table 5.1 summarizes the yearly event rates corrected for the detector's dead time. Figure 5.10 clearly shows the seasonal variations. The seasonal variation can be explained by a domination of the data sample (even at Level 3) by atmospheric muons. The atmospheric muon rate follows temperature variations [58]. Therefore, we have developed a test which is independent of

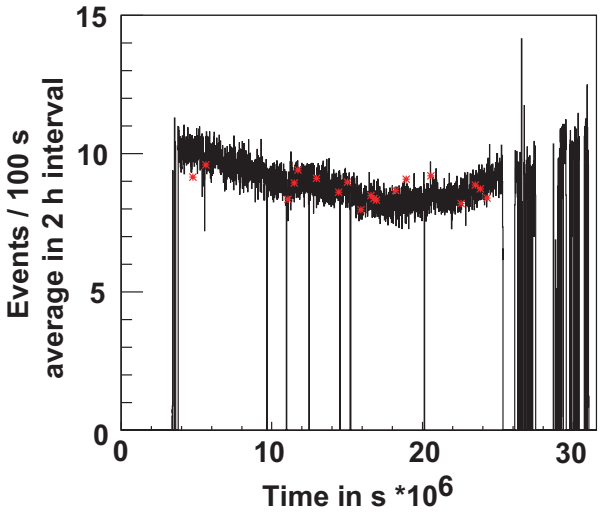

Figure 5.10: The variation of Level 3 event rates in 2001 shows a clear seasonal dependency and also fluctuations on a daily time scale. The red dots mark the mean event rate in the two hour off-time windows of the poorly localized bursts detected in 2001.

any mean rate.
The likelihood test uses the minimal -ln($\mathcal{L}$), $L_{\min}$, to identify detector instabilities. The $L_{\min}$ received by the Poisson fit is compared to the $L_{\min}$ distribution obtained in Poisson fits to 1000 generated Poisson distributions with 72 entries and mean λ. Here, λ is the mean estimated by the Poisson fit to the real data. Since the $L_{\min}$ distribution depends on the mean λ, which varies from burst to burst, the simulation is performed for each burst individually. Figure 5.11 shows one generated $L_{\min}$ distribution. In an instable detector event numbers in short time intervals are expected to differ from a Poisson distribution

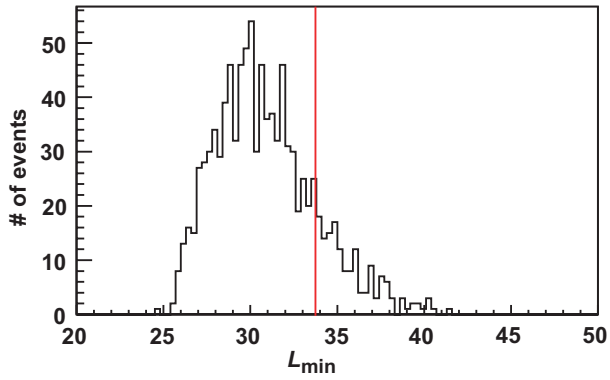

Figure 5.11: Simulated minimal -ln($\mathcal{L}$), $L_{\min}$, distribution obtained in fitting 1000 MC generated Poisson distributions with a discrete Poisson function. The red line marks the $L_{\min}$ resulting from the Poisson fit to the real data of the investigated burst.

and would therefore receive a low maximum likelihood in the Poisson fit or accordingly a high $L_{\min}$. Thus, a cut on $L_{\min}$ yields a separation criterion between stable and unstable off-time windows. The cut value is calculated for each burst individually by investigating the cumulative distribution of the generated $L_{\min}$ distribution. We choose the final cut in order to exclude less than 2.5 % of the stable bursts. Figure 5.12 presents the generated cumulative $L_{\min}$ distribution. A horizontal green line marks the 97.5 % level. Bursts with a $L_{\min}$ larger than the intersection point of the green line with the generated distribution are considered unstable. The vertical red line marks the $L_{\min}$ of the tested burst. This one passes the test. Four bursts do not pass the likelihood tests:

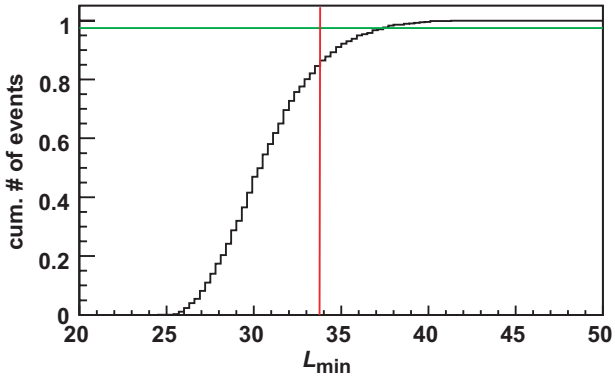

Figure 5.12: Simulated cumulative $L_{\min}$ distribution obtained in fitting 1000 MC generated Poisson distributions with a discrete Poisson function. The horizontal green line marks the 97.5 % level. Bursts with an $L_{\min}$ larger than the intersection point of the green line with the generated distribution would be considered unstable. The vertical red line marks the $L_{\min}$ of the tested burst, which passes the test.

- GRB010826
- GRB030215
- GRB030304
- GRB040409

Two of these bursts already failed the cumulative test. The remaining two are inspected closely. Looking at their rate regular dips attract attention. These gaps are due to the VLF veto excluding fake signals induced by a transmitting antenna installed 2 km from AMANDA-II. The VLF beacon experiment studies the mesosphere and lower ionosphere with low frequency electromagnetic waves emitted by the antenna. AMANDA-II responses to these electromagnetic signals, therefore no data is recorded during the transmission times of the antenna. These transmissions appear at 15 minute intervals and last for 60 seconds [6]. In figure 5.13 the rate for GRB040409 is plotted, which shows regular gaps due to the VLF veto. The VLF veto is not an instability but an understood behavior of the

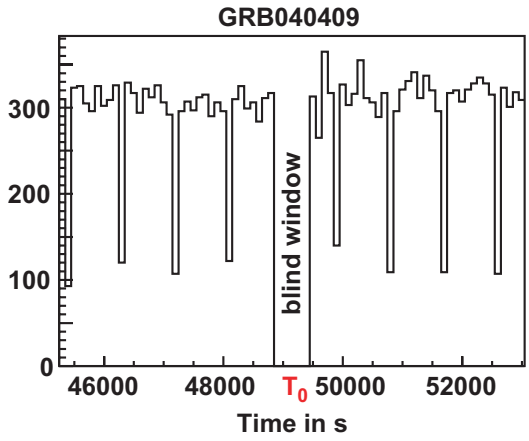

Figure 5.13: Rate (at Level 1) of a burst affected by the VLF veto: Gaps appear regularly in 15 minutes intervals and last for 60 s.

detector. Therefore, GRB030215 and GRB040409 are not excluded from the analysis.

5.2.3 ΔT-Distribution

In addition to the two tests the time between consecutive events ΔT in the off-time window was analyzed at Level 3. A stable detector is expected to show an exponential decay in the ΔT-distribution. An exponential fit is performed (see figure 5.14) to the ΔT-distribution for each GRB. Expectations predict a straight line in the logarithmic plot for a stable detector that does not distort the Poissonian distribution. The slope corresponds to the negative average rate. The plots are investigated by eye but no exclusion criterion is applied here. The first two bins show a slight deviation from the expected straight line due to dead time effects.

[6] The VLF veto appears every 6th, 21st, 36th and 51st minute of an hour (from private communication with W. Wagner and A. Tepe)

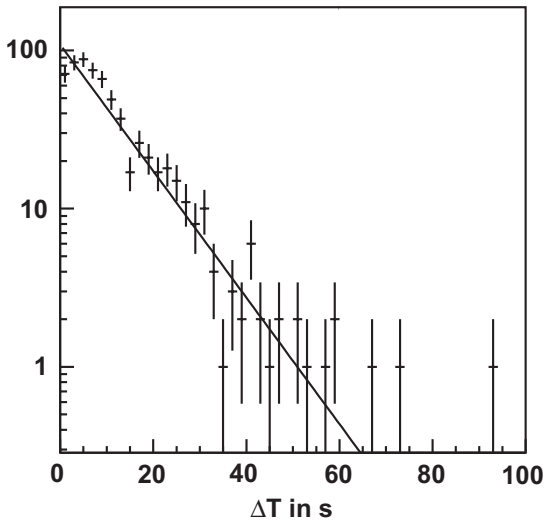

Figure 5.14: The distribution of the time ΔT between consecutive events is expected to fall off exponentially. An exponential fit is performed to the ΔT-distribution.

5.3 Reweighting of Simulated Events

5.3.1 Energy Reweighting

Instead of repeating CPU time consuming simulation steps for neutrino sources with different energy spectra, a universal event sample was produced at DESY-Zeuthen for all cases. This combined neutrino sample follows an E^{-1} energy spectrum and the neutrino-nucleon vertices are equally distributed within the interaction volume [49]. To obtain a meaningful GRB sample each event is weighted corresponding to the model prediction. The weight for an E^{γ} energy spectrum is given by[7]

$$w_i \cdot \frac{E}{\mathrm{GeV}} \cdot \left(\frac{E}{\mathrm{GeV}}\right)^{\gamma} \cdot \frac{w_{\mathrm{ep}}}{\mathrm{cm}^2} \cdot \frac{t}{s} \cdot \Omega \cdot \ln\left(\frac{E_{\mathrm{max}}}{E_{\mathrm{min}}}\right) \frac{1}{N_{\mathrm{gen}}} \ . \tag{5.2}$$

w_i is the initial weight according to the interaction probability calculated for each event in the MC generation and E its energy. w_{ep} accounts for the zenith dependent generation plane, where w_{ep} is defined by

$$w_{ep} = D(D|\cos(\theta)| + H\sin(\theta)). \tag{5.3}$$

D and H define the detector size, θ is the zenith angle. The AMANDA-II detector has a cylindrical shape with diameter of $D = 0.4\,\mathrm{km}$ and hight of $H = 0.8\,\mathrm{km}$. Equation 5.2 depends further on the lifetime t in seconds of the generated files. The generated events cover a solid angle of Ω. The original energy spectrum is generated in the range $E_{min} =$

[7] http://internal.icecube.wisc.edu/amanda/simulation/weight.html

10 GeV to $E_{max} = 10^8$ GeV, this results in the normalization factor $\ln(E_{max}/E_{min}) = 16.12$. N_{gen} is the number of generated ν_μ and $\bar{\nu}_\mu$ events. 10000 events are generated per file and 1460 files are used in this analysis. This yields a total number of generated events involved of

$$N_{gen} = 1460 \cdot 10000 = 1.46 \cdot 10^7 \ . \tag{5.4}$$

For an absolute normalization the weight has to be multiplied by the desired flux Φ, in this case the Waxman Bahcall spectrum given by equation 2.26. Figure 5.15 illustrates the energy reweighting and figure 5.16 the distribution of energy weights. The distribution of weights shows that the reweighted event sample is not dominated by a few events with high energy weights.

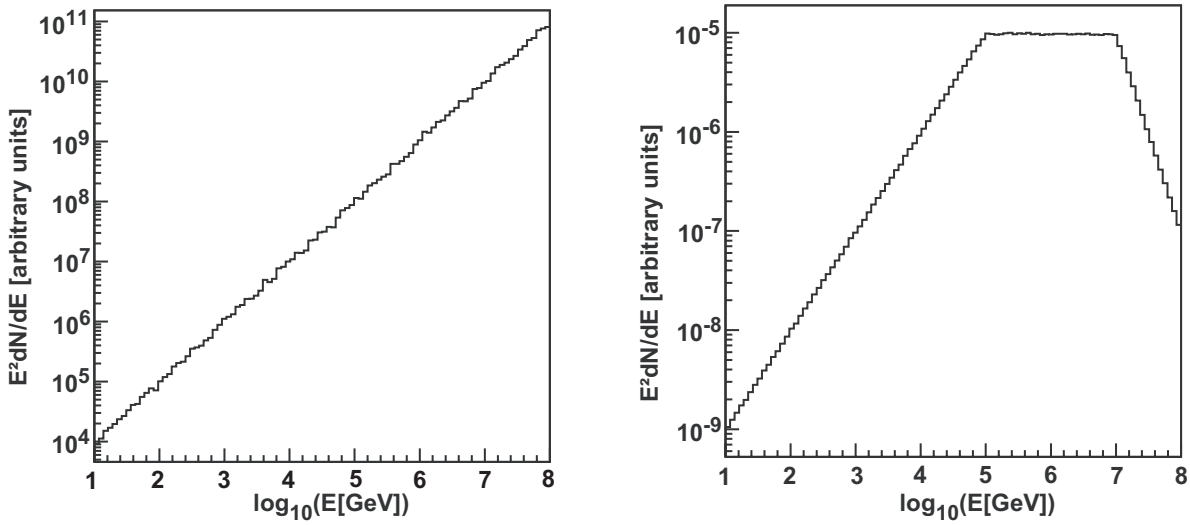

Figure 5.15: Plots produced with a toy model: Event rate following an E^{-1} energy spectrum (left) compared to the reweighted events following the energy spectrum predicted by the WB model prediction (right).

5.3.2 Directional Reweighting

One type of analyzed GRBs is detected by two non-direction sensitive IPN satellites and thus localized to a narrow annulus. The probability density $P(\alpha, \delta)$ (non-normalized) of finding the burst in the sky at the right ascension α and the declination δ follows a Gaussian distribution with mean at the center line of the annulus:

$$P_{IPN}(\alpha, \delta) = \frac{1}{\sigma\sqrt{2\pi}} \exp\left(-\frac{(d_{IPN}(\alpha, \delta) - r_{IPN})^2}{2\sigma^2}\right) \ . \tag{5.5}$$

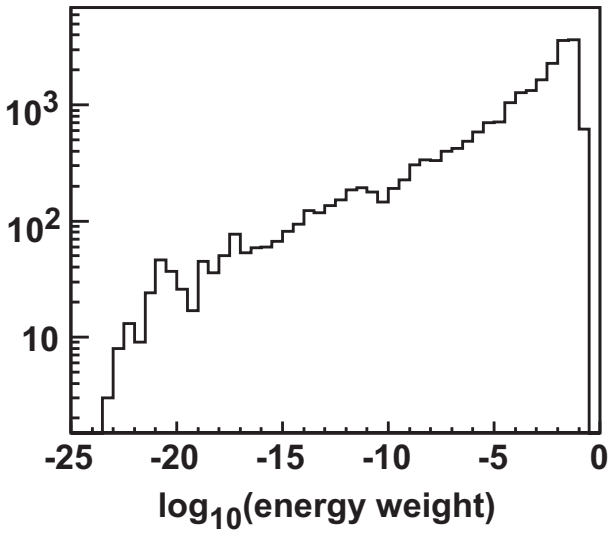

Figure 5.16: Distribution of energy weights. The reweighted sample is not dominated by single events.

$d_a(\alpha, \delta)$ describes the shortest distance of a point (α, δ) to the center line of the annulus a [8]:

$$d_a(\alpha, \delta) = |\arccos(\sin(\delta)\sin(\delta_a)) + \cos(\delta)\cos(\delta_a)\cos(\alpha - \alpha_a)|, \tag{5.6}$$

where α_a and δ_a are the right ascension and declination of the annulus center and r_a its central radius.
GRBs from the other type triggered the KONUS instrument and one non-direction sensitive IPN satellite, which selects a banana shaped segment from the IPN annulus. The probability density to find the burst in this intersection region of two annuli (IPN and KONUS) is proportional to the product of two normal distributions:

$$P(\alpha, \delta) = \frac{1}{\sigma_{\mathrm{IPN}}\sqrt{2\pi}} \exp\left(-\frac{(d_{\mathrm{IPN}}(\alpha, \delta) - r_{\mathrm{IPN}})^2}{2\sigma_{\mathrm{IPN}}^2}\right) \frac{1}{\sigma_{\mathrm{KON}}\sqrt{2\pi}} \exp\left(-\frac{(d_{\mathrm{KON}}(\alpha, \delta) - r_{\mathrm{KON}})^2}{2\sigma_{\mathrm{KON}}^2}\right). \tag{5.7}$$

A directional weight is assigned to each event proportional to the probability density. The distribution of these weights for one burst is shown in figure 5.17, it indicates that the reweighted event sample is not dominated by single events with high directional weights. Figure 5.18 illustrates the directional reweighting for one burst. The isotropically generated events are weighted with the probability given by equation 5.7. A loose directional cut is applied to the isotropically generated events in order to cut a banana shaped region from the sky corresponding to 9σ for the KONUS annulus and 1° for the IPN annulus, which typically has 9σ of less than 1°. Cutting an annulus smaller than 1° yield insufficient statistics. This cut is useful to save computing time in the cut optimization process, where it is necessary to loop over all events. This loose directional cut excludes events with a weight very close to zero and thus speeds up the cut optimization process. Events

[8] http://www.ssl.berkeley.edu/ipn3/FAQFORWEBSITE.pdf

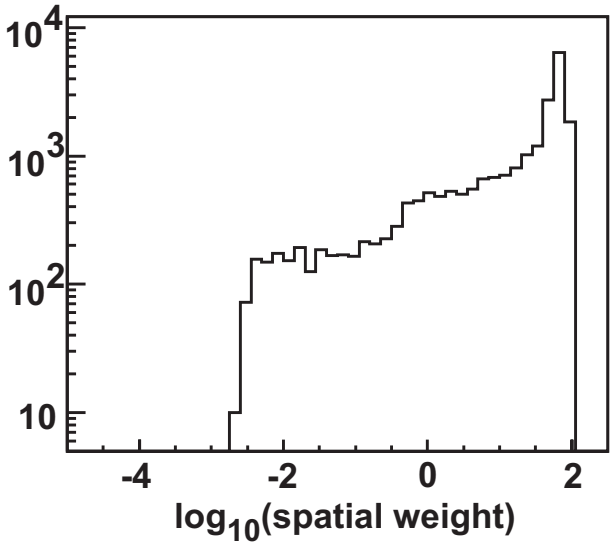

Figure 5.17: Distribution of directional weights.

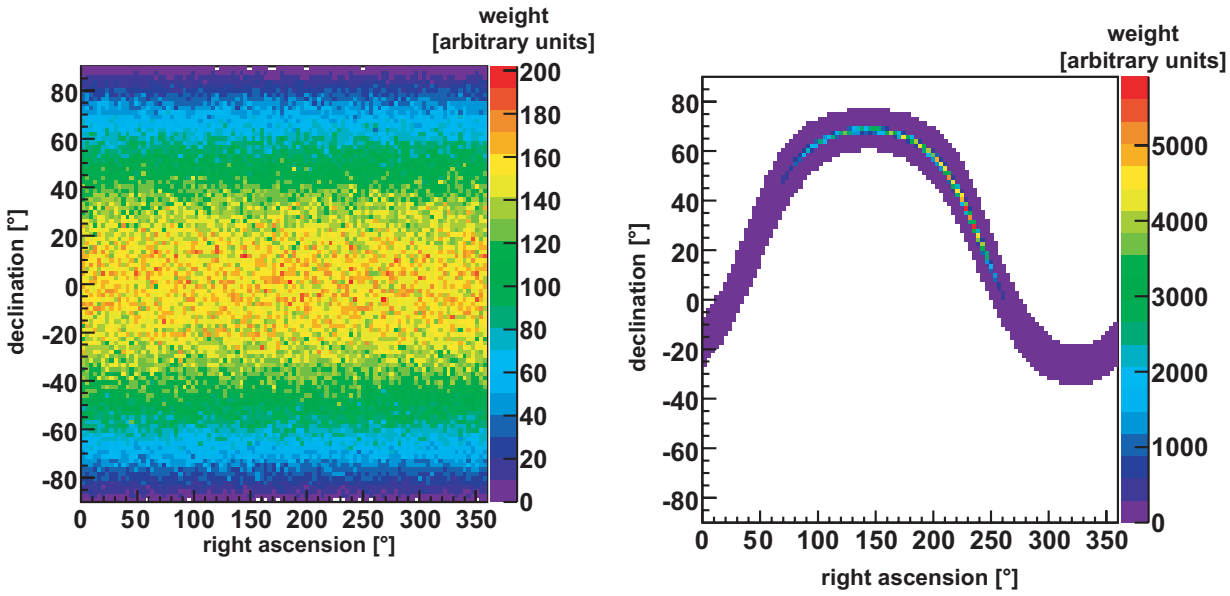

Figure 5.18: Plots produced with a toy model: The generated events (left) are isotropically distributed on a sphere. The distribution appears not isotropically because the plot is not spherical. The generated events receive a directional weight according to the probability to find the GRB within the localization region (right). White regions in the right plot have a weight which is numerically not distinguishable from zero.

passing this loose cut are saved to a new file[9] for each burst. In order to obtain reasonable statistics, simulated events from all years (2000 - 2004) are used to select the burst events.

[9]ROOT NTuples are used to store the reconstructed events

The number of events per burst ranges from 8000 to 25000. The variation in the event number is caused by variations in the solid angle of the burst localization region.

Normalization

Absolute normalization is necessary to ensure a total probability of unity for the GRB event to happen in the generation solid angle Ω. The total probability is given by:

$$\int_{\Omega} P(\alpha,\delta)d\Omega \approx \Omega \cdot \langle P(\alpha,\delta)\rangle \approx \Omega \cdot \frac{1}{N} \cdot \sum_{i=1}^{N} P_i \ . \tag{5.8}$$

The directional weight $P(\alpha,\delta)$ assigned to each event is proportional to the probability density, but it is not normalized yet. To take into account the normalization, each weight assigned to an event at Level 3 is divided by the sum over all weights P_i in the generation area Ω. In the combination of directional and energy weight the solid angle Ω cancels. Since the reweighting takes place at Level 3, N is the total number of events contained in all Level 3 files used taking into account corrections for the energy reweighting. This number is not equal to the number of generated events, firstly because not every generated event triggers the detector and secondly not every reconstructed event passes the Level 3 cleaning cuts. The fraction of events passing the cleaning cuts depends on the input energy spectrum. The input energy spectrum in the used simulated sample follows E^{-1}. According to table 4.5, 57 % of all generated events survive at Level 3. The WB spectrum used in the analysis has a different energy dependence (see equation 2.26). The bulk of events (64.3 %) in the final burst files are in the E^{-2} regime of the neutrino energy spectrum. 35.1 % of the events follow an E^{-1} spectrum and 0.6 % an E^{-4} spectrum. E^{-4} spectra are not treated separately in the simulation of [49] and thus the exact signal passing rate is not known. For softer spectra the signal passing rate increases, so we can conservatively assume a signal passing rate of 0.88 which is the passing rate for E^{-3} spectra. Since only 0.6 % of the events are in this regime this inaccuracy can be safely neglected. With this information we estimate the average passing rate for GRB neutrino events:

$$0.351 \cdot 0.57 + 0.643 \cdot 0.80 + 0.006 \cdot 0.88 = 0.720 \tag{5.9}$$

72.0 % of all simulated GRB neutrino events pass the Level 3 cleaning cuts. The relevant N in equation 5.8 becomes

$$N = N_{L3} \cdot \frac{0.72}{0.57} \ , \tag{5.10}$$

Inserting the total number of Level 3 events in the used sample $N_{L3} = 2.6 \cdot 10^6$ yields

$$N = 3.3 \cdot 10^6 \ . \tag{5.11}$$

5.4 Cut Variable Selection

Following foregoing analyses several variables have been examined. The following ones have been selected to provide a good separation of background and signal.

- Temporal Cut
- Directional Cut
- Angular resolution given by the paraboloid fit
- Smoothness
- Maximum Likelihood Value

The first two cuts use the information provided by the satellites assuming the temporal and directional coincidence of gamma and neutrino emission predicted by the fireball model. The latter three cuts are quality cuts to filter down-going events, which are reconstructed badly and thus appear as up-going events. These events form the main background of this analysis since they dominate the Level 3 sample. A smaller part of the background consists of atmospheric neutrinos and can only be separated to some extent by their direction using directional cuts. The cut variable selection will be motivated in the following sections.

5.4.1 Temporal Cut / Definition of the Search Window

GRBs typically last for 50 s. Based on model predictions we expect neutrino emission in temporal coincidence with the gamma emission. The time window of the gamma emission is defined by the burst start time T_0 given in the IPN catalog and the burst duration, in which the burst emits clearly detectable emission. The neutrino search is performed in a corresponding time window. To account for uncertainties in the start time due to Earth crossing time corrections (see section 3.1) the neutrino search window starts 10 seconds before the burst start time. Accounting conservatively for possible uncertainties, which could shorten the measured duration, the window lasts one second longer than the gamma emission in order to avoid missing any neutrino signal. This results in the time interval:

$$[T_0 - 10 \text{ s}, T_0 + \mathsf{duration} + 1 \text{ s}] \tag{5.12}$$

The neutrino search window definition is illustrated in figure 5.19. The number of background events is reduced dramatically by assuming the coincidence of gamma and neutrino emission, which allows to limit the search to the time window defined above.

5.4.2 Directional Cut

The directional cut reduces the neutrino search to the burst localization region. In the treated case of poor localization the search region is restricted to regions with a high probability of finding the burst. The probability distribution is determined by the satellite measurements. It follows a Gaussian distribution if the burst triggers two non-direction sensitive IPN satellites or the product of two normal distributions when KONUS and one non-direction sensitive satellite were triggered. The non-normalized probability density is

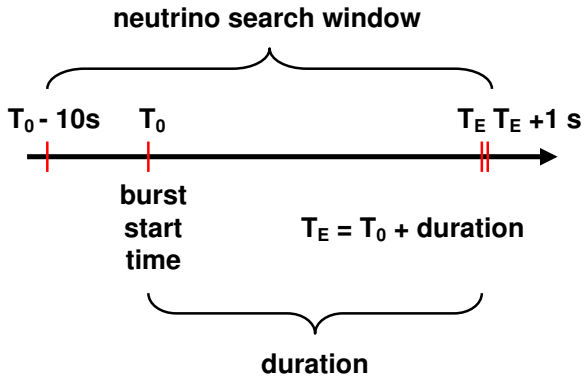

Figure 5.19: Neutrino Search Window: The neutrino emission is expected in coincidence with the gamma emission, which starts at the burst start time T_0 and lasts for the burst duration until T_E. To account for uncertainties due to Earth crossing time corrections the neutrino search window starts 10 seconds before the burst start time and lasts one second longer.

given by equation 5.5 and equation 5.7, respectively.
The background decreases approximately linearly with decreasing size of the search area. Although the localization region determined in the satellite measurement is relatively narrow, the search area cannot be restricted in the same way. The directional weight assigned to each events is calculated for its true MC direction in order to simulate the burst neutrino emission from the direction given by the satellites. But the final directional selection cut can only be applied to the reconstructed direction. The direction of real data events recorded in AMANDA-II can only be obtained by reconstruction. The true direction is only known for simulated events. It has to be kept in mind that the reconstruction of the direction introduces non-negligible uncertainties to the direction information. The mean deviation angle is $\sim 2^\circ$ for the energies of interest, but the deviation for individual events can be much larger. Figure 5.20 shows the true direction of pre-selected events[10] in one burst file and compares it to the reconstructed direction (32-fold Pandel likelihood fit) of the same events. At this point no weights are assigned to the plotted events. The region around the true direction given by the satellite measurements contains most of the reconstructed event directions. Therefore, a directional cut has to select such a region. The distance from the center line of the banana or annulus could be used to define the region or more naturally the function $P(\alpha, \delta)$, which depends on this distance. Here, α and δ are the reconstructed right ascension and declination. Since the function $P(\alpha, \delta)$ falls off rapidly with the distance of an event from the annulus center line, the cut is applied to the logarithm to avoid numerical problems. To account for increased background rates close to the horizon, an additional declination dependence is added to the directional cut. The declination dependence tightens the cut at small and widens it at large declinations.

[10]The pre-selection in order to reduce CPU time is described in section 5.3.2

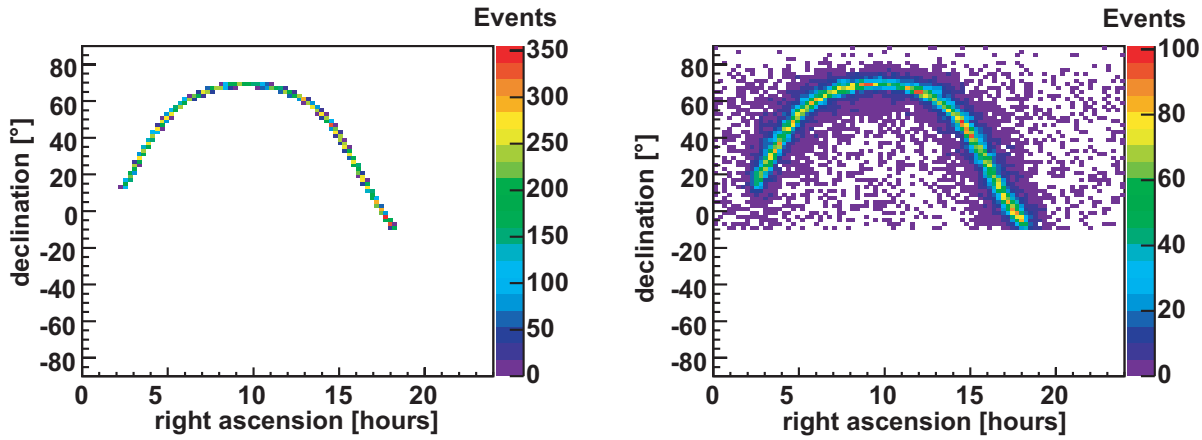

Figure 5.20: MC true direction (left) compared to reconstructed direction by the 32-fold Pandel likelihood fit (right): The mean deviation angle is 2° [45], but can be much larger for individual events. At this point no weights are assigned to the events.

The cut can be adjusted by two parameters space_a and space_b following

$$\ln(P(\alpha,\delta)) < \text{space\_a} + \delta/90^\circ \cdot \text{space\_b} \ . \tag{5.13}$$

A technical problem occurred at this point: The processed AMANDA data files contain the variables declination and right ascension for the years 2000 - 2003. 2004 processing did not include equatorial, but only detector coordinates, zenith and azimuth. To perform the conversion from detector coordinates to equatorial coordinates classes of the coordinate services contained in the *IceTray* software package[11] based on functions from the *slalib* library [59] are used. The conversion is not trivial since not only the Earth rotation but also further effects like precession and nutation have to be taken into account (as described in section 3.2.1).

Cut on Declination

Close to the horizon the number of background events originating in atmospheric processes increases significantly. Therefore, an additional directional cut on the declination is introduced. This cut is applied to the declination reconstructed by the first guess Pandel fit. This reconstruction is suited well for this cut, since no cleaning cut was applied to it during data processing. Figure 5.21 illustrates the different declination dependence of background and simulated signal at Level 3 prior to applying further selection cuts.

5.4.3 Reconstruction Quality Cuts

In addition to the temporal and directional cuts reconstruction quality cuts are applied to reduce the background consisting of misreconstructed down-going muons. The track

[11] developed and used by the IceCube collaboration

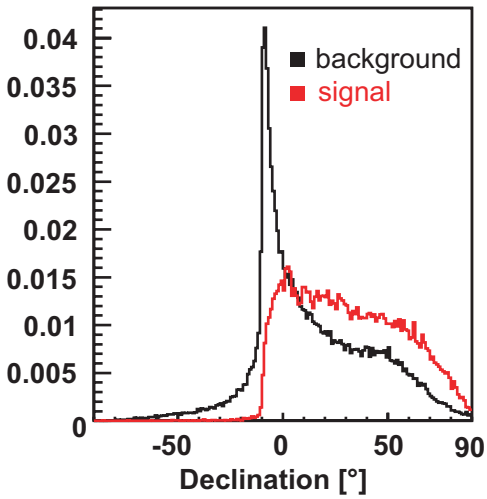

Figure 5.21: Declination reconstructed by the first guess Pandel fit: Signal (red) and background (black) show different declination dependence at Level 3. The background increases significantly close to the horizon.

quality parameters angular resolution, maximum likelihood and smoothness introduced in section 4.4.4 are used. Their distribution for simulated signals is compared to the distribution of the background (off-time recorded AMANDA-II data).

Angular Resolution

The angular resolution describes the error in the reconstructed direction estimated from the shape and size of the negative likelihood valley and can thus identify badly reconstructed events. The distribution of the angular resolution for background and simulated neutrino signal, both at Level 3, is compared in figure 5.22. Reconstructed signal events tend to have a better angular resolution compared to reconstructed background, which is dominated by misreconstructed down-going events. The background distribution peaks at $\sim 7°$ while the signal distribution reaches its maximum at $\sim 2°$.

Smoothness

The P_{hit} smoothness S describes the cumulative distribution of the hits along the muon track. Values close to 1 indicate that hits are found in OMs where none would be expected while values close to -1 state that hits are missing in OMs where hits would be expected. Both cases indicate a possible misreconstruction. A comparison of the smoothness distribution of signal and background at Level 3 is shown in figure 5.23. Both distributions are almost symmetric with respect to zero. The slight asymmetry might be explained by the detector geometry. The cut is applied to the absolute value of the smoothness. Background events tend to have larger absolute smoothness values than signal events. The background distribution peaks at $|S| \sim 0.4$ while the signal peaks at $|S| \sim 0.15$.

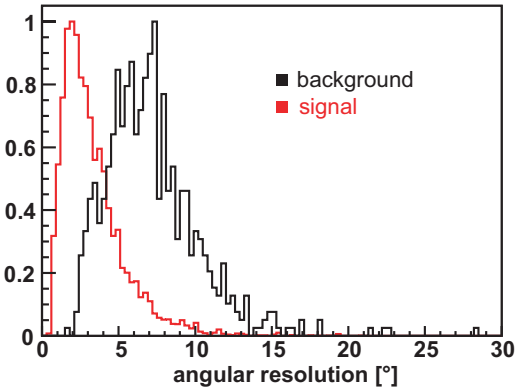

Figure 5.22: Distribution of the angular resolution compared for background (black) and signal (red) at Level 3.

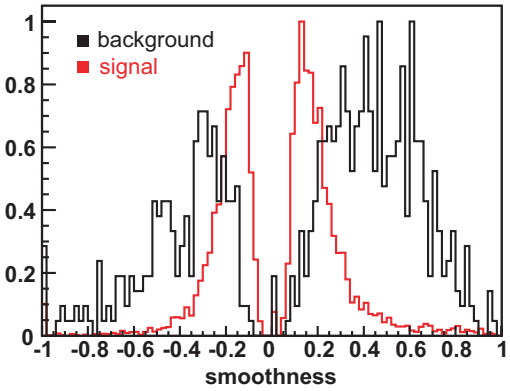

Figure 5.23: Distribution of P_{hit} smoothness compared for background (black) and signal (red) at Level 3.

Maximum Likelihood

The maximum likelihood evaluated in a likelihood reconstruction naturally indicates the quality of the reconstruction. The negative logarithm of the likelihood given by equation 4.10 is expected to be large for misreconstructed events. Figure 5.24 compares the minimal -ln($\mathcal{L}$), L_{min}, distribution resulting from the 32-fold iterative Pandel likelihood reconstruction seeded on the JAMS first guess fit for signal and background at Level 3. The L_{min} distribution resulting from the reconstruction of signal events peaks at ~ 7 while the reconstruction of background events is worse with a peak at ~ 8.

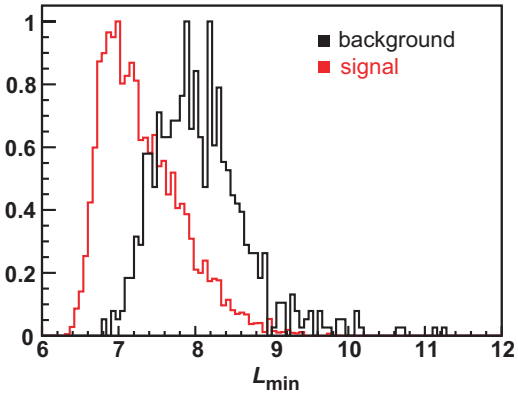

Figure 5.24: Minimal -ln($\mathcal{L}$), $L_{\min}$, distribution resulting from the 32-fold iterative Pandel likelihood reconstruction seeded on the JAMS first guess fit for signal (red) and background (black) at Level 3.

5.5 Cut Optimization

The cuts on the selected variables are optimized by minimizing the *Model Rejection Factor* (MRF) [60]. This method allows to optimize experimental cuts in order to place the most restrictive limit on a signal model. Minimizing the MRF is a different approach replacing the common maximization of the significance usually applied in particle physics. For very small numbers of expected signal events the common method, to maximize the signal over noise ratio or the signal over square root noise ratio, is not applicable any more. In this case an upper limit on the expected flux can be derived from the experimental observation. The method assumes that no signal event is observed and compares the number of observed events with the number of expected events from the known background sources in order to check their compatibility and thereby it determines the room for a physical signal.

5.5.1 Confidence Belt and Upper Limit

Upper limits are defined for a certain confidence level $1 - \alpha$. Considering a given probability function $p(n)_{s+b}$ to observe n events for a fixed but unknown signal s and a known background with mean b a set of intervals $[n_1, n_2]$ (the so called *confidence belt*) can be found for every value of s, which fulfill:

$$\sum_{n=n_1}^{n_2} p(n)_{s+b} = 1 - \alpha \ . \tag{5.14}$$

To make the choice of n_1 and n_2 unique Feldman and Cousins [61] proposed a "unified approach". An ordering principle is applied that ranks the values n dependent on their

likelihood ratio

$$R(s,n) = \frac{\mathcal{L}_{s+b}(n)}{\mathcal{L}_{s_{best}+b}(n)} \ , \tag{5.15}$$

where s_{best} maximizes the likelihood $\mathcal{L}_{s+b}(n)$ for a given n. The values n are included in the confidence belt according to their rank, starting with the n with the highest $R(s,n)$ and then with decreasing $R(s,n)$ until $\sum_{n=n_1}^{n_2} p(n)_{s+b}$ reaches the confidence level $1-\alpha$. The upper bound n_2 of this unique confidence interval is called the *Feldman-Cousins upper limit*.

5.5.2 Average Flux Upper Limit

The average flux limit for the 90 % confidence interval is defined as:

$$\bar{\Phi}(E)_{90} = \Phi(E)\frac{\bar{\mu}_{90}(n_b)}{n_s}. \tag{5.16}$$

n_s the number of expected signal events produced by the theoretical source spectrum $\Phi(E)$ estimated in MC simulations. The average Feldman-Cousins upper limit [61] for the 90 % confidence interval $\bar{\mu}_{90}$ depends on the number of expected background events n_b and is defined as the sum over all expected upper limits (for all possible numbers of observed events n_{obs}), weighted by their Poisson probability of occurrence and assuming that only background will be observed:

$$\bar{\mu}_{90}(n_b) = \sum_{n_{obs}=0}^{\infty} \mu_{90}(n_{obs}, n_b)\frac{(n_b)^{n_{obs}}}{(n_{obs})!}\exp(-n_b) \ . \tag{5.17}$$

It is necessary to work with this average upper limit because n_{obs} is not known until the cuts are defined and the experiment is performed. For a hypothetical ensemble of identical experiments, the strongest constraint on the predicted theoretical signal flux $\Phi(E)$ is obtained if the model rejection factor

$$\mathrm{MRF} = \frac{\bar{\mu}_{90}(n_b)}{n_s} \tag{5.18}$$

is minimal. The optimal set of cuts minimizes the model rejection factor. These cuts have to be determined before looking at the experimental data in order to avoid a bias introduction and to ensure that the derived intervals cover the unknown value at exactly the stated confidence of 90 %. [60]

5.5.3 Optimization Technique

The MRF depends on each cut variable. Changing one cut influences the dependence of the MRF on the other cuts. First we developed a method to optimize the cuts in

order to find the most stringent limit to the average flux of a single burst for each burst separately. We adjusted this method to obtain the lowest limit to the combined average flux for all analyzed bursts. The optimization for the single burst limit will be introduced first followed by a description of the enhancement of this method to account for the combination of the single burst results. Both methods are based on the calculation of the MRF described below.

Calculation of the MRF

To calculate the MRF the number of expected signal and background events passing the cuts have to be determined. The first one is calculated from the reweighted MC. The sum over the assigned weights (see section 5.3) yields the number of signal events predicted by the model flux. Several hours of off-time recorded AMANDA data, treated as background in the coincidence search, are contained in the background files. The time window was increased compared to the two hours used for the detector stability tests (see section 5.2). This is necessary because the number of events contained in two hours of data is roughly 700. These events are distributed in the Northern sky and only a few events pass the directional cut. These do not provide sufficient statistics to determine the best set of cuts. The on-time window stayed blind during the expansion of the off-time window. The enlarged files contained 40000 - 80000 events. The number of background events N_p passing the cuts had to be rescaled according to the neutrino search time window to obtain the number of expected background events within the search time window. Using the two hour off-time window allows to calculate the expected number of background events N_{BG} in the search time window by assuming a constant rate during this two hour interval:

$$N_{\mathrm{BG,2h}} = N_{p,2h}\frac{10\,\mathrm{s} + \mathsf{duration} + 1\,\mathrm{s}}{7200\,\mathrm{s}} \ . \tag{5.19}$$

The length of the search time window is given by $10\,\mathrm{s} + \mathsf{duration} + 1\,\mathrm{s}$. Equation 5.19 can be used only if no data is missing during these two hours. The detector stability is tested in these two hours and therefore this requirement is fulfilled. But for the expanded files we cannot be sure. Thus, the mean rate $R = \frac{N_{2h}}{7200\,\mathrm{s}}$ calculated from the number of events in the two hour off-time window N_{2h} is used to estimate the number of background events expected by:

$$N_{\mathrm{BG}} = N_p\frac{10\,\mathrm{s} + \mathsf{duration} + 1\,\mathrm{s}}{N_{\mathrm{file}}/R} \ , \tag{5.20}$$

where N_{file} is the number of events contained in the enlarged background file and N_p the number of events passing the cuts.

Single Burst Optimization

In order to obtain the best cuts, the global minimum of the MRF in the six dimensional parameter space[12] has to be found. To determine this minimum the six dimensional

[12]The six parameters used are space_a, space_b, declination, angular resolution, smoothness and maximum likelihood value.

parameter space is scanned in an iterative way. Start cut values for each parameter are chosen by eye to provide a good separation between background and signal. Each cut value is changed from its start value while the others are fixed to their start value. Different values are tested in each optimization step covering the interval

$$[\mathsf{cut}_{\mathsf{start}} - 50 \cdot \mathsf{step}_{\mathsf{cut}}, \mathsf{cut}_{\mathsf{start}} + 50 \cdot \mathsf{step}_{\mathsf{cut}}] \ , \tag{5.21}$$

with a step size $\mathsf{step}_{\mathsf{cut}}$ adjusted separately per eye for each parameter. For each of the 101 variations the relative MRF is calculated. Differing from the definition of the MRF given by equation 5.18 we use the relative MRF defined as

$$\mathrm{MRF}_{\mathrm{rel}} = \frac{\bar{\mu}_{90}(\mathrm{N_{BG}})}{\mathrm{s}} \ , \tag{5.22}$$

where s is the signal passing rate at Level 3 given by the ratio of the number of events at Level 3 after and before applying any selection cuts. Since for a single burst the number of events before cuts stays constant, either minimizing the relative MRF or minimizing the actual MRF, will result in the same set of cuts. 606 different relative MRFs are determined since the variation is performed for each of the six selected cut variables. One changed cut variable yields the smallest MRF among all 606 variations. The corresponding cut for this variable is stored as the start value for this variable while the start values of the other variables are kept at the old start value. The procedure is repeated until the change in the MRF to the next step is smaller than 0.001. Figure 5.25 illustrates the optimization process schematically. This method might not return the global minimum, but a local minimum instead. However, the scanned region given by 5.21 in one dimension covers the possible range of values sweepingly. Assuming that large fluctuation does not appear on scales smaller than the step size the iterative method is very robust.

Combined Burst Optimization

In fact, to receive the best combined limit, the minimal MRF for the combination of all 64 bursts has to be found, which would mean to search for a global minimum in a 64×6 dimensional parameter space. This optimization is not feasible. Therefore, we have developed a method that scans the six dimensional parameter space of each burst separately in an iterative way taking into account the combination. The shape of the localization region differs a lot from burst to burst. Thus, it is desirable to have a separate set of cuts for each burst. To incorporate the fact that the single burst results will be combined to a combined flux limit for all analyzed bursts we adjust the number of expected background events. In the combination the number of background events increases since the total search time window is longer than the single burst window. The single burst optimization does not account for the increase in background due to this fact. Therefore, we adjust the iterative method described above slightly. Instead of using the expected background in the single burst search time window, we calculate the relative MRF using the expected background scaled with the total search time for all bursts. This

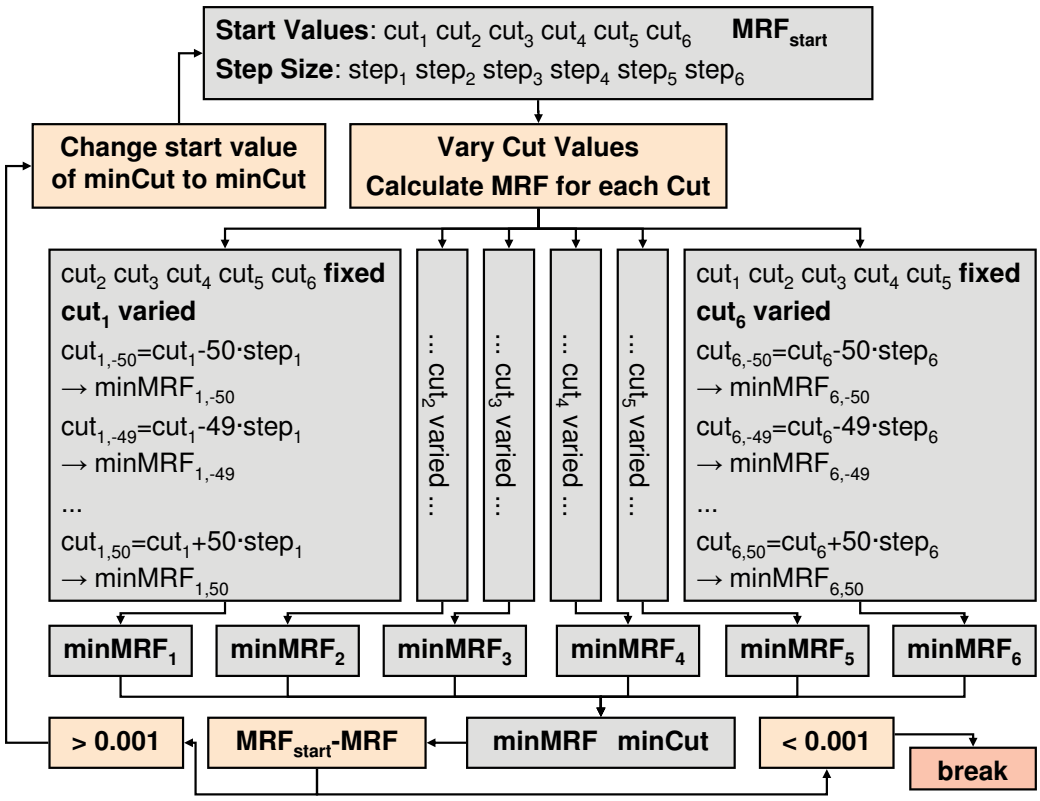

Figure 5.25: Scheme of the iterative optimization process

background for a burst j is given by

$$N_{\mathrm{BG,j}}^{\mathrm{com}} = \frac{N_{p,j}}{N_{\mathrm{file}}/R} \cdot (64 \cdot 10\,\mathrm{s} + \sum_{\mathrm{i}=1}^{64} \mathsf{duration_i} + 64 \cdot 1\,\mathrm{s}) \cdot \frac{\mathsf{duration_j}}{40\,\mathrm{s}} \ , \tag{5.23}$$

where $N_{p,j}$ is the number of events passing the cuts for the burst j and N_{file} is the initial number of events contained in the file before selection cuts are applied. The last factor $\frac{\mathsf{duration_j}}{40\,\mathrm{s}}$ is the ratio of the duration of the burst j to the mean duration of all 64 bursts. Taking into account the individual burst duration, results in tighter cuts for long burst and wider cuts for short bursts. This is desirable because the number of background events increases linearly with the burst duration, while the number of signal events is expected to stay constant, since the theoretical model predicts a constant integrated neutrino emission.
The signal passing rate needed for the calculation is treated the same way as in the single burst optimization, it is not affected by the combination. Note, that this method does not return the optimal set of cuts that lead to the lowest flux upper limit. However, the results obtained by the developed method are close to the optimal values. Advantage of this method is its low CPU time consumption and its robustness.
The same set of start values is used for the optimization of each burst. These start values and the corresponding step size for each variable are summarized in table 5.2. Figure 5.26

Table 5.2: start values and step size used in cut optimization

Cut Variable	Start Value	Step Value
space_a	-50	1.0
space_b	-500	10.0
declination [°]	-5	0.1
angular resolution [°]	8.0	0.1
smoothness	0.5	0.01
likelihood	9.0	0.1

displays the dependence of the MRF on variations of the cut values. GRB000309 is selected as an example. The dependence of the single variables changes from burst to burst. Some bursts are not sensitive to the variation of single cut variables, while others are sensitive to that variable. To realize an automated optimization the same variables are used for all bursts. If the burst is not sensitive to a certain cut variable the cut becomes redundant. This results in a extremely loose cut that does not effect signal and background passing rates. For this reason some MRF vs. cut curves are flat while others show a distinct minimum. The cut which yields the minimal MRF is considered the best cut. The optimization process as described above provides the best set of cuts for each burst. The distributions of best cut values for each variable are shown in figure 5.27. The directional cuts show the strongest fluctuations according to different shaped localization regions for every burst. For each burst the number of background and signal events passing the cuts are determined. Their distribution and a scatter plot are shown in figure 5.28. If in the combination single bursts were responsible for a large fraction of the total background, excluding these bursts might lead to a better combined limit. *Good* bursts in the combination are those bursts with a low MRF[13] resulting from the optimization. One burst after the other is included in the combined MRF starting with the best one, which is the one with the lowest MRF. For each combination i the combined MRF is calculated:

$$\mathrm{MRF}_i^{\mathrm{com}} = \bar{\mu}_{90} \left(\sum_{k=1}^{i} b_k \right) / \sum_{k=1}^{i} s_k \ , \tag{5.24}$$

where b_k is the number of expected background events and s_k the number of predicted signal events for a single burst k. The dependency of the combined MRF on the number of included bursts is displayed in figure 5.29. No minimum occurs but the curve falls off continuously. Therefore, the best combination that yields the most stringent flux upper limit is the combination of all bursts. Combining all bursts leads to a total number of

[13]Note, here the absolute instead of the relative MRF is used to make the single burst MRFs comparable.

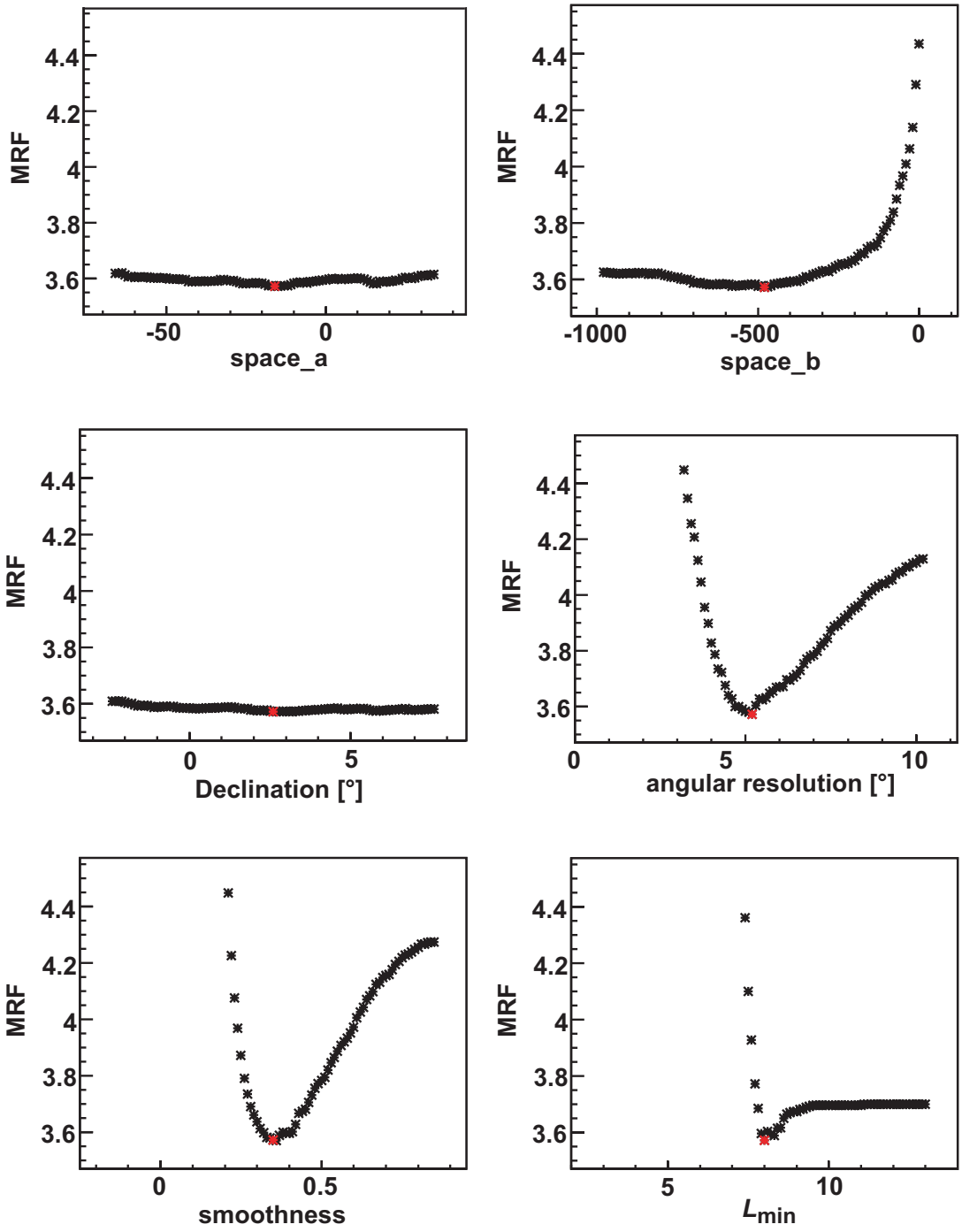

Figure 5.26: The MRF depends on the single cut values. The best cut values (marked red) minimizes the MRF. Shown is the last iteration step of GRB00309.

expected background events b_{com}

$$b_{\text{com}} = \sum_{k=1}^{64} b_k = 0.17 \tag{5.25}$$

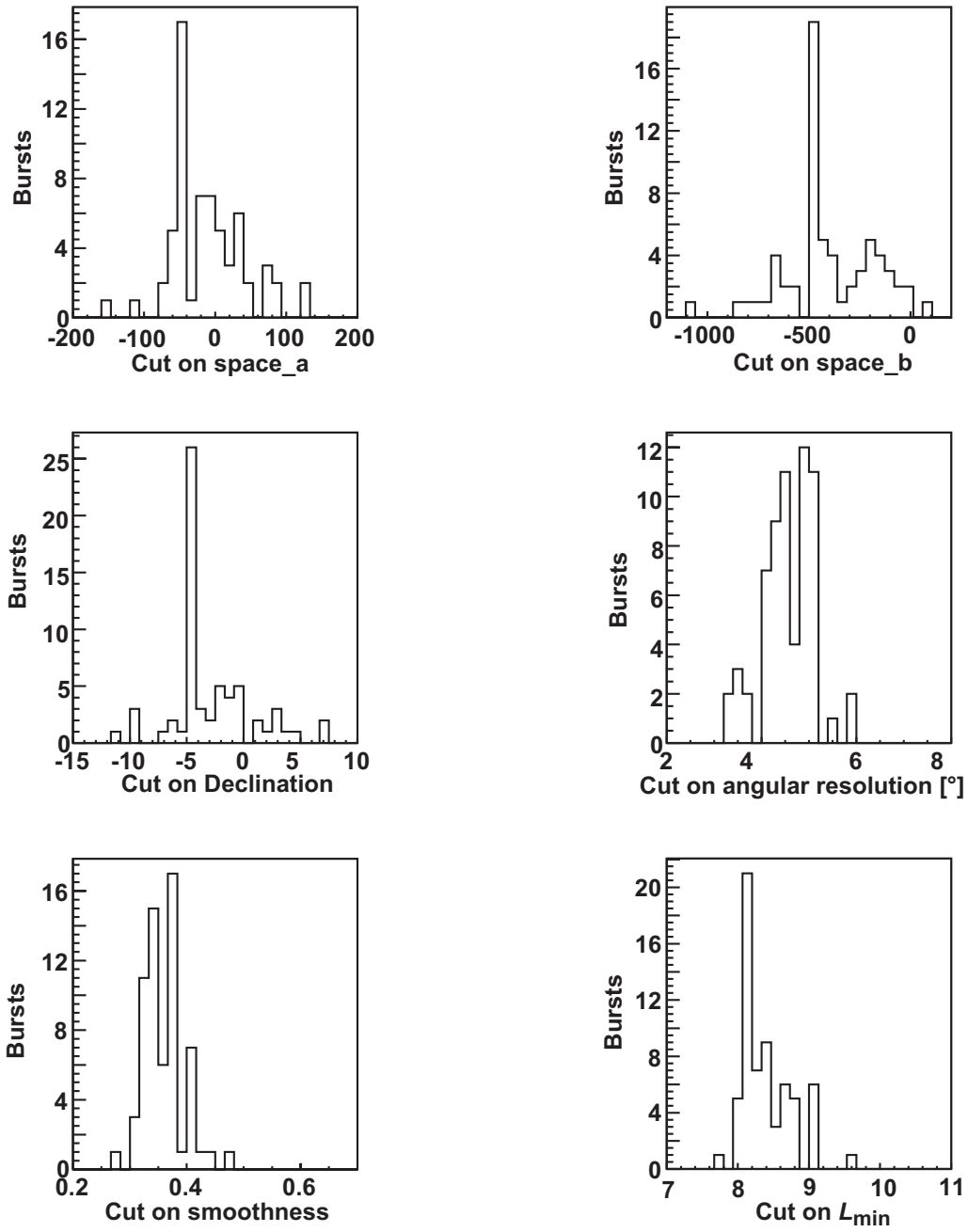

Figure 5.27: Distribution of selected cut values for all 64 bursts.

and a total number of predicted signal events by the WB model spectrum s_{com}

$$s_{\mathrm{com}} = \sum_{k=1}^{64} s_k = 0.34 \tag{5.26}$$

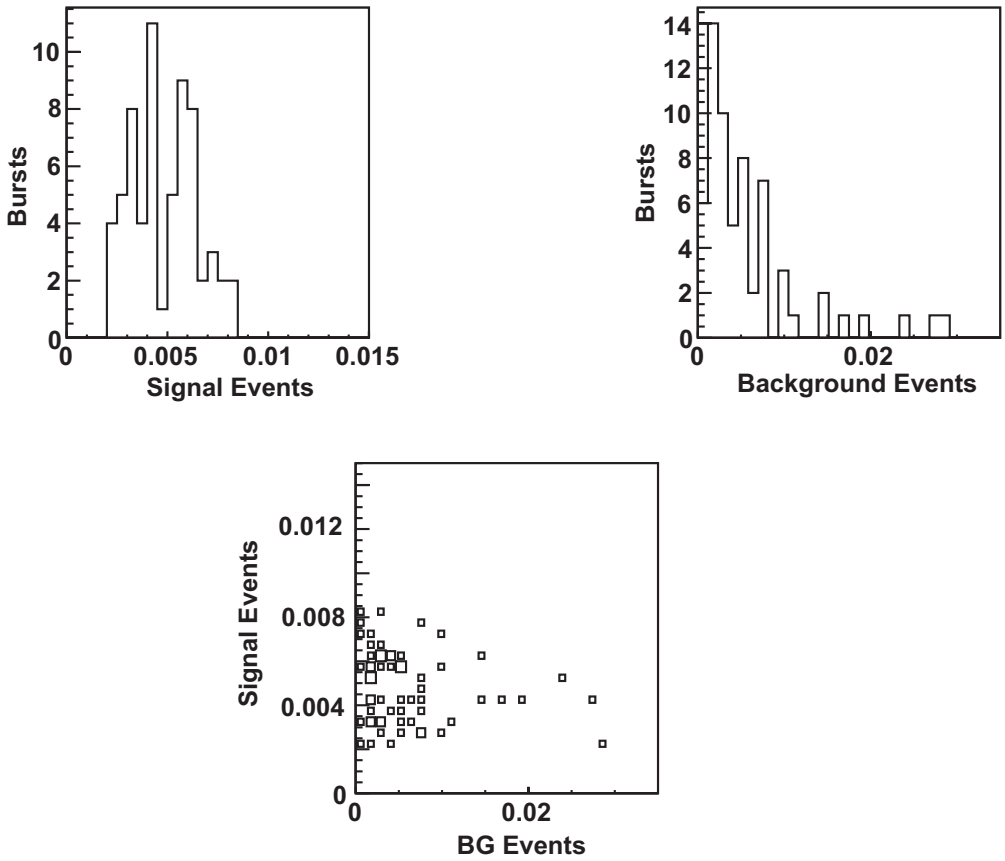

Figure 5.28: Number of signal and background events passing the selected cuts for all 64 bursts.

resulting in the following MRF:

$$\text{MRF} = 7.15 \ . \tag{5.27}$$

5.5.4 Systematic Uncertainties

There are several sources of systematic uncertainties. This section enumerates the possible sources of the systematic uncertainties relevant for this analysis and gives a brief summary on their estimation. Studies of the systematic uncertainties have been accomplished for an E^{-2} input energy spectrum. Simulations to estimate the effect of systematic uncertainties caused by various sources on the signal event rate have been performed by M. Ackermann [49].

- **Optical Module Efficiency**: Glass, gel and boundary layer transmittivities and the quantum efficiency of the OMs were measured under laboratory conditions [62] and included in the simulation. Simulations of the atmospheric neutrino declination distribution for different OM efficiencies between 70 % and 130 % were compared to

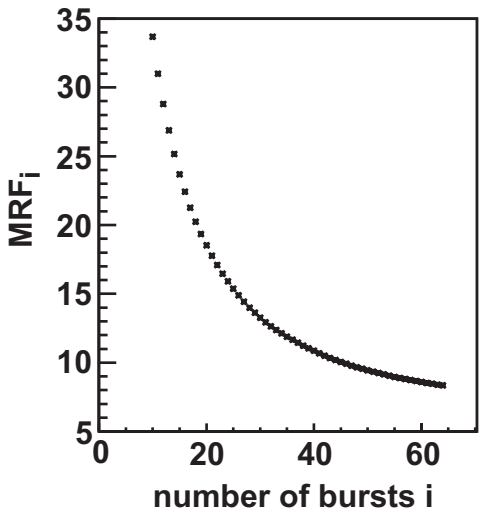

Figure 5.29: Combined MRF dependent on number of bursts included, i.

a data sample dominated by atmospheric neutrinos applying a Kolmogorov-Smirnov test. The 1-σ-interval of $[0.9, 1.03]$ obtained in the test is considered as the systematic uncertainty in the OM efficiency. Simulations were performed to estimate the resulting uncertainty in the signal event rate of an E^{-2} energy spectrum and yielded $+2\,\%$ and -9%.

- **Time Calibration**: The time delay due to the signal readout is calibrated with a laser. Simulations studied the influence of the calibration accuracy on the signal rates and their angular resolution [63]. The resulting uncertainty in the signal rates caused by timing calibration uncertainties was found to be negligible ($\sim 1\,\%$).

- **Rock density**: Absorption rates of the muons and neutrino conversion rates depend on the density of the medium. The uncertainty in the density of the surrounding ice can be neglected since the density is well known. But the density of the conversion region is not extensively probed. It is treated as standard rock of density $2650\,\mathrm{kg\,m^{-3}}$. Typical rock density varies between $2300\,\mathrm{kg\,m^{-3}}$ and $2800\,\mathrm{kg\,m^{-3}}$. Assuming an uncertainty of $10\,\%$ for the rock density, results in changes in the event rate of $2\,\%$ for horizontal events and $7\,\%$ for vertical events.

- **Neutrino Interaction Cross Section**: The neutrino event rate is a linear function of the cross section. Uncertainties in the cross section arise from uncertainties in the structure functions of the nucleons. Simulation studies imply an uncertainty in the cross section between $100\,\mathrm{GeV}$ and $1\,\mathrm{PeV}$ of approximately $3\,\%$, which yields the same uncertainty in the event rate.

- **Neutrino-muon Angle**: NUSIM does not take into account the scattering angle between neutrino and muon in the charged current interaction described by equa-

tion 4.2. For the neutrino energies of interest in this analysis the scattering angle and accordingly the resulting uncertainty in the event rate is negligibly small ($\sim -1\,\%$).

- **Muon Propagation**: In the simulation the muons are propagated through ice and rock, where they generate secondaries, eventually decay and lose energy in ionization and bremsstrahlung. Secondarys produce pairs and interact in photo-nuclear processes. For the energies of interest the cross sections for these processes are well known with small uncertainties of 1-2 % [64]. Simulations with varying cross sections have been performed and showed that a simultaneous variation of all cross sections by 2 % results in a variation of the event rate of 1 %.

- **Photon Propagation**: Čerenkov photons are propagated through ice using the PTD photon propagation package. A simplified model describes the ice properties. To estimate the effect of uncertainties in the photon propagation on the event rate the PTD results were compared to results of an other photon propagation program PHOTONICS. PHOTONICS uses a fundamentally different approach to describe the structure of ice. The estimated systematic uncertainty caused by the photon propagation is approximately 2 %.

- **Reconstruction Bias**: Some features of real events might not be accounted for in the simulation. If these features effect the reconstruction a mismatch between simulated and real data in the distribution of event parameters could occur. Possible features of this type are residual cross talk hits that passed the hit cleaning or short time variations in the OM noise rate. A slight mismatch in the smoothness and angular resolution distribution of simulated and real data at a high cut level ($> 95\,\%$ atmospheric neutrinos) was found. This mismatch could be due to the few remaining misreconstructed down-going muons, but might as well originate in a systematic bias. Conservatively assuming the latter case allows the calculation of a scaling factor between MC and real data. From the point source analysis [65] it is known that the difference of expected events passing the final point source cuts with and without scaling is -7 %. Since the cuts of the point source analysis are not significantly different from the ones used in this analysis we quote this difference as systematic error from reconstruction bias.

- **IPN Burst Flux**: The average neutrino flux predicted by the Waxman Bahcall spectrum is based on BATSE triggered bursts. During the runtime of BATSE it was found that 88 % of the bursts which triggered BATSE, are detected by other IPN satellites as well. The remaining 12 % detected by the IPN but not triggered BATSE belong to the class of BATSE non-triggered bursts, which have on average less than 1/10 of the peak photon flux of their triggered counterparts. The flux model assumes that the neutrino flux is proportional to the photon flux and therefore including non-triggered bursts in the upper limit calculation artificially increases the expected number of signal events. Assuming that 12 % of the bursts contribute only 1/10 of the expected flux per burst while the other ones contribute the full expected

flux yields a correction in the number of signal events of

$$0.12 \cdot \frac{1}{10} + 0.88 = 0.892 \tag{5.28}$$

or accordingly -11 %.

- **Short Burst Flux**: Furthermore short bursts are not included in the calculation of the average neutrino flux. Ten bursts out of 64 have a duration smaller than 2 s and are therefore classified as short bursts. We assume conservatively that the short bursts have a lower flux compared to the long ones and thus contribute to the systematic uncertainties with $-\frac{10}{64} = -16\,\%$.

Assuming that the listed systematic uncertainties σ_i are independent allows the calculation of the total systematic uncertainty σ_{total}:

$$\sigma_{total} = \sqrt{\sum_{i=1}^{10} \sigma_i^2} \tag{5.29}$$

Table 5.3 summarizes the individual uncertainties and quotes the resulting total uncertainty of +8 % and -24 %.

Including Systematic Uncertainties in the Upper Limit

The compatibility of the number of observed events and the number of background events depends on the systematic uncertainties in the measurement and in the simulation. Therefore, they are included in the calculation of an upper limit. Conrad et al. [66] developed a method to incorporate systematic uncertainties by averaging over probability density functions that parameterize the uncertainties. It is possible to include theoretical uncertainties of the background process as well as uncertainties in the signal detection efficiency. Assuming that the uncertainties are described by a Gaussian distribution the modified probability density function (PDF) is:

$$q(n)_{s+b} = \frac{1}{2\pi\sigma_b\sigma_s} \int_0^\infty \int_0^\infty p(n)_{b'+\epsilon' s}\; e^{\frac{-(b-b')^2}{2\sigma_b^2}}\, e^{\frac{-(1-\epsilon')^2}{2\sigma_\epsilon^2}}\, db' d\epsilon' \tag{5.30}$$

σ_ϵ is the uncertainty in the signal detection efficiency relative to the nominal efficiency. Accordingly b is the estimated background and σ_b its uncertainty. $p(n)_{s+b}$ describes the PDF to observe n events for a fixed but unknown signal s and the known background b. Usually, the distribution of the uncertainty is considered Poissonian.
The detector response is simulated including the best knowledge of its efficiency. But still uncertainties are present as not every detail of the detector is fully understood and some effects might be missing in the simulation. These uncertainties affect the calculation of the expected signal predicted by a theoretical model. The simulations might not be comparable to the known background since the efficiency of the signal differs from the

Table 5.3: Summary of systematic uncertainties

Source of Systematic Uncertainty	Resulting Uncertainty in the Signal Rate
OM efficiency	+ 2 % − 9 %
Time Calibration	± 1 %
Rock Density	± 7 %
Neutrino Cross Section	± 3 %
Neutrino-muon Scattering Angle	+ 0 % − 1 %
Muon Propagation	± 1 %
Photon Propagation	± 2 %
Reconstruction Bias	+ 0 % − 7 %
IPN Burst Flux	+ 0 % − 11 %
Short Burst Flux	+ 0 % − 16 %
Sum	+ 8 % − 24 %

background efficiency, which presents the actual detector behavior. If no uncertainty in the signal detection efficiency is present σ_ϵ becomes zero in relative terms to the nominal efficiency, in such a hypothetical case the detector simulation describes the detector response perfectly well and simulations can be compared to recorded data. However, uncertainties do occur in the simulation and thus have to be accounted for in the calculation of the upper limit.
In this analysis the software POLE[14] is used to solve the integrals over the systematic uncertainties of equation 5.30. POLE performes a Monte Carlo integration and calculates the modified confidence belt.
The total systematic uncertainty (+8 %, -24 %) estimated in the previous section is asymmetric and its distribution is unknown. We assume the signal detection efficiency to follow a Gaussian distribution with mean at

$$1 - 0.24 + 0.08 = 0.84 \ , \tag{5.31}$$

and a standard deviation of $\frac{0.24+0.08}{2} = 0.16$. In this case POLE returns the following 90 % confidence interval

$$[0.00, 2.97] \ . \tag{5.32}$$

Compared to the confidence interval without including systematic uncertainties $[0.00, 2.43]$ the upper limit increased. The given upper limits are the average upper limits that would be obtained by an ensemble of experiments with the expected background of $b_{\mathrm{com}} = 0.17$ and no true signal. They determine the **experimental sensitivity**.

[14] POissonian Limit Estimator

Chapter 6

Unblinding and Results

The analysis described in detail in chapter 5 was presented to the IceCube collaboration and approval for unblinding the on-time data was given. The cuts obtained in the optimization were applied to the data contained in the defined neutrino search time window. No recorded neutrino event passed the cuts. This null result allows to set an upper limit on the predicted neutrino flux emitted by GRBs. Inserting the average event upper limit estimated in section 5.5.4 into equation 5.16 yields an average upper limit to the predicted per burst flux at 90 % confidence level of

$$E^2 \cdot \Phi(E)_{90\%} \leq 4.4 \cdot 10^{-4}\,\mathrm{GeV\,cm^{-2}\,s^{-1}} \tag{6.1}$$

in the energy range of 10^5 GeV to 10^7 GeV (the plateau of the Waxman Bahcall spectrum). This results in an average upper limit to the diffuse flux (see section 2.2.5) of

$$E^2 \cdot \Phi(E)_{90\%} \leq 3.9 \cdot 10^{-8}\,\mathrm{GeV\,cm^{-2}\,s^{-1}\,sr^{-1}}\ . \tag{6.2}$$

These limits are above the model prediction given in 2.2.5 by a factor of 8.8 .
The obtained limits are compared to the analysis of 400 well localized bursts in 1997-2003 performed by Hardtke and Kuehn [56]. The combined limit to the diffuse flux by this analysis is

$$E^2 \cdot \Phi(E)_{90\%} \leq 6.0 \cdot 10^{-9}\,\mathrm{GeV\,cm^{-2}\,s^{-1}\,sr^{-1}}\ , \tag{6.3}$$

which is 6.5 times below our limit. It is not suprising that the combined limit of 400 bursts lies below the limit resulting from an analysis of only 64 bursts, since the number of expected signal events increases linearly with the number of bursts. However, the expected number of background events is suprising: 151 well localized bursts during the AMANDA-II runtime yield an expected number of background events of 1.29 [56] while we expect only 0.17 background events in the analysis of 64 bursts, although we obtain a comparable signal rate of 70 - 75 % relative to Level 3 passing the selection cuts. Our analysis yields a smaller number of expected background events per burst and at the same time a comparable signal passing rate although it covers a larger solid angle due to the poor localization. This can be explained by the cut selection: Former muon neutrino GRB analyses determined one single set of cuts for all analyzed bursts while

the presented analysis of poorly localized bursts selects an individual set of cuts for each burst. Treating each burst separately leads to a strongly reduced number of background events due to the different dependence of background and signal on the burst duration. The signal predicted by the theoretical flux model is independent of the duration, because the bursts are assumed to produce an equal amount of energy. Therefore, short bursts are expected to have a higher luminosity compared to long burst. On the other hand, the background increases linearly with the burst duration. Thus, it is desirable to tighten the cuts for long bursts and apply looser cuts to short bursts. This is implemented in the optimization process of the current analysis. Especially for a discovery a low number of expected background events is extremely important, because the lower flux limit decreases with increased expected background.

Chapter 7

Summary and Outlook

We analyzed 64 bursts to find a temporal and directional coincidence between muon neutrinos and gamma emission. The bursts were poorly localized by non-direction sensitive satellites of the IPN and the KONUS instrument between 2000 and 2004 while the neutrino data was recorded by AMANDA-II. We have determined the detector stability for the two hour off-time window of the analyzed bursts. Two different detector stability tests were performed: the cumulative test and the likelihood test. The cumulative test is particularly suitable to find time correlated instabilities, while the likelihood test is sensitive to temporally uncorrelated distortions. In contrast to other analyses, criteria are fixed based on these two tests to define when to exclude a burst from the analysis. The tests with the defined criteria will be useful for future GRB coincidence analyses and represents a first step towards the standardization of detector stability tests in GRB analyses.
Directional and reconstruction quality cuts were selected and optimized in an iterative way by minimizing the model rejection factor. An individual set of cuts for each burst was obtained to account for strongly varying localization regions and burst durations. Comparison with former analyses of well localized GRBs shows that this method results in less expected background events without decreasing the signal passing rate. A low number of expected background events is extremely important especially for a potential discovery in future analyses, because the lower flux limit decreases with increased expected background. Thus, future GRB analyses should account for the varying burst duration in the cut optimization.
No recorded neutrino events passed the optimized cuts. According to this null result, an upper limit on the neutrino flux from GRBs predicted by the Waxman Bahcall model was set. The obtained limit to the diffuse flux is

$$E^2 \cdot \Phi(E)_{90\%} \leq 3.9 \cdot 10^{-8}\,\mathrm{GeV\,cm^{-2}\,s^{-1}\,sr^{-1}}$$

and lies a factor of 8.8 above the model prediction $E^2 \cdot \Phi_\nu^{WB} = 4.5 \cdot 10^{-9}\,\mathrm{GeV\,cm^{-2}\,s^{-1}\,sr^{-1}}$. A lower limit than this one could be set on the diffuse flux in the former analysis of 400 well localized bursts in 1997-2003 performed by Hardtke and Kuehn [56] due to a larger number of analyzed bursts. Still, this lower limit lies 1.3 times above the predicted model

flux. The theoretical prediction has neither been proven nor ruled out.
Several improvements are conceivable in the future. First of all the presented analysis could be extended to a precursor search, which extends the neutrino search time window to 100 or more seconds before the start time of gamma emission observation. This alternative analysis would be based on a different model. Precursor neutrinos could be produced in p-p-interactions either within the star or in the immediate circumburst environment predicted by GRB models different to the fireball model (see for example [67]).
Larger detector volumes will be realized in future detectors like IceCube, which is currently under construction. Once completed, IceCube will consist of 4800 OMs arranged on 80 strings instrumenting a volume of $1\,\mathrm{km}^3$, 70 times larger than the AMANDA-II volume. One year of IceCube data - assuming full instrumentation - provides the sensitivity needed to verify predictions of coincident neutrino flux from GRBs [68]. Detection sensitive satellites like Swift or GLAST will support future coincidence searches. Future analyses could also be improved by taking into account individual burst parameters like redshift, gamma-factor and the photon spectral indices, instead of working with average values. The individual neutrino flux can vary up to several magnitudes, dependent upon these parameters [69] leading to variations of the calculated flux limit. These parameters were not measured for many GRBs in the past, thus, unfortunately it was not possible to include individual neutrino spectra in the presented analysis.
Furthermore, the novel method of optical follow-up will increase the sensitivity of neutrino telescopes to identify transient sources like GRBs. The idea is to complement the coincidence search by performing an automated optical follow-up of selected neutrino events. We expect an increase in the sensitivity to GRBs by a factor of 2-3 utilizing an optical follow-up program triggered by the detection of high-energy events with certain multiplicity realized by a network of automated 1-2 meter optical telescopes monitoring the corresponding part of the sky for GRB afterglows. [70]

Appendix A

Detailed Burst Information

The following tables quote the characteristics of 80 poorly localized bursts used in this analysis. The start time of each burst is taken from the IPN catalog and represents the times when the emission rises significantly above the background. The durations were provided by Kevin Hurley in private communication and represent the time during which the burst emits clearly detectable gamma-ray emission (see section 3.1).

Table A.1: List of Initially Selected GRBs in 2000 from the IPN catalog

day	**month**	**year**	**hour**	**minute**	**second**	**duration [s]**	**stability**
9	MAR	2000	2	43	50	14.50	stable
20	APR	2000	11	44	31	0.25	stable
17	MAY	2000	10	2	4	60.42	stable
27	MAY	2000	12	46	30	22.00	stable
18	JUN	2000	21	32	24	17.70	stable
19	JUN	2000	23	28	0	50.00	stable
27	JUL	2000	4	7	53	29.89	stable
7	AUG	2000	3	16	19	23.00	stable
29	AUG	2000	2	30	52	6.34	stable
18	SEP	2000	16	11	56	15.00	stable
30	NOV	2000	3	59	35	2.50	stable
26	MAY	2000	23	28	15	0.60	stable
18	SEP	2000	19	35	18	2.75	stable

Table A.2: List of Initially Selected GRBs in 2001 from the IPN catalog

day	month	year	hour	minute	second	duration [s]	stability
12	FEB	2001	17	26	39	24.45	bad files
13	FEB	2001	2	57	26	12.00	bad files
24	FEB	2001	4	49	18	19.00	stable
6	MAR	2001	22	35	46	18.75	stable
8	MAY	2001	13	17	8	25.00	stable
13	MAY	2001	11	33	30	380.00	stable
16	MAY	2001	15	24	39	53.00	stable
30	MAY	2001	19	47	20	9.00	stable
23	JUN	2001	3	31	16	7.00	stable
3	JUL	2001	20	30	51	8.00	stable
11	JUL	2001	2	43	30	220.00	stable
13	JUL	2001	7	58	28	15.00	stable
30	JUL	2001	3	30	43	41.00	stable
7	AUG	2001	9	16	58	61.82	stable
26	AUG	2001	18	6	3	285.57	unstable
18	SEP	2001	15	31	14	19.00	stable
29	SEP	2001	0	22	43	18.00	stable
16	JUN	2001	5	35	23	0.20	stable
15	JUL	2001	20	23	46	47.00	stable
3	OCT	2001	3	34	9	48.00	stable
8	OCT	2001	19	55	52	14.00	stable
22	NOV	2001	20	51	34	12.00	stable

Table A.3: List of Initially Selected GRBs in 2002 from the IPN catalog

day	month	year	hour	minute	second	duration [s]	stability
13	JAN	2002	2	4	12	2.00	stable
13	JAN	2002	11	2	46	21.00	stable
26	JAN	2002	7	15	34	26.00	stable
8	FEB	2002	6	1	43	35.00	stable
2	MAR	2002	12	23	40	325.00	stable
7	APR	2002	4	11	40	23.42	stable
30	APR	2002	0	26	49	7.00	stable
8	MAY	2002	20	37	59	12.29	stable
14	MAY	2002	18	35	57	8.77	stable
19	MAY	2002	14	53	34	56.00	stable
29	MAY	2002	3	53	10	36.00	bad files
2	JUN	2002	17	30	28	0.60	stable
15	JUN	2002	18	2	23	12.00	stable
30	JUN	2002	6	37	28	21.44	stable
15	JUL	2002	6	24	34	15.00	bad files
25	JUL	2002	16	25	39	27.00	bad files
14	SEP	2002	21	15	12	9.00	stable
6	OCT	2002	7	32	2	26.00	stable
11	OCT	2002	4	37	55	41.00	stable
16	JAN	2002	20	47	37	10.00	stable
15	MAR	2002	15	42	46	22.00	stable
9	APR	2002	9	27	15	25.00	stable

Table A.4: List of Initially Selected GRBs in 2003 from the IPN catalog

day	month	year	hour	minute	second	duration [s]	stability
25	FEB	2003	15	2	47	19.00	stable
4	MAR	2003	23	34	24	2.30	unstable
18	MAR	2003	2	46	30	86.00	stable
28	MAR	2003	7	27	17	300.00	stable
19	MAY	2003	10	2	42	15.00	stable
23	MAY	2003	14	10	54	0.25	stable
7	JUN	2003	2	19	21	0.20	stable
29	JUN	2003	13	8	56	20.00	bad files
1	JUL	2003	17	0	49	35.00	stable
6	JUL	2003	20	6	56	58.00	stable
9	JUL	2003	10	37	25	29.16	stable
11	JUL	2003	17	50	26	12.00	stable
26	JUL	2003	9	51	8	132.00	stable
29	SEP	2003	14	27	14	0.60	stable
3	DEC	2003	5	58	57	9.00	stable
18	DEC	2003	6	28	8	0.70	stable
15	FEB	2003	17	11	52	52.80	stable

Table A.5: List of Initially Selected GRBs in 2004 from the IPN catalog

day	month	year	hour	minute	second	duration [s]	stability
2	MAR	2004	4	14	35	1.00	stable
4	APR	2004	10	58	51	7.00	bad files
9	APR	2004	13	39	8	64.77	stable
19	MAY	2004	10	42	53	4.80	stable
15	JUN	2004	11	22	29	74.45	bad files
1	JUL	2004	22	46	44	10.00	stable
11	DEC	2004	7	49	50	22.40	stable

Bibliography

[1] R. W. Klebesadel, I. B. Strong, and R. A. Olsen, "Observation of Gamma-Ray-Bursts of Cosmic Origin," *Astrophys. J.* **182** (1973) L85–L88.

[2] K. Hurley, "A Gamma-Ray Burst Bibliography, 1973-2001." http://www.ssl.berkeley.edu/ipn3/grbbiblio.pdf.

[3] **BAIKAL** Collaboration, V. A. Balkanov *et al.*, "The Lake Baikal neutrino experiment," *Nucl. Phys. Proc. Suppl.* **87** (2000) 405–407, `astro-ph/0001145`.

[4] R. D. Preece *et al.*, "The BATSE Gamma-Ray Burst Spectral Catalog. I. High Time Resolution Spectroscopy of Bright Bursts using High Energy Resolution Data," *Astrophys. J. Suppl.* **126** (2000) 19, `astro-ph/9908119`.

[5] **Swift Science** Collaboration, N. Gehrels *et al.*, "The Swift Gamma-Ray Burst Mission," *AIP Conf. Proc.* **727** (2004) 637–641, `astro-ph/0405233`.

[6] W. S. Paciesas *et al.*, "The Fourth BATSE Gamma-Ray Burst Catalog (Revised)," *Astrophys. J. Suppl.* **122** (1999) 465–495, `astro-ph/9903205`.

[7] P. Meszaros, "Gamma-Ray Bursts," *Rept. Prog. Phys.* **69** (2006) 2259–2322, `astro-ph/0605208`.

[8] G. J. Fishman, "Gamma-Ray Bursts: an Overview," *Publication of the Astronomical Society of the Pacific* **107** (Dec., 1995) 1145–+.

[9] B. Zhang and P. Meszaros, "Gamma-Ray Bursts: Progress, Problems and Prospects," *Int. J. Mod. Phys.* **A19** (2004) 2385–2472, `astro-ph/0311321`.

[10] J. Greiner *et al.*, "Evolution of the polarization of the optical afterglow of the gamma-ray burst GRB 030329," *Nature* **426** (2003) 257–259, `astro-ph/0311282`.

[11] D. Bersier *et al.*, "The Strongly Polarized Afterglow of GRB 020405," *Astrophys. J.* **583** (2003) L63–L66, `astro-ph/0206465`.

[12] S. Klose *et al.*, "Prospects for multiwavelength polarization observations of GRB afterglows and the case GRB 030329," *Astron. Astrophys.* **420** (2004) 899–903, `astro-ph/0403504`.

[13] B. Ryden, *Introduction to Cosmology*. Addison Wesley, 2003.

[14] B. Stern, J. Poutanen, and R. Svensson, "Brightness dependent properties of gamma-ray bursts," astro-ph/9703167.

[15] J. P. Norris, G. F. Marani, and J. T. Bonnell, "Connection Between Energy-dependent Lags and Lorentz Factor in Gamma-ray Bursts," *Astrophys. J.* **534** (2000) 248–257, astro-ph/9903233.

[16] D. E. Reichart *et al.*, "A Possible Cepheid-Like Luminosity Estimator for the Long Gamma-Ray Bursts," astro-ph/0004302.

[17] D. Band *et al.*, "BATSE observations of gamma-ray burst spectra. 1. Spectral diversity," *Astrophys. J.* **413** (1993) 281–292.

[18] J. K. Becker, M. Stamatikos, F. Halzen, and W. Rhode, "Coincident GRB neutrino flux predictions: Implications for experimental UHE neutrino physics," *Astropart. Phys.* **25** (2006) 118–128, astro-ph/0511785.

[19] S. E. Woosley and J. S. Bloom, "The supernova – gamma-ray burst connection," *Ann. Rev. Astron. Astrophys.* **44** (2006) 507–556, astro-ph/0609142.

[20] T. Piran, "The physics of gamma-ray bursts," *Rev. Mod. Phys.* **76** (2004) 1143–1210, astro-ph/0405503.

[21] B. Paczynski, "Gamma-ray bursters at cosmological distances," *Astrophys. J.* **308** (1986) L43–L46.

[22] P. Meszaros and M. J. Rees, "High-entropy fireballs and jets in gamma-ray burst sources," *Mon. Not. Roy. Astron. Soc.* **257** (1992) 29–31.

[23] A. R. Bell, "The acceleration of cosmic rays in shock fronts. II," *Mon. Not. Roy. Astron. Soc.* **182** (1978) 443–455.

[24] E. Fermi, "On the Origin of the Cosmic Radiation," *Phys. Rev.* **75** (1949) 1169–1174.

[25] T. K. Gaisser, "Cosmic rays and particle physics,". Cambridge, UK: Univ. Pr. (1990) 279 p.

[26] T. Piran, "Gamma-Ray Bursts - When Theory Meets Observations," astro-ph/0104134.

[27] T. Piran, "Gamma-Ray Bursts - a Primer For Relativists," gr-qc/0205045.

[28] E. Waxman and J. N. Bahcall, "High energy neutrinos from cosmological gamma-ray burst fireballs," *Phys. Rev. Lett.* **78** (1997) 2292–2295, astro-ph/9701231.

[29] W.-M. Yao *et al.*, *Particle Physics Booklet*. Institute of Physics Publishing, 2006.

[30] E. Waxman and J. N. Bahcall, "High energy neutrinos from astrophysical sources: An upper bound," *Phys. Rev.* **D59** (1999) 023002, `hep-ph/9807282`.

[31] D. Guetta, D. Hooper, J. Alvarez-Muniz, F. Halzen, and E. Reuveni, "Neutrinos from individual gamma-ray bursts in the BATSE catalog," *Astropart. Phys.* **20** (2004) 429–455, `astro-ph/0302524`.

[32] E. Waxman, "Astrophysical sources of high energy neutrinos," *Nucl. Phys. Proc. Suppl.* **118** (2003) 353, `astro-ph/0211358`.

[33] K. Zuber, "Neutrino physics,". Bristol, UK: IOP (2004) 438 p.

[34] B. Kayser, "Neutrino Mass, Mixing, and Flavor Change,".

[35] H. Athar, M. Jezabek, and O. Yasuda, "Effects of neutrino mixing on high-energy cosmic neutrino flux," *Phys. Rev.* **D62** (2000) 103007, `hep-ph/0005104`.

[36] A. Dar and A. De Rujula, "A cannonball model of gamma-ray bursts: superluminal signatures," `astro-ph/0008474`.

[37] A. Dar and A. De Rujula, "The cannonball model of gamma ray bursts: High-energy neutrinos and gamma-rays," `astro-ph/0105094`.

[38] K. Hurley, M. Sommer, J.-L. Atteia, M. Boer, T. Cline, F. Cotin, J.-C. Henoux, S. Kane, P. Lowes, and M. Niel, "The solar X-ray/cosmic gamma-ray burst experiment aboard ULYSSES," *Astron. Astrophy. Suppl. Ser.* **92** (Jan., 1992) 401–410.

[39] Y. Shirasaki *et al.*, "Design and Performance of the Wide-Field X-Ray Monitor on Board the High-Energy Transient Explorer 2," *Publ. Astron. Soc. Jap.* **55** (2003) 1033, `astro-ph/0311067`.

[40] J.-L. Atteia *et al.*, "In flight performance and first results of FREGATE," *AIP Conf. Proc.* **662** (2003) 3–16, `astro-ph/0202515`.

[41] J. N. Villasenor, R. Dill, J. P. Doty, G. Monnelly, R. Vanderspek, S. Kissel, G. Prigozhin, G. B. Crew, and G. R. Ricker, "An Overview of the HETE Soft X-ray Camera," in *AIP Conf. Proc. 662: Gamma-Ray Burst and Afterglow Astronomy 2001: A Workshop Celebrating the First Year of the HETE Mission*, G. R. Ricker and R. K. Vanderspek, eds., pp. 33–37. Apr., 2003.

[42] M. Longair, *High Energy astrophysics*, vol. 2. Cambridge University Press, 2 ed., 1994.

[43] S. P. Wyatt, *Principles of Astronomy*. Allyn and Bacon, Inc., 3 ed., 1977.

[44] E. Andres *et al.*, "The AMANDA neutrino telescope: Principle of operation and first results," *Astropart. Phys.* **13** (2000) 1–20, astro-ph/9906203.

[45] **AMANDA** Collaboration, J. Ahrens *et al.*, "Muon track reconstruction and data selection techniques in AMANDA," *Nucl. Instrum. Meth.* **A524** (2004) 169–194, astro-ph/0407044.

[46] J. G. Learned and S. Pakvasa, "Detecting tau-neutrino oscillations at PeV energies," *Astropart. Phys.* **3** (1995) 267–274, hep-ph/9405296.

[47] R. Gandhi, C. Quigg, M. H. Reno, and I. Sarcevic, "Ultrahigh-energy neutrino interactions," *Astropart. Phys.* **5** (1996) 81–110, hep-ph/9512364.

[48] A. Karle, "Observations of high energy neutrinos with water/ice neutrino telescopes," *J. Phys. Conf. Ser.* **39** (2006) 379–385, astro-ph/0602025.

[49] M. Ackermann, "Searches for signals from cosmic point-like sources of high energy neutrinos in 5 years of AMANDA-II data," PhD thesis, Humboldt-Universitaet zu Berlin, 2006.

[50] G. C. Hill, "Detecting neutrinos from AGN: New fluxes and cross sections," *Astropart. Phys.* **6** (1997) 215–228, astro-ph/9607140.

[51] D. Chirkin and W. Rhode, "Muon Monte Carlo: A New high precision tool for muon propagation through matter,". Contributed to 27th International Cosmic Ray Conference (ICRC 2001), Hamburg, Germany, 7-15 Aug 2001.

[52] A. Karle, "Monte Carlo simulation of photon transport and detection in deep ice: Muons and cascades,". Prepared for International Workshop on Simulations and Analysis Methods for Large Neutrino Telescopes, Zeuthen, Germany, 6-9 Jul 1998.

[53] S. Hundertmark, "AMASIM neutrino detector simulation program,". Prepared for International Workshop on Simulations and Analysis Methods for Large Neutrino Telescopes, Zeuthen, Germany, 6-9 Jul 1998.

[54] D. "Pandel, ""Bestimmung von Wasser- und Detektorparametern und Rekonstruktion von Myonen bis 100 TeV mit dem Baikal-Neutrinoteleskop NT-72"," Diploma thesis, "Humboldt-Universitaet zu Berlin", 1996.

[55] P. Sudhoff, "Transmission measurements with AMANDA glass and evaluation for IceCube,". AMANDA internal report 20000201, DESY Zeuthen, 2000.

[56] **IceCube** Collaboration, A. Achterberg *et al.*, "The Search for Muon Neutrinos from Northern Hemisphere Gamma-Ray Bursts with AMANDA," astro-ph/0705.1186.

[57] M. Ribordy, "AMANDA-II/2000 data statistics, OM selection and retriggering procedure,". AMANDA internal report 20020601, DESY Zeuthen, 2002.

[58] **AMANDA** Collaboration, A. Bouchta, "Seasonal variation of the muon flux seen by AMANDA,". Prepared for 26th International Cosmic Ray Conference (ICRC 99), Salt Lake City, UT, 17-25 Aug 1999.

[59] P. Wallace *et al.*, "The SLALIB Library," *ASP Conference Series* **61** (1994) 481–484.

[60] G. C. Hill and K. Rawlins, "Unbiased cut selection for optimal upper limits in neutrino detectors: The model rejection potential technique," *Astropart. Phys.* **19** (2003) 393–402, astro-ph/0209350.

[61] G. J. Feldman and R. D. Cousins, "A Unified approach to the classical statistical analysis of small signals," *Phys. Rev.* **D57** (1998) 3873–3889, physics/9711021.

[62] P. Sudhoff, "Transmission measurements with AMANDA glass and evaluation for IceCube,". AMANDA internal report 20010701, DESY Zeuthen, 2001.

[63] A. Biron, "Reconstruction uncertainties due to time calibration errors,". AMANDA internal report 20001101, DESY Zeuthen, 2000.

[64] E. V. Bugaev, I. A. Sokalski, and S. I. Klimushin, "Simulation accuracy of long range muon propagation in medium: Analysis of error sources," hep-ph/0010323.

[65] **IceCube** Collaboration, A. Achterberg *et al.*, "Five years of searches for point sources of astrophysical neutrinos with the AMANDA-II neutrino telescope," *Phys. Rev.* **D75** (2007) 102001, astro-ph/0611063.

[66] J. Conrad, O. Botner, A. Hallgren, and C. Perez de los Heros, "Including systematic uncertainties in confidence interval construction for Poisson statistics," *Phys. Rev.* **D67** (2003) 012002, hep-ex/0202013.

[67] S. Razzaque, P. Meszaros, and E. Waxman, "Neutrino signatures of the supernova - gamma ray burst relationship," *Phys. Rev.* **D69** (2004) 023001, astro-ph/0308239.

[68] **IceCube** Collaboration, A. Achterberg *et al.*, "Detecting GRBs with IceCube and optical follow-up observations,". Prepared for 30th International Cosmic Ray Conference (ICRC 07), Merida, Mexico, 2007.

[69] **IceCube** Collaboration, M. Stamatikos, J. Kurtzweil, and M. J. Clarke, "Probing for leptonic signatures from GRB030329 with AMANDA- II," astro-ph/0510336.

[70] M. Kowalski and A. Mohr, "Detecting neutrino-transients with optical follow-up observations," astro-ph/0701618.

Acknowledgement

Numerous people contributed greatly to this thesis.
First, this work was initiated by Prof. Steve Barwick during my studies at the University of California Irvine (UCI). I thank Steve Barwick for supervising me: he taught me the basics of the AMANDA experiment and GRB neutrino search. Not only did he and his secretary help me to overcome all the little problems of my daily life like finding an appartement, choosing interesting classes etc., but Prof. Barwick had an important influence in the physics of this work. Many people made the time in Irvine enjoyable: Kyler Kuehn and Lisa Gerhard helped me to take the first steps in a new experiment. The graduate students from the physics department introduced me to the off-campus life in Irvine. Many thanks to Cathy, Dave and Quinn for making this stay unforgettable. Last but not least this stay would not have been possible without the financial support of the DAAD.
Back in Wuppertal, Prof. Karl-Heinz Kampert led the work in the right direction and to a successful conclusion. I am indebted to him for his support and supervision. He inspired me during this year in Wuppertal and made me believe in my work even in times of frustration. I am grateful to every member of the working group for pleasant working conditions and many fruitful discussions. I express particular gratitude to Timo Karg, who always had time to help me with small and big problems, and thus contributed a lot to the completion of my thesis. Thanks go to Heiko Geenen and Lars Linden for being lovely officemates, to Jan-Patrick Hülss for proofreading my thesis, and special thanks to Daniel Kümpel for being my collegue and good friend ever since our "Brückenkurs".
Finally I am much obliged to my family and friends. During my education I received affectionate encouragement from my parents, ranging from financial support to lovingly prepared meals. I am thankful to my aunt for correcting the language mistakes in this text. Many thanks go to my good friends Jessika Eiler, Jenny Golan and Henrik Pferdehirt for their encouragement, especially in times of frustration. Thank you, Andi, for being my chill-out area.

Hiermit versichere ich, dass ich diese Arbeit nur unter Zuhilfenahme der angegebenen Quellen und Hilfsmittel selbständig angefertigt habe.

Wuppertal, Juli 2007 Anna Franckowiak